

## A Search for Hierarchical Triples using Kepler Eclipse Timing

D. R. Gies, S. J. Williams, R. A. Matson, Z. Guo, S. M. Thomas

*Center for High Angular Resolution Astronomy and Department of Physics and Astronomy, Georgia State University, P. O. Box 4106, Atlanta, GA 30302-4106, USA*

gies@chara.gsu.edu, swilliams@chara.gsu.edu, rmatson@chara.gsu.edu,  
guo@chara.gsu.edu, thomas@chara.gsu.edu

J. A. Orosz

*Department of Astronomy, San Diego State University, San Diego, CA 92182-1221, USA*

orosz@sciences.sdsu.edu

and

G. J. Peters

*Space Sciences Center and Department of Physics and Astronomy, University of Southern California, Los Angeles, CA 90089-1341, USA*

gjpeters@mucen.usc.edu

### ABSTRACT

We present the first results of a *Kepler* survey of 41 eclipsing binaries that we undertook to search for third star companions. Such tertiaries will periodically alter the eclipse timings through light travel time and dynamical effects. We discuss the prevalence of starspots and pulsation among these binaries and how these phenomena influence the eclipse times. There is no evidence of short period companions ( $P < 700$  d) among this sample, but we do find evidence for long term timing variations in 14 targets (34%). We argue that this finding is consistent with the presence of tertiary companions among a significant fraction of the targets, especially if many have orbits measured in decades. This result supports the idea that the formation of close binaries involves the deposition of angular momentum into the orbital motion of a third star.

*Subject headings:* binaries: eclipsing — starspots — stars: variables: general — stars: formation

## 1. Introduction

Star formation requires very efficient processes to remove angular momentum from protostars in order to avoid faster than critical rotation. This may be accomplished by magnetic winds among lower mass stars (Matt & Pudritz 2005), but the fact that binary stars are common among the more massive stars (Mason et al. 1998; Kouwenhoven et al. 2007) suggests that much of their natal angular momentum is deposited into orbital motion (Larson 2002; Zinnecker & Yorke 2007). Models of massive star formation (Krumholz et al. 2009; Kratter et al. 2010) show that binary and often multiple stars with orbital dimensions measured in AU can form through disk fragmentation processes. In order to shrink such orbits to periods of days, interactions with a third star may be required to carry away angular momentum (for example, through Kozai cycles with tidal friction; Eggleton & Kiseleva-Eggleton 2001). There is now substantial evidence that many close binaries have distant tertiary companions (Pribulla & Rucinski 2006; Tokovinin et al. 2006; Raghavan et al. 2010).

One of the best methods to detect tertiary stars orbiting close, eclipsing binaries is to search for periodic variations in the eclipse times caused by the light travel delay associated with orbital motion, the so-called light travel time effect or LITE (Irwin 1959; Mayer 2004; Pribulla et al. 2005). If the third star’s orbital period is short ( $< 1$  year), then additional, dynamical perturbations of the inner orbit can occur that will also create changes in the eclipse times (Borkovits et al. 2011). The triple star system IU Aur may represent an example where such dynamical perturbations influence the eclipse timings (Özdemir et al. 2003). Eclipse timing observations have led to the identification of many candidate binaries with tertiary companions (Liao & Qian 2010; Zakirov 2010) and even the detection of planets around a binary (Lee et al. 2009). However, caution is required in the interpretation of trends in the eclipse times since other long-term, secular processes can also affect the angular momentum of the orbit (Zavala et al. 2002; Hoffman et al. 2006; Pilecki et al. 2007).

The NASA *Kepler* spacecraft offers us an unprecedented opportunity to search for tertiary companions of eclipsing binaries thanks to its extraordinary photometric precision and long time span of uninterrupted observations (Prša et al. 2011). Early results from *Kepler* have already led to the discovery of stellar (Slawson et al. 2011) and planetary companions (Doyle et al. 2011; Welsh et al. 2012) of binary stars. Here we present a first examination of the eclipse timing variations in 41 eclipsing binaries that were identified prior to the launch of *Kepler*. These systems are characterized by short periods, deep eclipses, and primary stars more massive than the Sun, parameters that may favor the detection of tertiary stars. A more complete examination of eclipse timing variations among a large subsample of binaries in the *Kepler* field of view will appear shortly (J. Orosz et al., in preparation). We describe the measurements in §2, outline the different processes that cause timing variations in §3,

and discuss our results in §4.

## 2. Eclipse Timing Measurements

We began this project in a Cycle 1 Guest Observer program on 20 targets, and we enlarged the sample to 40 and 41 systems in Cycles 2 and 3, respectively. The targets were selected from the All Sky Automated Survey Kepler Field of View study (Pigulski et al. 2009), the HATNET survey (Hartman et al. 2004), Vulcan survey (Borucki et al. 2001; Mjaseth et al. 2007), and early *Kepler* results (Prša et al. 2011). The binaries were chosen from semi-detached and fully detached systems with deep eclipses ( $> 0.2$  mag). The final sample consists of 41 binaries with orbital periods of 0.6 to 6.1 d and with primary star effective temperatures in the range 5200 to 11000 K according to the *Kepler Input Catalog* (Kepler Mission Team 2009).

We obtained all the long cadence, light curve data available through Quarter 9 (2009.3 – 2011.5). We used the Simple Aperture Photometry product that was processed with minimal assumptions about the long term flux variations. However, we found that there were significant drifts in flux level within and between the data quarters. These trends were removed in each quarter by binning the data into six parts and fitting a cubic spline through the means of the upper 50% of each sample. Then the full set was divided by the spline fit and the data from each quarter combined. This method effectively flattened out all the long term trends (on timescales larger than 30 d) with the exception of some fast drifts that are occasionally seen at the start of a quarter. The final product is a list of barycentric Julian date, normalized flux, and its uncertainty. There are some systematic differences between quarters (discussed further in the Appendix and noted by the letter Q in the final column of Table 1), the most egregious being those for KID 04678873, a star that has a nearby companion that blends by different amounts each quarter. Removing blending problems is important for models of the light curve, but the changing flux normalization has little influence on the eclipse timings we present here.

We measured the instance of mid-eclipse by fitting a model template to the observations around the eclipse times. The template was constructed by binning all the data in orbital phase according to an adopted period and trial epoch of mid-eclipse (usually from the work of Slawson et al. 2011), and then forming the mean phase and flux for each bin. We fit a parabola to the lowest 20% of the eclipse template data to find the actual phase of minimum, and this was used to re-center the template and adjust the epoch of minimum light. This served to produce a linear ephemeris of predicted eclipse times for the entire duration of the observations, and fits were made to each eclipse where there were at least three photometric

measurements in each of the eclipse itself and in both adjoining out-of-eclipse sections (of length similar to the full eclipse duration). Each eclipse was then fit in orbital phase space using the template by a non-linear, least-squares solution based upon four parameters, the relative flux level and slope outside of eclipse, the eclipse depth, and the time of mid-eclipse. The uncertainties in the eclipse times were estimated using the actual scatter of the observations from the fit of the template.

We made such template fits for both the primary and secondary eclipses, and we found improved periods by setting the slope of the observed minus calculated ( $O - C$ ) times to zero. There were many cases where the periods derived from the primary and secondary eclipses were significantly different, and we simply set the adopted period  $P_a$  to be the average of these two periods. The results are summarized in Table 1 that lists the *Kepler* identification number KID (appended with a P or S for the primary or secondary eclipses), the average timing error (the internal error  $I$ ), the standard deviation of the  $O - C$  times (the external error  $E$ ), the adopted period  $P_a$ , the epoch  $T$  of the mid-eclipse that defines the zero-point for the  $O - C$  residuals, and the period  $P$  that yields a zero slope in  $O - C$  diagram. The final columns give the formal value of  $\dot{P}/P$  derived from a weighted, quadratic fit of the  $O - C$  trend (a measure of curvature) and symbolic remarks about the character of the  $O - C$  diagram (discussed in §3 and the Appendix). Numbers in parentheses give the uncertainty in the last digit quoted.

We measured over 27000 eclipse times in total, and these are collected in Table 2 (given in full in the electronic version of the paper). The columns give the KID number, the time of the eclipse from the adopted linear ephemeris  $T_E$ , the eclipse type (1 for the primary and 2 for the secondary eclipse), the  $O - C$  measurement, and its uncertainty.

### 3. Characteristics of the $O - C$ Variability

The internal errors  $I$  associated with the timing measurements are very small (1 to 318 s) compared to the sampling time of the long cadence data (1765 s) thanks to the extreme precision of the *Kepler* observations. There are a few surprising cases where the external error  $E$  is less than the internal error  $I$ , and these correspond to systems containing pulsating stars, where the fast varying flux causes an increase in the estimate of the internal scatter. We find that  $E > I$  for most of the systems, indicating that there is some real variation present in the eclipse times. However, it is very important to place any apparent  $O - C$  variations in the context of the kinds of light curve variability observed outside of eclipse. We found that it was very useful to display the entire set of photometric measurements in a diagram showing differences from the mean light curve. We constructed such a diagram by placing

these differences in a gray scale image as a function of orbital phase (on the adopted linear ephemeris) and of orbital cycle number (from the first recorded eclipse). These diagrams are presented in Figure Set 1 (given in full in the electronic version). Each figure shows the mean light curve in the lower panel (extended in orbital phase to aid the sense of phase continuity) and presents the differences in a gray scale image in the upper panel. The gray intensity varies from the lowest point below the average (black) to the highest peak above the average (white) over a range in normalized flux given in each caption. Gaps in the time series are indicated by a uniform, mid-range gray intensity. The corresponding  $O - C$  diagrams are given Figure Set 2 (again given in full in the electronic version) for each binary in the sample. These display the measurements for the primary and secondary eclipses as + and  $\times$  symbols, respectively.

There are a number of features in these diagrams that are useful for the interpretation of the eclipse timing variations. Those binaries with slowly changing eclipse times are immediately detected in the gray scale diagrams in Figure Set 1 by the appearance of alternating regions of bright and dark intensity (over those parts of the eclipsing light curve where the absolute value of the time derivative is large). We assigned to the category of candidate third body systems those cases where the deviations in the secondary eclipse track those of the primary star’s changes and where  $|\dot{P}/P|$  is significantly larger than its error. These 16 systems are discussed on a case by case basis in the Appendix and are noted by letter T (candidate tertiary) in the last column of Table 1.

The system with the largest systematic variation is KID 9402652 (Fig. Set 2.26). Like the other candidates, the variation observed here has not yet completed one cycle over the two year duration of the *Kepler* observations. We made preliminary LITE fits for both the primary and secondary eclipses (shown as solid lines in Fig. Set 2.26), and we find a semiamplitude of  $119 \pm 25$  s, an eccentricity  $e = 0.58 \pm 0.04$ , a longitude of periastron  $\omega = 290 \pm 3$  deg, an epoch of periastron of BY 2009.1  $\pm$  0.1, and a period of  $3.1 \pm 0.3$  y for the third body reflex orbit. For an assumed total mass of  $2.7M_{\odot}$ , this yields a third star mass product of  $M_3 \sin i = 0.32 \pm 0.08 M_{\odot}$ . If correct, then the *Kepler* data have covered only two thirds of one orbit.

We found one system, KID 4544587 (Fig. Set 2.6), where the deviations in the secondary timings were a mirror image of those for the primary. This is an eccentric system ( $e = 0.31$ ; Slawson et al. 2011) where the secondary eclipse is well offset from phase 0.5 (Fig. Set 1.6). We think the simplest explanation is that we are detecting apsidal motion due to tidal effects, and we used the method of Lacy (1992) to fit a solution for the advance of perihelion. This fit yields parameters  $\omega = 313.3$  (at  $T = \text{BJD } 2,455,262.7977$ ),  $\dot{\omega} = 0.0001107$  (4) radians per sidereal period, and an apsidal period  $U = 340.3 \pm 1.3$  y. It is possible that some of this motion

might be caused by a third body (see eq. 60, 61, and 63 in Borkovits et al. 2011), but this is not a necessary component. We found, for example, that using structure constants  $k_2$  from Claret & Gimenez (1992) and estimates of the fractional radii from Slawson et al. (2011), the predicted apsidal period ranges from 180 y (for synchronous rotation at periastron) to 590 y (for rotation synchronous with the mean orbital motion). Consequently, we simply assumed that the eclipse timing variations are due only to the tidal apsidal advance (marked by A in the last column of Table 1), and this system was not counted among the candidate third body group. Less pronounced timing variations in two other binaries (KID 04851217 and 08196180) are probably related to apsidal motion.

There is ample evidence that many of the systems (containing stars with  $T_{\text{eff}} < 6500$  K) experience starspot activity. This is observed as flux variations outside eclipse that generally move with respect to the orbital period. We find examples where the spot rotation is faster than the orbit so that the spots are seen progressively earlier with each orbital cycle (KID 5444392, Fig. Set 1.13), slower than the orbit (KID 8552540, Fig. Set 1.21), and where both trends are visible (KID 09899416, Fig. Set 1.30). These apparent spot variations do influence the eclipse times (Kalimeris et al. 2002). For example, we see that the times when dark spot patterns cross the secondary eclipse in KID 5444392 (Fig. Set 1.13) correspond to extrema of the secondary’s  $O - C$  timings (Fig. Set 2.13). We detected such spot activity in 25 systems, and these are indicated by the letter S in the last column of Table 1.

We also found 23 cases where there were fast flux variations that are probably due to pulsations (Uytterhoeven et al. 2011). These appear in the gray scale diagrams with closely spaced brightness variations. In many of these cases, the brightness oscillations form coherent patterns in the gray scale diagrams, indicating that the pulsation periods have a harmonic or near-harmonic relationship to the orbital period (for example, KID 3440230, Fig. Set 1.5), as was found for the remarkable binary HD 187091 (KID 8112039 = KOI-54) by Welsh et al. (2011).

In order to search for possible evidence of periodic signals in the  $O - C$  residuals, we calculated the power spectra of the  $O - C$  measurements for each target (for  $P > 10$  d). In general, no significant periodicities were found with the exceptions of those with starspot activity (where the periodicities corresponded to the intervals between spot crossing at times of eclipse) and two pulsator cases. We found periods of 40.4 d and 26.6 d for KID 8553788 and 9592855, respectively, and these can be seen to be the intervals between successive large pulsation peaks crossing the eclipses in these near-resonant cases (see Fig. Set 1.22, 1.27). The binaries displaying pulsation are indicated by the letter P in the final column of Table 1, and their actual pulsation amplitudes are probably large since they were detected in long cadence data that averages over 29 minutes of flux variability.

Slawson et al. (2011) and Welsh et al. (2012) found a few cases of *Kepler* observations of eclipsing binaries where extra eclipses were seen from transits of tertiary stars. We made a rudimentary search for such transits by comparing the difference fluxes from the mean eclipse curve with a smoothed version of the same and by identifying any observations where three consecutive measurements were significantly lower than expected (minimum more than three standard deviations below). No events were identified through this scheme. It is certainly possible that smaller amplitude transits were missed, but we would have found any transits with amplitudes as large as those detected by Slawson et al. (2011) (see their Fig. 3).

#### 4. Discussion

We cannot at this stage claim that the period variations of all the third body candidates are actually due to orbital motion. Such a statement must await a longer time span of observations that shows true periodic variability in the  $O - C$  residuals for both eclipses. In the meantime, we caution that long-term secular variations associated with mass exchange, systemic mass loss, tidal dissipation, and magnetic cycles may be present in some systems (Tokovinin et al. 2006; Pilecki et al. 2007; Zakirov 2010). However, there are some situations where the evidence does indeed point towards the third body explanation. For example, the system with the largest  $|\dot{P}/P|$ , KID 04848423 (Fig. Set 2.11), shows systematic differences between the primary and secondary eclipse curves that may result from the dynamical effects of the third star (Borkovits et al. 2011). Another target, KID 02708156 = UZ Lyr, has a very long observational history of eclipse timings, and the *Kepler* estimate of  $\dot{P}/P$  is consistent with a periodic  $O - C$  variation but is inconsistent with a secular variation. Thus, we think it is appropriate to consider all the long-term variable systems as candidates for a tertiary companion.

It is also important to review the selection effects associated with this study. First, any system with a third body will show a periodic  $O - C$  variation that will have both locally linear and curved sections. Since our selection of candidates is based upon only detecting curvature in the  $O - C$  diagram, we will miss any systems that were observed in the locally linear part of their cycle (compensated for by our choice of period that keeps the  $O - C$  curve flat over the duration of the observations). Second, the current observational window covers only about two years, so the results are relatively insensitive to motion in orbits with much longer periods, because the changes will be minor over this time span.

We show examples of the predicted variations in Figure 3 that shows the semiamplitude as a function of outer orbital period for several assumed tertiary masses. The solid lines

show the LITE semiamplitude,

$$\frac{m_3}{m_{123}} \frac{a_2 \sin i}{c} (1 - e_2^2)$$

where  $m_3/m_{123}$  is the fractional mass of the third star compared to the total mass of the system,  $a_2$  is the semimajor axis,  $i$  is the inclination and  $e_2$  is the eccentricity of the outer orbit, and  $c$  is the speed of light (Borkovits et al. 2011). For the purpose of this figure, we assumed an inner binary mass of  $3M_\odot$ ,  $\sin i = \pi/4$ , and a circular outer orbit ( $e_2 = 0$ ). The dashed lines show the semiamplitude of the dynamical terms,

$$\frac{15}{8} \frac{m_3}{m_{123}} \frac{P_1}{P_2} (1 - e_2^2)^{-3/2} \frac{P_1}{2\pi} (1 - e_1^2)^{1/2}$$

where  $P_1$  and  $P_2$  are the periods of the inner and outer systems (Borkovits et al. 2011). Again for illustration, we assumed representative values  $e_1 = e_2 = 0$  and  $P_1 = 1.5$  d. The plus sign marks the preliminary results for KID 09402652. We see that with timing results accurate to a few tens of seconds, we should have been able to detect LITE variations for companions as small as  $0.2M_\odot$  with periods  $> 200$  d, and we might have found dynamical variations for such stars with periods  $< 200$  d. The lack of detected systems with  $P < 1000$  d probably means that such tertiary systems are rare.

The lack of short period companions is consistent with other results on tertiary companions of spectroscopic binaries (Tokovinin et al. 2006) and on those previously found through LITE methods (Zakirov 2010). Tokovinin et al. (2006) made an adaptive optics survey of nearby, spectroscopic binaries consisting of solar-type stars. They found that the frequency of tertiaries was 63% for the whole sample and rose to 96% for systems where the close binary period was less than 3 d. Based on their results, we would expect that most of the eclipsing binaries in our sample have tertiary companions. However, most of these tertiaries have long orbital periods (with a mean value of 32 y in the sample of Zakirov 2010), and only 11% (Zakirov 2010) to 15% (Tokovinin et al. 2006) of these triples have outer periods of less than 10 y. Thus, if we assume that all of the eclipsing binaries in our sample are triple, then we would have expected to find only 4 to 6 systems in the period range we can detect, much smaller than the 14 candidates we present here. We suspect that the discrepancy may result from the lack of detection of lower mass tertiaries at lower periods in the earlier work and/or our likely inclusion of candidate systems whose variability actually has an origin unrelated to a tertiary.

Our results appear to be consistent with the general occurrence of tertiary companions to close binaries, provided that most of these have periods longer than a few years. This agrees with theoretical results that dynamically stable, hierarchical systems have a large ratio of outer to inner period (Holman & Wiegert 1999; Mardling & Aarseth 2001) and with observational studies that show that low values of the ratio are rare (for example, the smallest



ratio was  $P_2/P_1 \approx 1000$  in the survey of Tokovinin et al. 2006). We are currently involved in a moderate resolution spectroscopic study of all the eclipsing binaries in the sample presented here. We will make complete light and radial velocity curve studies of the targets, and this may aid detection of tertiaries. Once allowance is made for the flux any nearby stars within the *Kepler* point spread function, the light curve analysis will include a potential third-light component that acts to dilute (weaken) the eclipse depths. A tertiary might also be detected spectroscopically through the flux dilution of the spectral lines (making the lines of the primary and secondary appear weaker than expected) and/or through detection of the tertiary’s relatively stationary spectral lines. Such results will provide additional constraints on the flux of any tertiaries as well as accurate masses and other parameters for the stars in the close binaries.

We are grateful for the support of Martin Still and the staff of the *Kepler* Guest Observer Office. We also thank Natalie Batalha, for sharing her VULCAN results on eclipsing binaries in advance of publication, and the referee Pavel Mayer, whose comments were particularly helpful. *Kepler* was competitively selected as the tenth Discovery mission. Funding for this mission is provided by NASA’s Science Mission Directorate. This study was supported by NASA grants NNX10AC39G, NNX11AB70G, and NNX12AC81G. The data presented in this paper were obtained from the Multimission Archive at the Space Telescope Science Institute (MAST). STScI is operated by the Association of Universities for Research in Astronomy, Inc., under NASA contract NAS5-26555. Support for MAST for non-HST data is provided by the NASA Office of Space Science via grant NAG5-7584 and by other grants and contracts.

Facilities: Kepler

### A. Notes on Individual Stars

*KID 02305372*. A similar period was found in both the HATNET (Hartman et al. 2004) and ASAS surveys (Pigulski et al. 2009). Both the primary and secondary  $O - C$  measurements show a significant positive parabolic trend. However, there is a slowly varying trend in the light curve residuals that probably results from starspot activity and leads to differences in the primary and secondary  $O - C$  measurements.

*KID 02708156*. This star, UZ Lyr, has many eclipse measurements going back to 1920 that are listed by Kreiner et al. (2001). There are oscillations in the historic  $O - C$  measurements that have an amplitude of  $\approx 900$  s, so the parabolic trends in the *Kepler* data are probably related to changes on decadal time scales. There are faster ( $\approx 100$  d) variations in the

secondary  $O - C$  measurements that are due to starspots. Vesper et al. (2001) note the presence of  $H\alpha$  emission in this Algol-type system.

*KID 03241619.* A similar period was found in the HATNET survey. The light curve is strongly modulated by migrating starspots that clearly influence the  $O - C$  timings for both eclipses.

*KID 03327980.* The VULCAN survey (Mjaseth et al. 2007) determined a similar period and ephemeris. Beyond quarter to quarter systematic differences, there is no evidence of significant variability in the  $O - C$  measurements.

*KID 03440230.* The star was identified in the VULCAN survey with twice the actual orbital period. Both primary and secondary  $O - C$  timings indicate a negative periodic trend, but starspot activity appears to influence the results for the secondary.

*KID 04544587.* Similar periods were found for this eccentric system in both the VULCAN and ASAS surveys. The  $O - C$  measurements have opposite trends for the primary and secondary as expected for apsidal motion. Both the primary and secondary  $O - C$  timings are affected by resonant pulsations described by Hambleton et al. (2011)<sup>1</sup>.

*KID 04574310.* Similar periods were determined in the HATNET and ASAS surveys. The light curve is dominated by starspot activity that especially influences the secondary eclipse times.

*KID 04660997.* This star V1130 Cyg has the shortest period in our sample. The first published period from Miller (1966) of 0.562561247 (48) d is about  $4\sigma$  longer than we and Kreiner (2004) find. The  $O - C$  measurements show fluctuations related to starspot activity on both stars.

*KID 04665989.* A similar period was found in the ASAS survey. There are slight systematic variations in the light curves between quarters, and the gray scale representation of the light curve suggests that pulsation is present.

*KID 04678873.* The *Kepler* period is similar to that found in the HATNET and ASAS surveys. The light curve shows evidence of pulsation that introduces scatter into the  $O - C$  timings of the eclipses. This target has a close visual companion that is located  $5''.1$  north and that is 0.9 mag fainter in the UCAC3 catalog (Zacharias et al. 2010), and the influence of blending varies with each quarter.

*KID 04848423.* There are only two quarters available currently, but this target shows the

---

<sup>1</sup><http://kepler.nasa.gov/Science/ForScientists/keplerconference/sessions/>

largest period changes of any in our sample. The period appears to be increasing, yet the period from *Kepler* is slightly lower than that found in the HATNET and ASAS surveys (where the presumed period was set at twice the actual value). There appear to be small but significant differences in the  $O - C$  timings of the primary and secondary that hint that dynamical effects from a third body are present. Some modest starspot activity is also indicated in the gray scale diagram of the light curve.

*KID 04851217*. This star, HDE 225524, shows fast variability related to pulsation. The  $O - C$  measurements show a modest sign reversal over the course of the *Kepler* observations that are opposite for the primary and secondary eclipses. The light curve (Fig. Set 1.12) shows that the secondary eclipse occurs early (near phase 0.48), consistent with a non-zero eccentricity. This is a candidate apsidal motion system.

*KID 05444392*. A similar period was estimated in the HATNET and ASAS surveys. The  $O - C$  variations are closely related to starspot changes evident in the gray scale depiction of the light curve.

*KID 05513861*. The ASAS catalog reports a similar period. The  $O - C$  curves for both the primary and secondary eclipses show a large, positive curvature that requires a cubic polynomial for an acceptable fit. These variations may be caused by motion about a third body. There is also evidence of rapid flux variability related to pulsation.

*KID 05621294*. A similar period was established by the VULCAN survey. The light curve shows rapid variability related to pulsation of the primary star (plus some modest starspot activity). The pulsations influence the  $O - C$  measurements, but there also appears to be a negative parabolic trend in the  $O - C$  timings of both components (with systematic differences evident at both extremes of the observing window). This is suggestive of changes related to a third body.

*KID 05738698*. Similar periods were found by HATNET and ASAS (half the actual period for ASAS). This is a hint of longer pulsation periods ( $\approx 2P$ ) in the gray scale diagram of the light curve.

*KID 06206751*. The *Kepler* period agrees with earlier results from HATNET and ASAS. There is evidence of both pulsation and starspot activity in the gray scale light curve. The  $O - C$  timings suggest a low amplitude and negative curvature for both components that may be indicative of a third body.

*KID 07368103*. The VULCAN survey found a period equal to twice the actual one. There is clear evidence of fast pulsation in the light curve as well as low-level starspot activity.

*KID 08196180*. This is an eccentric system with narrow eclipses. The VULCAN survey

found a similar period. The light curve shows evidence of both starspot and pulsational modulation. The periods derived from the  $O - C$  diagram are significantly different for the primary and secondary, and this may imply a very long term variation due to apsidal motion (probably consistent with the small radii,  $R/a$ , indicated by the narrow eclipses).

*KID 08262223.* The *Kepler* and VULCAN period results agree. The light curve is modulated by pulsation in near resonance with the orbit. The wander in the  $O - C$  values probably results from the pulsational variations.

*KID 08552540.* This eclipsing binary, V2277 Cyg, was discovered by Diethelm (2001), and the periods from TrES (Devor et al. 2008), ASAS, and *Kepler* all agree. The light curve is modulated by starspot activity in both stars, and the apparent  $O - C$  variations track the starspot evolution.

*KID 08553788.* There is good agreement among the periods from ASAS, VULCAN, and *Kepler*. The gray scale depiction of the light curve shows that there is near resonant pulsation in the primary, and there is probably starspot activity in both stars. The  $O - C$  timings are influenced by both pulsation and starspots, but there is also a marked negative curvature in the both sets of  $O - C$  measurements. We tentatively suggest that the latter is due to a third body.

*KID 08823397.* The period from VULCAN agrees with the *Kepler* result. Apart from quarter to quarter systematic differences, the light curve and  $O - C$  trends look stable.

*KID 09159301.* VULCAN estimated a period twice the actual one. This star displays rapid pulsations (which may form a near resonant beat pattern in the more recent data) and starspot activity in the light curve. The  $O - C$  timings of the primary show a positive curvature that we tentatively assume is related to third body effects.

*KID 09357275.* The VULCAN and *Kepler* periods agree. The light curve is shaped by starspot activity that is readily seen in the  $O - C$  measurements for secondary eclipse. There are also quarter to quarter systematic differences in the secondary eclipse depth.

*KID 09402652.* V2281 Cyg was discovered as an eclipsing binary by Diethelm (2001). The orbital period estimates from ASAS, WASP (Payne et al. 2012)<sup>2</sup>, and *Kepler* all agree. Both the primary and secondary  $O - C$  values display a large amplitude and negative curvature trend. The curve is not well matched with a parabola, but it can be reproduced as the light travel time effect of motion about a third star (§3).

*KID 09592855.* All the estimates of period from ASAS, VULCAN, and *Kepler* are in agree-

---

<sup>2</sup><http://wasp.paynescape.com>

ment. The light curve shows rapid variations presumably due to pulsation.

*KID 09602595.* The first period determination for V995 Cyg was made by Strohmeier (1963), and the star has been well observed since. The *Kepler* period is close to the estimate of 3.556509 d from Kreiner (2004). The light curve is influenced by starspots that result in an especially large  $O - C$  variation for the secondary eclipse. The presence of negative curvature in the primary eclipse  $O - C$  and of large  $O - C$  residuals in the historical record (Kreiner et al. 2001) suggest that a third body may contribute to the observed variations.

*KID 09851944.* The ASAS and *Kepler* periods are the same. This system displays near harmonic pulsational variability, possibly on both stars.

*KID 09899416.* BR Cyg has a long history of eclipse timings that show variations as large as  $\approx 1000$  s (Kreiner et al. 2001). The *Kepler* period agrees with the historical value from Kreiner (2004). A multicolor study of the light curve was made by Terrell & Gross (2005). The *Kepler* light curve shows the presence of starspot activity that moves both ahead and behind the orbital period advance. Most of the eclipse timing variations are probably related to the starspot activity.

*KID 10156064.* The period from VULCAN matches the *Kepler* result. There is some evidence of starspot activity in the light curve diagram, but the eclipse timings show no obvious variability.

*KID 10191056.* The periods from ASAS, TrES, and *Kepler* are all consistent. The periods from the primary and secondary differ by a small but significant amount. The eclipses are narrow and thus the radii are relatively small, so we suspect that apsidal motion cannot be the explanation. A third body dynamical perturbation is a possible cause.

*KID 10206340.* The periods from ASAS, Kreiner (2004), and *Kepler* are in agreement for this system, V850 Cyg. The light curve diagram reveals starspot activity associated with the primary, and there is evidence of pulsation that is best seen around orbital phase 0.25. Uytterhoeven et al. (2011) suggest that this is a  $\gamma$  Dor pulsator. The large excursions in the  $O - C$  timings are associated with the starspot features in the light curve.

*KID 10486425.* The periods from VULCAN, TrES, and *Kepler* are consistent with each other. The light curve shows evidence of pulsation (probably related to the primary), and short-term trends in the  $O - C$  measurements are due to the net flux changes associated with these pulsations.

*KID 10581918.* This system is WX Dra, and the periods from Kreiner (2004), ASAS, TrES, and *Kepler* all agree. The light curve, gray scale diagram shows slowly evolving, starspot structures that affect the  $O - C$  timings.

*KID 10619109.* The period estimates from *Kepler*, TrES, and VULCAN are consistent (although twice the period is reported for VULCAN). The light curve shows starspot activity and low amplitude pulsation. The primary and secondary periods are different, but this is probably due to the larger influence of starspots at the beginning and ending of the time series.

*KID 10661783.* The derived periods from ASAS and *Kepler* are identical. Pulsations are prominent in the light curve of this totally eclipsing system.

*KID 10686876.* The VULCAN, TrES, and *Kepler* periods are consistent. The light curve of this totally eclipsing binary shows starspot and pulsational activity. Furthermore, both primary and secondary  $O - C$  measurements display a negative curvature (the differences between the two sets are probably due to starspot activity). This may result from the influence of a third body.

*KID 10736223.* The period of V2290 Cyg was first determined by Guilbault et al. (2001) using observations made over a 73 y range, and the light curve was subsequently analyzed by Pazhouhesh & Edalati (2002). The periods from Kreiner (2004) and *Kepler* are slightly less than that from Guilbault et al. (2001). The *Kepler* light curve displays variations from starspots and pulsation. Furthermore, both the primary and secondary  $O - C$  data show a net positive curvature, implying a slightly increasing period. These facts suggest that the changes are related to a third body.

*KID 10858720.* The periods for V753 Cyg are consistent among the estimates from Kreiner (2004), ASAS, and *Kepler*. The light curve indicates the primary is a pulsator, but the  $O - C$  timings appear relatively constant. Kaitchuck et al. (1985) checked for  $H\alpha$  emission from circumstellar gas but found none.

*KID 12071006.* The period of V379 Cyg was first determined by Belyawsky (1936), but the system has had little attention since then. This is the longest period system in the sample, and it has a very deep primary eclipse. The light curve shows evidence of pulsation and starspots. The primary  $O - C$  timings show a slight negative curvature, but we suspect this is due to the characteristics of the starspots near the beginning of the observations.

## REFERENCES

- Belyawsky, S. 1936, *Perem. Zvezdy*, 5, 36
- Borkovits, T., Csizmadia, S., Forgács-Dajka, E., & Hegedüs, T. 2011, *A&A*, 528, A53
- Borucki, W. J., Caldwell, D., Koch, D. G., et al. 2001, *PASP*, 113, 439

- Claret, A., & Gimenez, A. 1992, *A&AS*, 96, 255
- Devor, J., Charbonneau, D., O’Donovan, F. T., Mandushev, G., & Torres, G. 2008, *AJ*, 135, 850
- Diethelm, R. 2001, *Information Bulletin on Variable Stars*, 5060, 1
- Doyle, L. R., Carter, J. A., Fabrycky, D. C., et al. 2011, *Science*, 333, 1602
- Eggleton, P. P., & Kiseleva-Eggleton, L. 2001, *ApJ*, 562, 1012
- Guilbault, P. R., Henden, A. A., Billings, G. W., et al. 2001, *Information Bulletin on Variable Stars*, 5018, 1
- Hambleton, K., Kurtz, D., Prša, A., Bloeman, S., & Southworth, J. 2011, in *Kepler Science Conference - NASA Ames Research Center*, 180
- Hartman, J. D., Bakos, G., Stanek, K. Z., & Noyes, R. W. 2004, *AJ*, 128, 1761
- Hoffman, D. I., Harrison, T. E., McNamara, B. J., et al. 2006, *AJ*, 132, 2260
- Holman, M. J., & Wiegert, P. A. 1999, *AJ*, 117, 621
- Irwin, J. B. 1959, *AJ*, 64, 149
- Kaitchuck, R. H., Honeycutt, R. K., & Schlegel, E. M. 1985, *PASP*, 97, 1178
- Kalimeris, A., Rovithis-Livaniou, H., & Rovithis, P. 2002, *A&A*, 387, 969
- Kepler Mission Team. 2009, *VizieR Online Data Catalog*, 5133, 0
- Kouwenhoven, M. B. N., Brown, A. G. A., Portegies Zwart, S. F., & Kaper, L. 2007, *A&A*, 474, 77
- Kratter, K. M., Matzner, C. D., Krumholz, M. R., & Klein, R. I. 2010, *ApJ*, 708, 1585
- Kreiner, J. M. 2004, *Acta Astron.*, 54, 207
- Kreiner, J. M., Kim, C.-H., & Nha, I.-S. 2001, *An Atlas of O-C Diagrams of Eclipsing Binary Stars*
- Krumholz, M. R., Klein, R. I., McKee, C. F., Offner, S. S. R., & Cunningham, A. J. 2009, *Science*, 323, 754
- Lacy, C. H. S. 1992, *AJ*, 104, 2213

- Larson, R. B. 2002, *MNRAS*, 332, 155
- Lee, J. W., Kim, S.-L., Kim, C.-H., et al. 2009, *AJ*, 137, 3181
- Liao, W.-P., & Qian, S.-B. 2010, *MNRAS*, 405, 1930
- Mardling, R. A., & Aarseth, S. J. 2001, *MNRAS*, 321, 398
- Mason, B. D., Gies, D. R., Hartkopf, W. I., et al. 1998, *AJ*, 115, 821
- Matt, S., & Pudritz, R. E. 2005, *ApJ*, 632, L135
- Mayer, P. 2004, in *Astronomical Society of the Pacific Conference Series*, Vol. 318, *Spectroscopically and Spatially Resolving the Components of the Close Binary Stars*, ed. R. W. Hilditch, H. Hensberge, & K. Pavlovski, 233–241
- Miller, W. J. 1966, *Ricerche Astronomiche*, 7, 217
- Mjaseth, K., Batalha, N., Borucki, W., et al. 2007, in *Bulletin of the American Astronomical Society*, Vol. 38, *American Astronomical Society Meeting Abstracts #210*, 98
- Özdemir, S., Mayer, P., Drechsel, H., Demircan, O., & Ak, H. 2003, *A&A*, 403, 675
- Payne, S. G., Norton, A. J., Wheatley, P. J., et al. 2012, *Astronomical Journal*, submitted
- Pazhouhesh, R., & Edalati, M. T. 2002, *Astronomische Nachrichten*, 323, 462
- Pigulski, A., Pojmański, G., Pilecki, B., & Szczygieł, D. M. 2009, *Acta Astron.*, 59, 33
- Pilecki, B., Fabrycky, D., & Poleski, R. 2007, *MNRAS*, 378, 757
- Pribulla, T., Chochol, D., Tremko, J., & Kreiner, J. M. 2005, in *Astronomical Society of the Pacific Conference Series*, Vol. 335, *The Light-Time Effect in Astrophysics: Causes and cures of the O-C diagram*, ed. C. Sterken, 103
- Pribulla, T., & Rucinski, S. M. 2006, *AJ*, 131, 2986
- Prša, A., Batalha, N., Slawson, R. W., et al. 2011, *AJ*, 141, 83
- Raghavan, D., McAlister, H. A., Henry, T. J., et al. 2010, *ApJS*, 190, 1
- Slawson, R. W., Prša, A., Welsh, W. F., et al. 2011, *AJ*, 142, 160
- Strohmeier, W. 1963, *Information Bulletin on Variable Stars*, 32, 1
- Terrell, D., & Gross, J. 2005, *Information Bulletin on Variable Stars*, 5646, 1



- Tokovinin, A., Thomas, S., Sterzik, M., & Udry, S. 2006, *A&A*, 450, 681
- Uytterhoeven, K., Moya, A., Grigahcène, A., et al. 2011, *A&A*, 534, A125
- Vesper, D., Honeycutt, K., & Hunt, T. 2001, *AJ*, 121, 2723
- Welsh, W. F., Orosz, J. A., Aerts, C., et al. 2011, *ApJS*, 197, 4
- Welsh, W. F., Orosz, J. A., Carter, J. A., et al. 2012, *Nature*, 481, 475
- Zacharias, N., Finch, C., Girard, T., et al. 2010, *AJ*, 139, 2184
- Zakirov, M. M. 2010, *Kinematics and Physics of Celestial Bodies*, 26, 269
- Zavala, R. T., McNamara, B. J., Harrison, T. E., et al. 2002, *AJ*, 123, 450
- Zinnecker, H., & Yorke, H. W. 2007, *ARA&A*, 45, 481

Table 1. Eclipsing Binary Properties

KID	$I$ (s)	$E$ (s)	$P_a$ (d)	$T$ (BJD-2,400,000)	$P$ (d)	$\dot{P}/P$ ( $10^{-6} \text{ y}^{-1}$ )	Comment <sup>a</sup>
2305372P	5.1	60.7	1.4046774	55075.52509 (6)	1.404678238 (8)	9.45 (4)	Q, S, T
2305372S	20.4	96.6	...	55587.5342 (6)	1.40467658 (5)	15.4 (2)	...
2708156P	2.8	39.8	1.8912670	55438.49951 (2)	1.89127025 (1)	2.29 (2)	S, T
2708156S	17.8	46.5	...	55227.6235 (3)	1.89126366 (7)	-1.9 (1)	...
3241619P	14.3	34.2	1.7033444	55159.64932 (6)	1.70334416 (3)	2.20 (7)	S
3241619S	41.4	44.2	...	55574.4141 (7)	1.70334564 (5)	2.7 (2)	...
3327980P	5.2	2.6	4.2310219	55411.36394 (7)	4.23102181 (9)	0.01 (9)	Q
3327980S	6.4	2.9	...	55735.03527 (9)	4.2310220 (1)	-0.1 (1)	...
3440230P	4.6	48.5	2.8811205	55537.69744 (3)	2.88111953 (3)	-8.23 (6)	S, T
3440230S	27.2	86.8	...	55057.9937 (2)	2.8811285 (2)	-2.0 (3)	...
4544587P	4.8	150.5	2.1891140	55341.60581 (4)	2.18909716 (3)	0.38 (5)	A, P
4544587S	3.8	149.8	...	55358.35084 (3)	2.18913086 (2)	-0.17 (3)	...
4574310P	1.8	4.8	1.3062191	55235.49909 (2)	1.306218991 (4)	-0.18 (1)	S
4574310S	6.2	18.6	...	55614.9559 (1)	1.30621925 (1)	-0.12 (4)	...
4660997P	16.9	43.8	0.5625604	55177.9496 (3)	0.562560545 (6)	1.15 (3)	S
4660997S	22.7	53.5	...	55009.4630 (1)	0.562560116 (4)	-0.94 (3)	...
4665989P	1.6	1.4	2.2480675	55626.68385 (2)	2.248067537 (8)	0.02 (1)	Q, P
4665989S	2.3	2.2	...	55540.13337 (3)	2.24806754 (1)	0.01 (2)	...
4678873P	24.4	47.0	1.8788771	55486.5223 (3)	1.8788767 (1)	-0.1 (2)	Q, P
4678873S	160.4	375.3	...	55579.525 (2)	1.87887732 (5)	10.4 (1)	...
4848423P	3.5	11.1	3.0035189	55505.20125 (5)	3.0035202 (4)	34. (2)	S, T
4848423S	4.9	11.0	...	55608.82124 (7)	3.0035184 (5)	43. (3)	...
4851217P	62.6	13.1	2.4702796	55487.4806 (6)	2.4702807 (4)	0.8 (7)	A, P
4851217S	45.5	11.2	...	55093.4215 (7)	2.4702788 (3)	0.9 (5)	...
5444392P	11.4	29.3	1.5195281	55609.83190 (4)	1.51952822 (2)	-0.68 (6)	S
5444392S	15.5	44.3	...	55569.5644 (1)	1.51952794 (4)	-1.36 (9)	...
5513861P	1.3	34.2	1.5101839	55500.17856 (2)	1.510184171 (5)	8.53 (1)	P, T
5513861S	1.1	33.7	...	55111.306244 (4)	1.510183743 (4)	7.83 (1)	...
5621294P	7.4	15.7	0.9389071	54989.2511 (1)	0.938906670 (9)	-1.73 (5)	P, S, T
5621294S	45.7	60.0	...	55657.2851 (7)	0.93890760 (3)	-5.6 (1)	...
5738698P	4.8	1.6	4.8087740	55100.85490 (5)	4.8087739 (1)	0.02 (7)	P, Q
5738698S	4.5	2.5	...	55189.81827 (5)	4.80877398 (9)	0.03 (7)	...
6206751P	13.0	25.5	1.2453439	55702.4624 (2)	1.24534410 (2)	-1.34 (5)	P, S, T
6206751S	28.6	58.2	...	55510.0573 (1)	1.24534372 (5)	-0.7 (1)	...
7368103P	81.2	30.2	2.1825141	55445.506 (2)	2.1825156 (4)	-0.6 (8)	P, S
7368103S	317.8	470.6	...	55084.300 (7)	2.1825116 (1)	-6.8 (3)	...
8196180P	5.1	8.4	3.6716598	55372.64452 (5)	3.67166118 (5)	0.00 (6)	A, P, S
8196180S	13.9	25.9	...	55465.9158 (1)	3.6716584 (1)	0.3 (2)	...
8262223P	6.1	6.3	1.6130147	55430.90874 (8)	1.61301466 (2)	-0.10 (5)	P, Q
8262223S	15.9	16.4	...	55694.63694 (7)	1.61301467 (5)	-0.1 (1)	...
8552540P	9.6	23.7	1.0619344	55471.26705 (3)	1.06193406 (1)	0.06 (4)	S
8552540S	13.8	28.7	...	55610.9120 (2)	1.06193481 (1)	-0.08 (5)	...
8553788P	3.9	23.2	1.6061743	55046.54573 (7)	1.60617393 (1)	-4.04 (3)	P, S, T
8553788S	23.5	42.6	...	55142.1194 (2)	1.60617473 (8)	-3.7 (2)	...
8823397P	1.0	1.0	1.5065037	55440.539331 (8)	1.506503705 (3)	0.006 (7)	Q

Table 1—Continued

KID	$I$ (s)	$E$ (s)	$P_a$ (d)	$T$ (BJD-2,400,000)	$P$ (d)	$\dot{P}/P$ ( $10^{-6} \text{ y}^{-1}$ )	Comment <sup>a</sup>
8823397S	2.3	3.4	...	55646.17738 (3)	1.506503679 (7)	0.04 (2)	...
9159301P	12.1	17.4	3.0447717	55726.6290 (1)	3.0447698 (1)	1.4 (1)	P, S, T
9159301S	128.0	125.9	...	55645.9444 (9)	3.04477509 (3)	2.6 (1)	...
9357275P	1.7	1.7	1.5882981	55573.50073 (3)	1.588298146 (5)	0.07 (1)	Q, S
9357275S	9.4	15.9	...	55378.9344 (1)	1.58829803 (3)	0.13 (9)	...
9402652P	0.9	53.9	1.0731136	55132.422059 (5)	1.073113953 (2)	-10.227 (6)	T
9402652S	1.0	53.5	...	55135.10484 (1)	1.073113272 (2)	-10.182 (6)	...
9592855P	10.9	20.8	1.2193248	55656.3029 (1)	1.21932475 (2)	-1.65 (5)	P, Q
9592855S	13.2	22.9	...	55424.0215 (1)	1.21932480 (3)	-0.46 (8)	...
9602595P	2.0	51.0	3.5565240	55375.52022 (1)	3.55651727 (2)	-3.32 (2)	S, T
9602595S	13.1	103.2	...	54993.1977 (2)	3.5565296 (2)	-11.3 (2)	...
9851944P	14.5	16.1	2.1639018	55345.3670 (2)	2.16390189 (8)	-0.2 (1)	P
9851944S	14.9	14.9	...	55339.9571 (1)	2.16390178 (8)	0.1 (1)	...
9899416P	2.1	10.2	1.3325638	55248.88593 (2)	1.332564453 (5)	0.19 (1)	Q, S
9899416S	4.1	22.0	...	55532.05579 (9)	1.332563116 (9)	-0.13 (2)	...
10156064P	4.5	3.2	4.8559364	54988.44967 (5)	4.85593639 (9)	0.01 (8)	Q, S
10156064S	4.6	3.2	...	55413.34462 (6)	4.85593643 (9)	0.04 (8)	...
10191056P	1.6	1.7	2.4274949	55120.10058 (2)	2.42749482 (1)	-0.03 (2)	Q, T
10191056S	1.8	1.6	...	55521.85228 (1)	2.42749498 (1)	-0.03 (2)	...
10206340P	13.5	123.3	4.5643870	55691.8342 (2)	4.5643908 (2)	5.5 (2)	P, S
10206340S	24.8	180.6	...	55137.26033 (7)	4.5643817 (3)	-3.4 (3)	...
10486425P	29.1	94.1	5.2748090	55091.0297 (7)	5.2748069 (4)	2.1 (4)	P
10486425S	51.6	232.2	...	55452.353 (1)	5.274813 (1)	0. (2)	...
10581918P	5.0	21.5	1.8018650	55434.86895 (4)	1.80186287 (3)	-0.45 (9)	Q, S
10581918S	31.4	90.6	...	55396.1296 (2)	1.8018668 (2)	-2.5 (5)	...
10619109P	8.5	33.0	2.0451630	55086.03015 (9)	2.04516121 (4)	1.5 (1)	P, Q, S
10619109S	45.4	137.1	...	55631.0696 (7)	2.04516339 (2)	-0.14 (4)	...
10661783P	29.1	9.0	1.2313633	55102.7180 (4)	1.23136331 (5)	0.0 (2)	P, Q
10661783S	55.6	21.1	...	54974.0406 (3)	1.2313633 (1)	0.2 (3)	...
10686876P	3.2	39.6	2.6184286	55111.05523 (3)	2.61842922 (2)	-6.99 (4)	P, Q, S, T
10686876S	14.8	53.4	...	55591.5375 (1)	2.6184274 (1)	-8.5 (2)	...
10736223P	4.0	14.9	1.1050922	55136.83544 (4)	1.105091980 (7)	2.58 (3)	P, Q, S, T
10736223S	24.6	28.4	...	55145.1241 (3)	1.10509236 (4)	2.6 (2)	...
10858720P	2.6	5.5	0.9523776	55502.47547 (3)	0.952377636 (4)	-0.07 (2)	P, Q
10858720S	2.2	4.4	...	55137.23868 (2)	0.952377592 (3)	0.04 (1)	...
12071006P	9.3	16.2	6.0960140	55181.39070 (6)	6.096022 (2)	-19. (3)	P, Q, S
12071006S	140.0	182.3	...	55172.245 (1)	6.09600 (2)	-63. (46)	...

<sup>a</sup>A = apsidal motion; P = pulsation; Q = systematic variations between quarters; S = starspots; T = candidate third body system.

Table 2.  $O - C$  Eclipse Timing Measurements<sup>a</sup>

KID Number	$T_E$ (BJD-2,400,000)	Eclipse Type	$O - C$ (s)	$\sigma(O - C)$ (s)
2305372	54965.26211	2	-3.1	39.9
2305372	54965.96025	1	26.4	1.6
2305372	54966.66678	2	25.4	45.8
2305372	54967.36493	1	26.8	1.6
2305372	54968.07146	2	6.4	42.9
2305372	54968.76960	1	27.5	2.1
2305372	54969.47614	2	69.2	43.3
2305372	54970.17428	1	26.2	2.3
2305372	54970.88082	2	0.9	36.8
2305372	54971.57896	1	26.5	1.2
2305372	54972.28549	2	17.5	43.4
2305372	54972.98364	1	27.9	1.1
2305372	54973.69017	2	10.7	40.2
2305372	54974.38831	1	30.0	1.7
2305372	54975.09485	2	90.6	51.1
2305372	54975.79299	1	27.5	2.1

<sup>a</sup>The full table is available in the electronic version.

**Fig. Set 1. Light curve variations**

**Fig. Set 2. Eclipse timing variations**

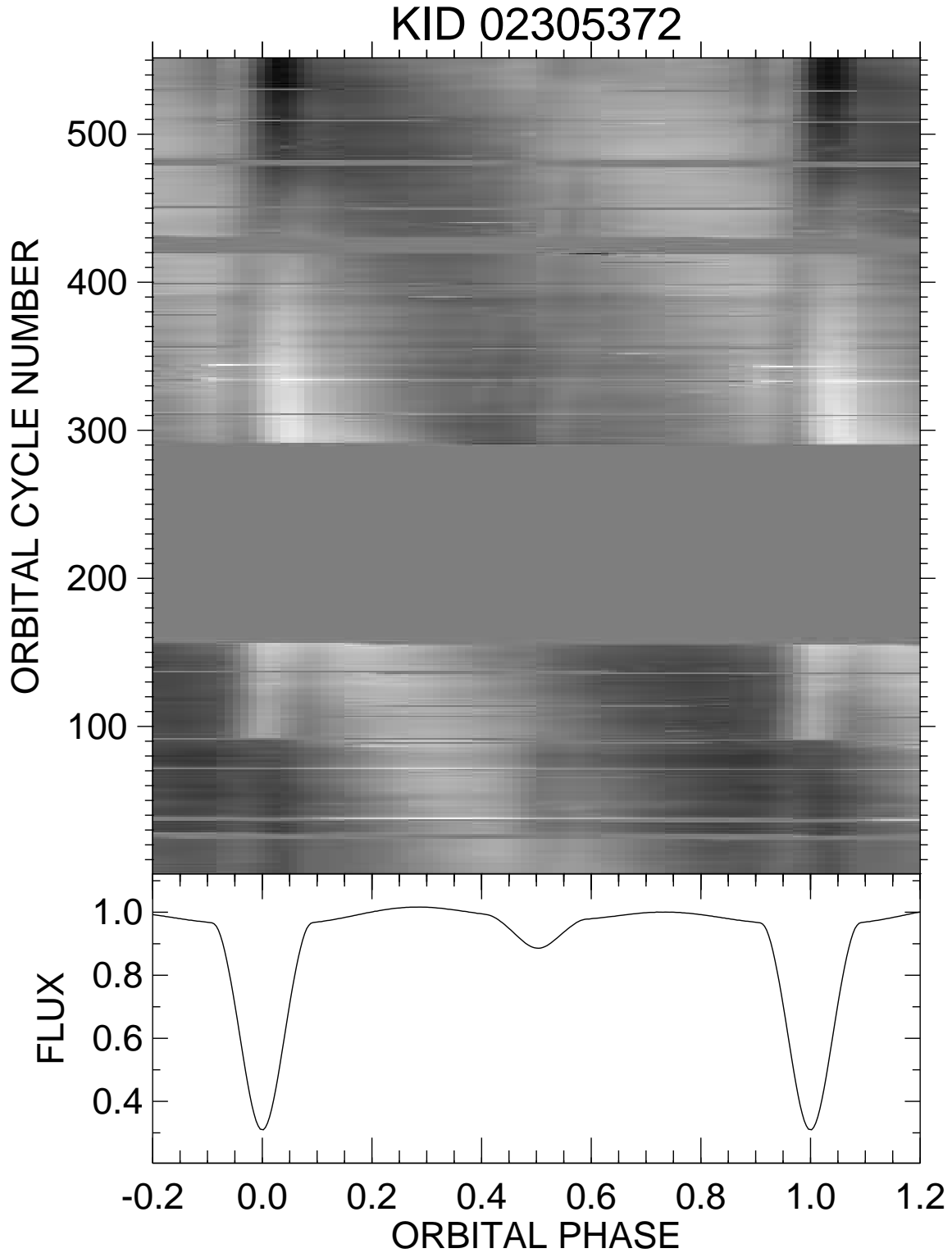


Fig. 1.1.— The lower panel shows a mean, normalized light curve formed by binning in orbital phase. The top panel shows the flux differences as a function of orbital phase and cycle number, represented as a gray scale diagram (range  $\pm 3\%$ ).

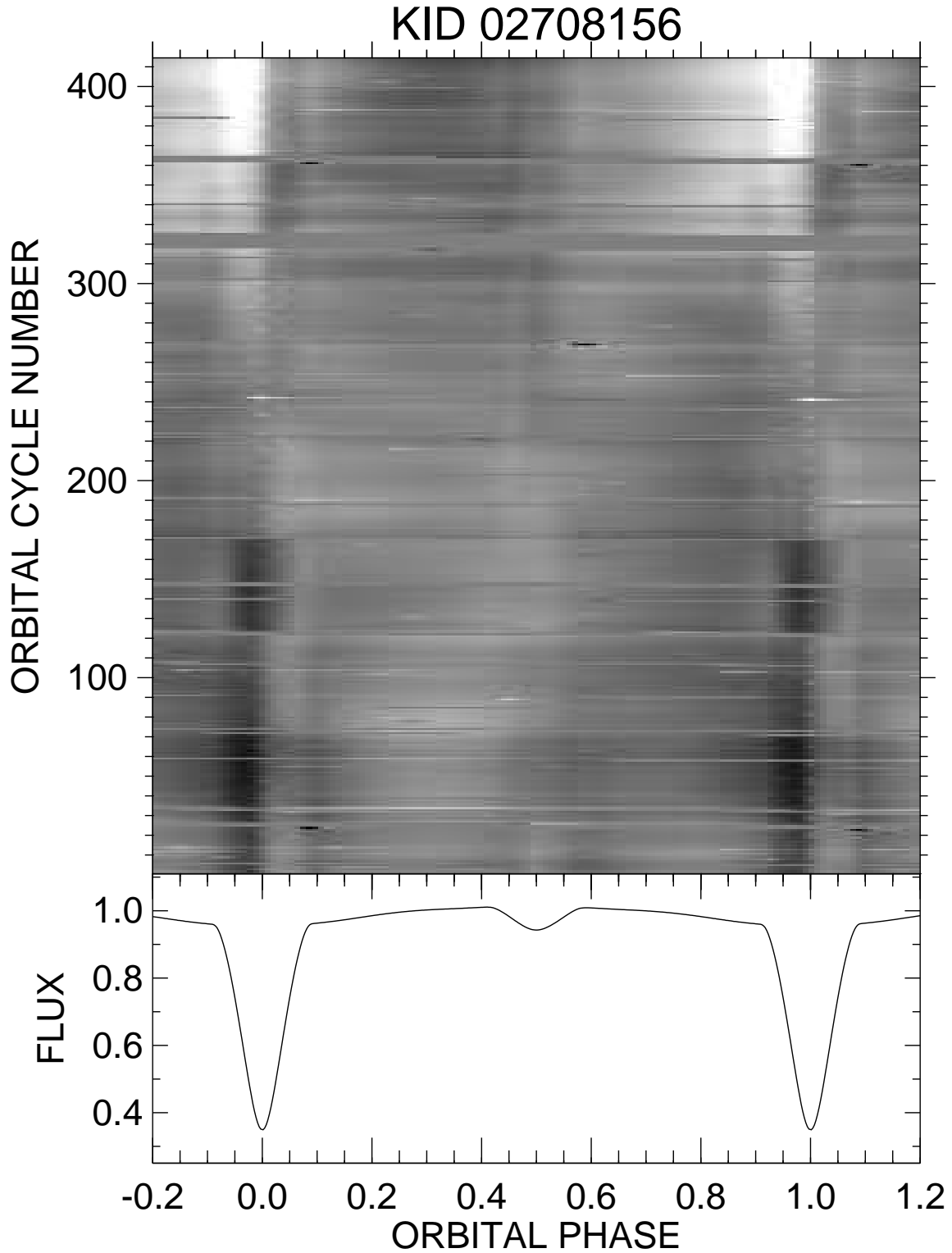


Fig. 1.2.— The lower panel shows a mean, normalized light curve formed by binning in orbital phase. The top panel shows the flux differences as a function of orbital phase and cycle number, represented as a gray scale diagram (range  $\pm 1\%$ ).

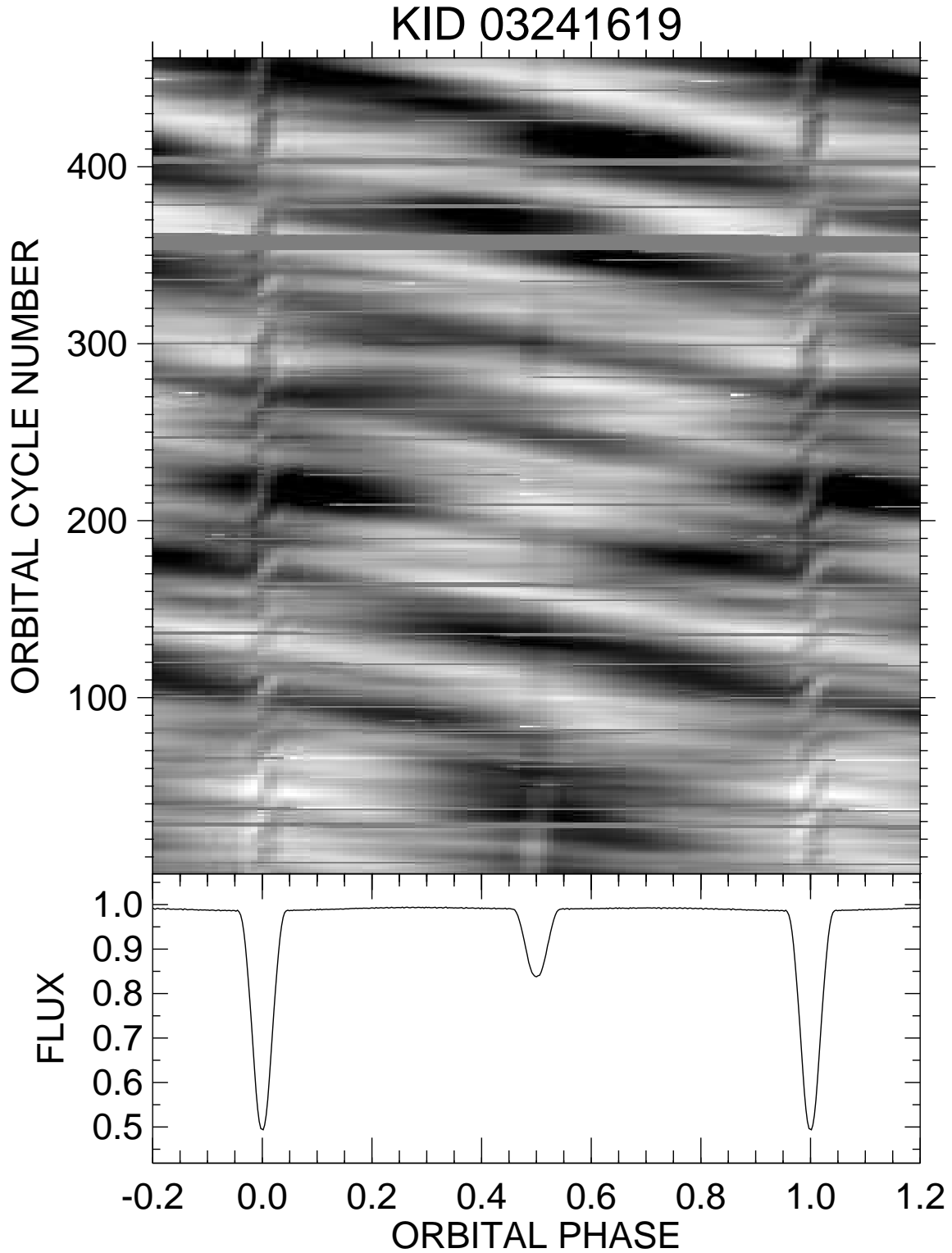


Fig. 1.3.— The lower panel shows a mean, normalized light curve formed by binning in orbital phase. The top panel shows the flux differences as a function of orbital phase and cycle number, represented as a gray scale diagram (range  $\pm 3\%$ ).



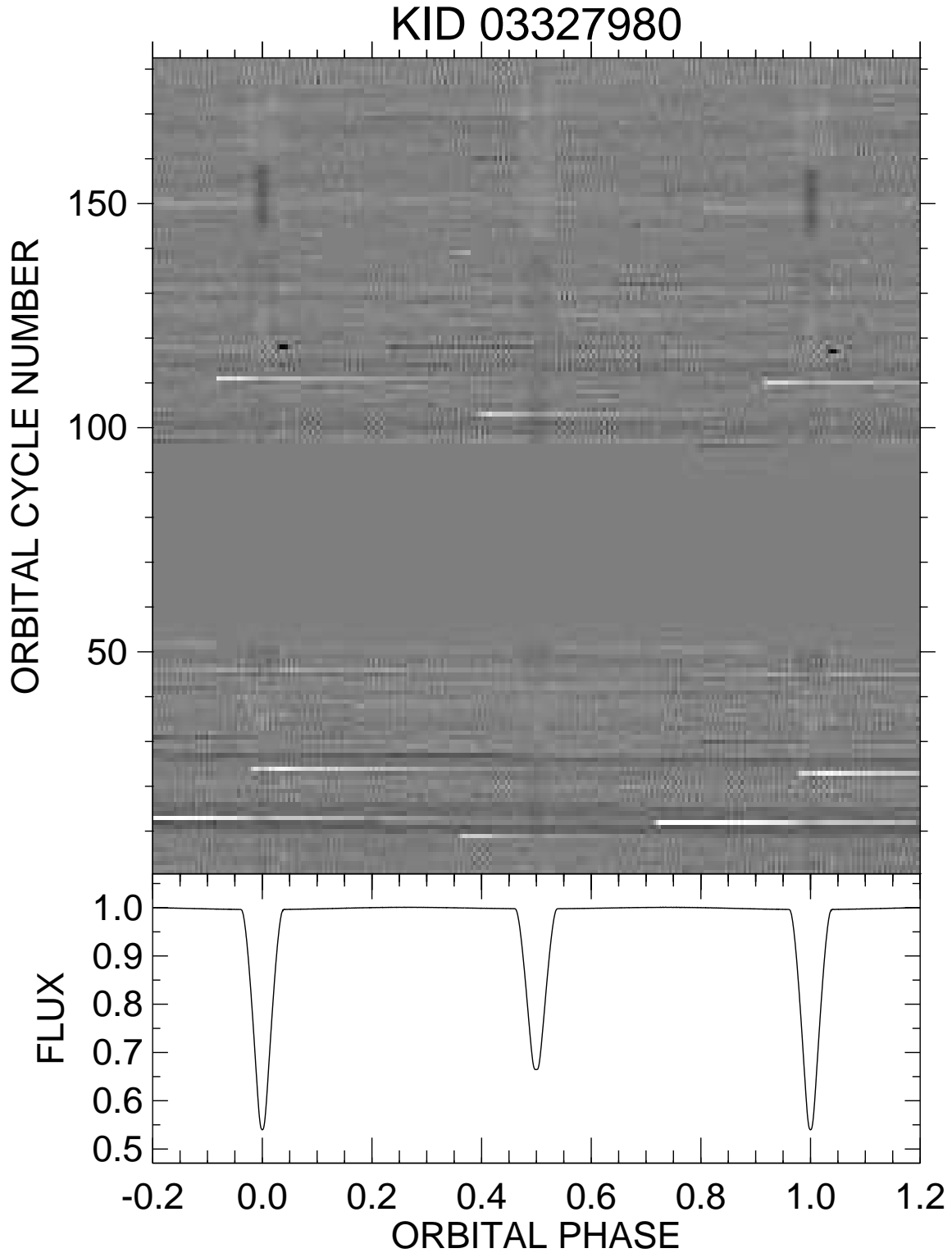


Fig. 1.4.— The lower panel shows a mean, normalized light curve formed by binning in orbital phase. The top panel shows the flux differences as a function of orbital phase and cycle number, represented as a gray scale diagram (range  $\pm 0.5\%$ ).

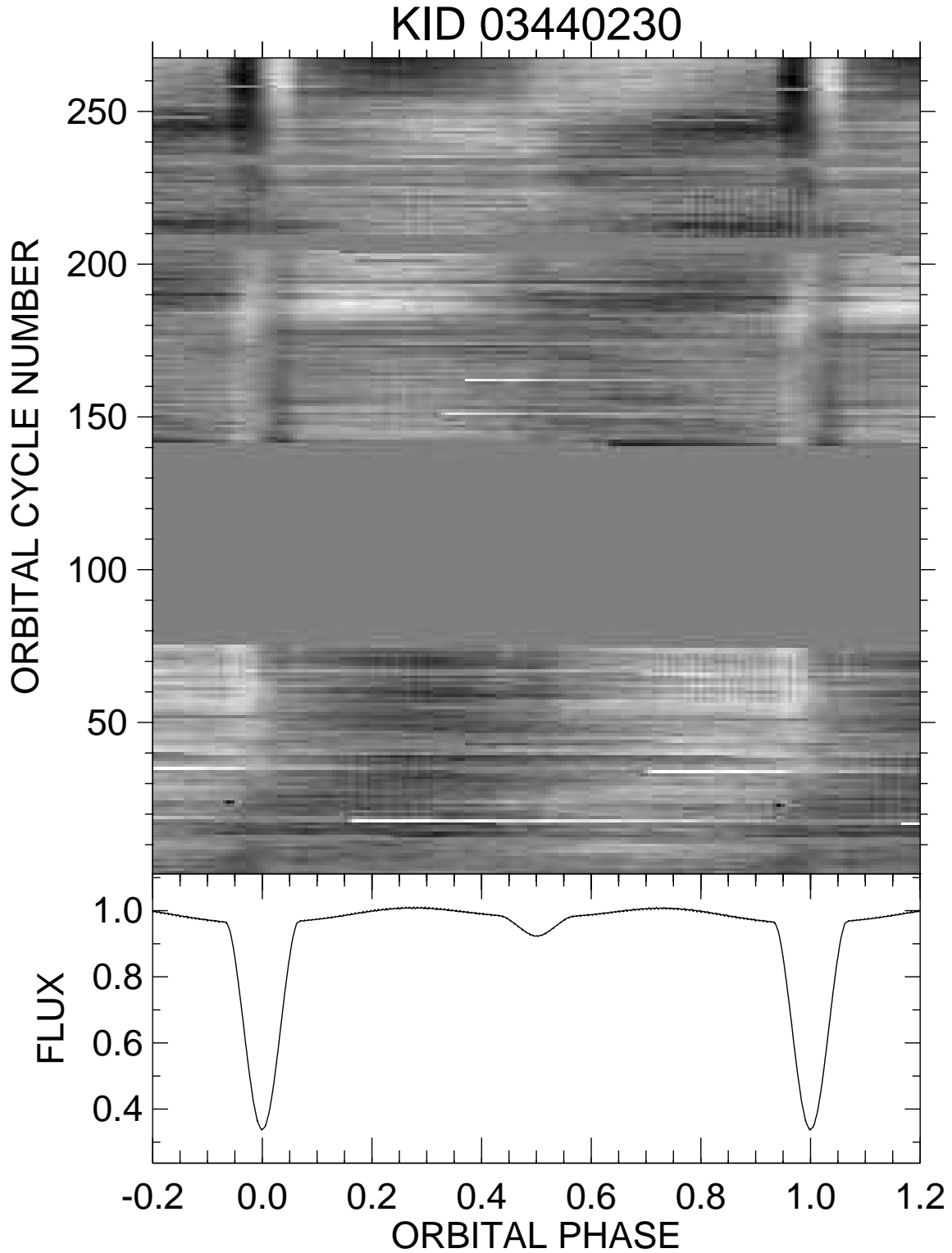


Fig. 1.5.— The lower panel shows a mean, normalized light curve formed by binning in orbital phase. The top panel shows the flux differences as a function of orbital phase and cycle number, represented as a gray scale diagram (range  $\pm 1\%$ ).

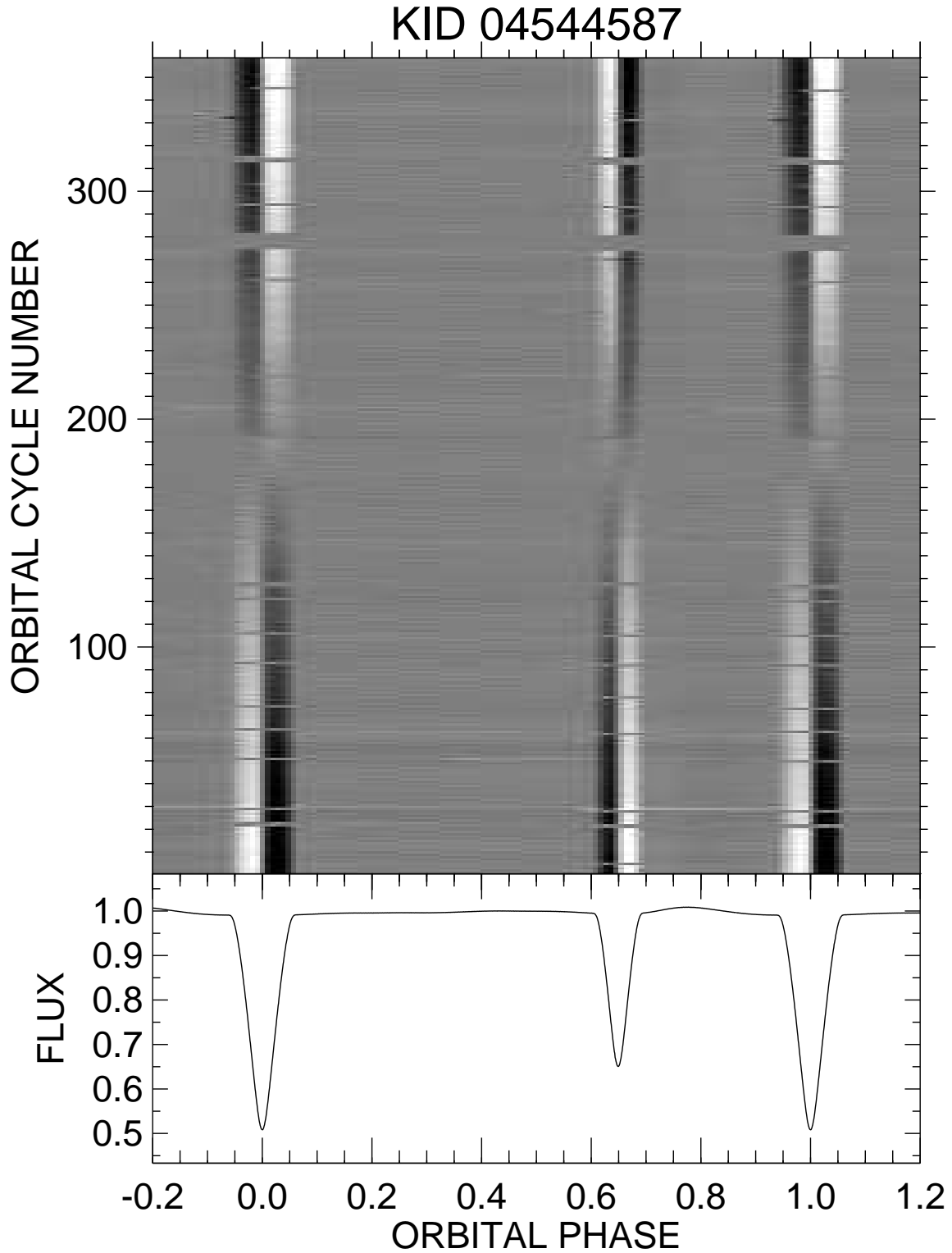


Fig. 1.6.— The lower panel shows a mean, normalized light curve formed by binning in orbital phase. The top panel shows the flux differences as a function of orbital phase and cycle number, represented as a gray scale diagram (range  $\pm 1.5\%$ ).

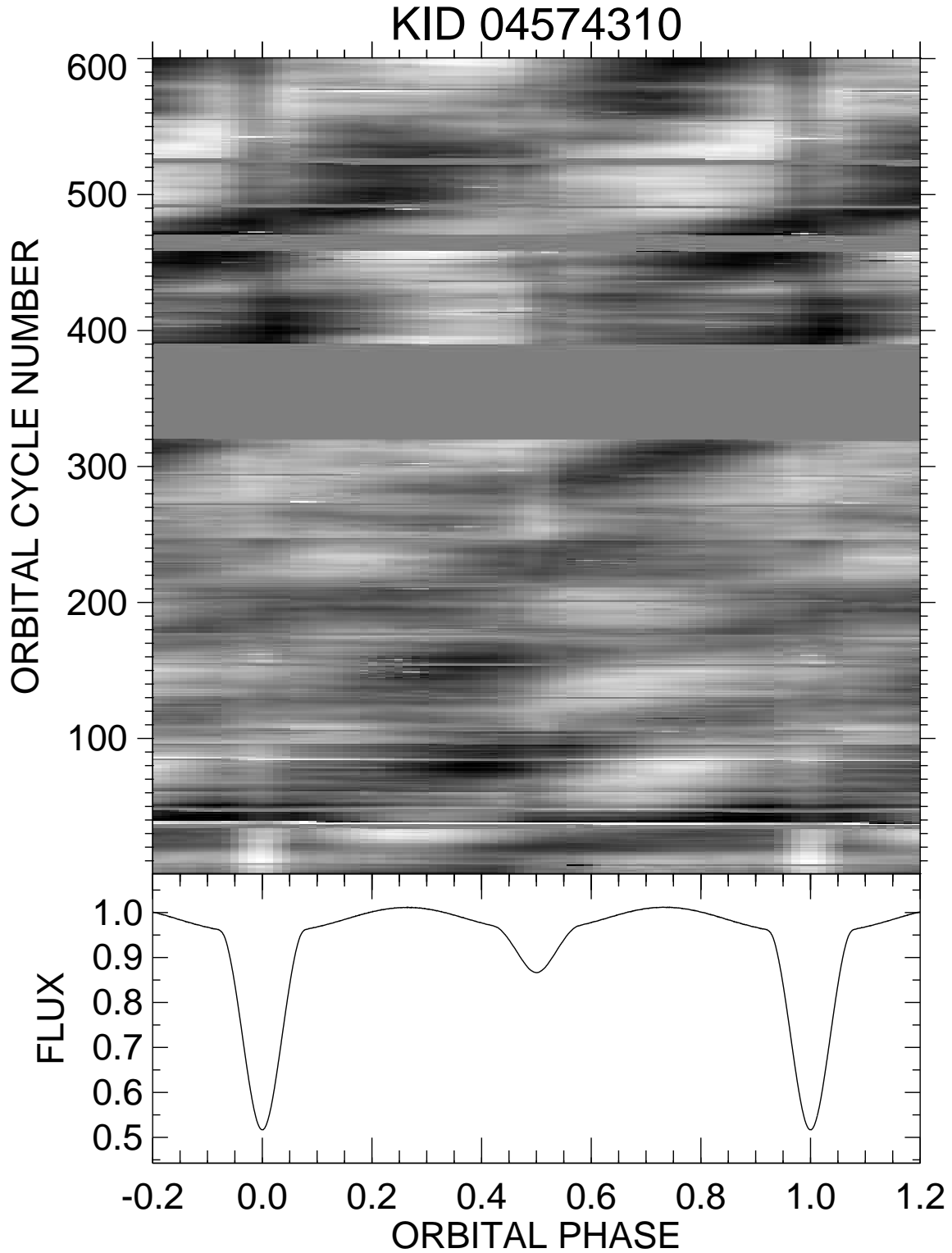


Fig. 1.7.— The lower panel shows a mean, normalized light curve formed by binning in orbital phase. The top panel shows the flux differences as a function of orbital phase and cycle number, represented as a gray scale diagram (range  $\pm 0.5\%$ ).

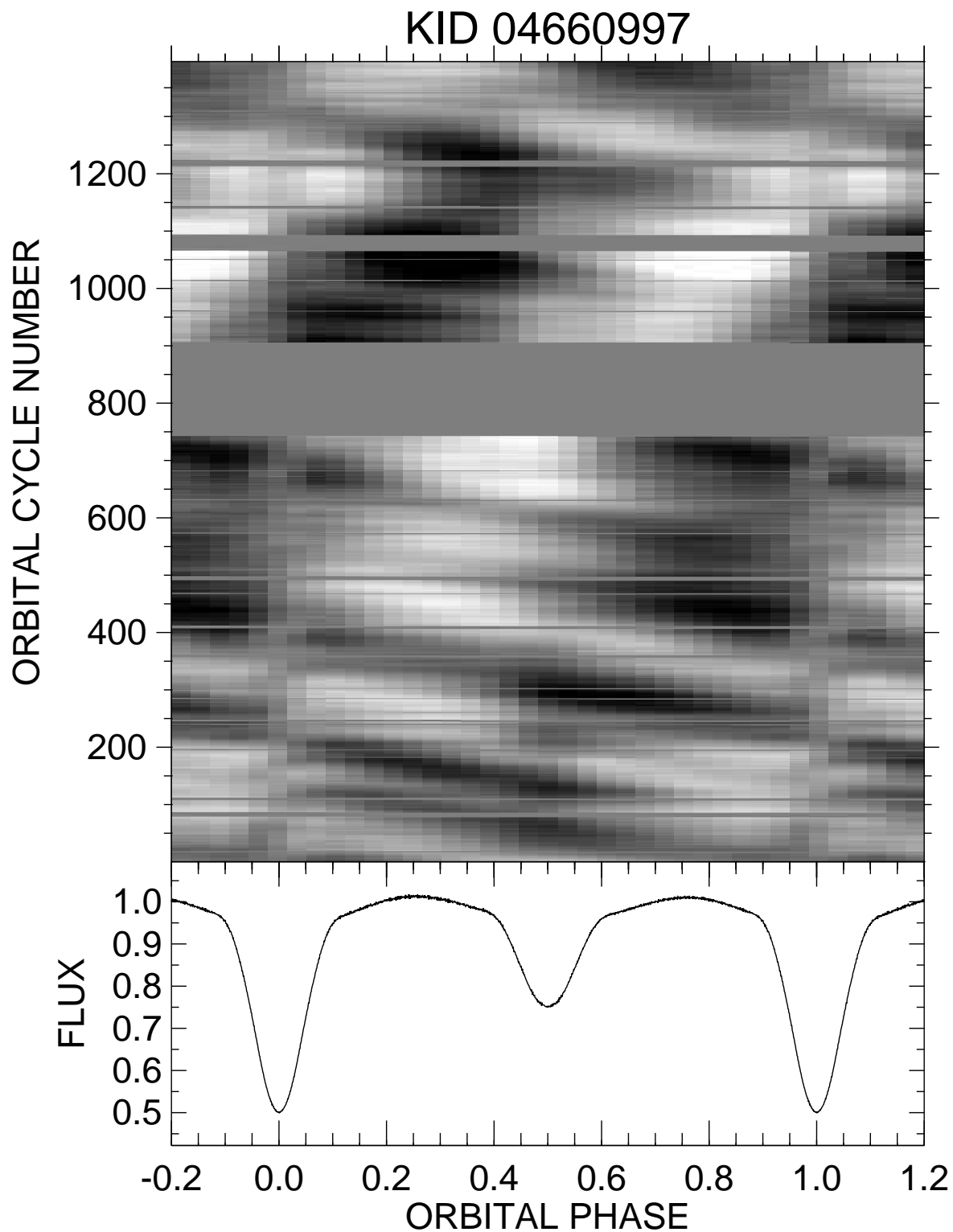


Fig. 1.8.— The lower panel shows a mean, normalized light curve formed by binning in orbital phase. The top panel shows the flux differences as a function of orbital phase and cycle number, represented as a gray scale diagram (range  $\pm 4\%$ ).

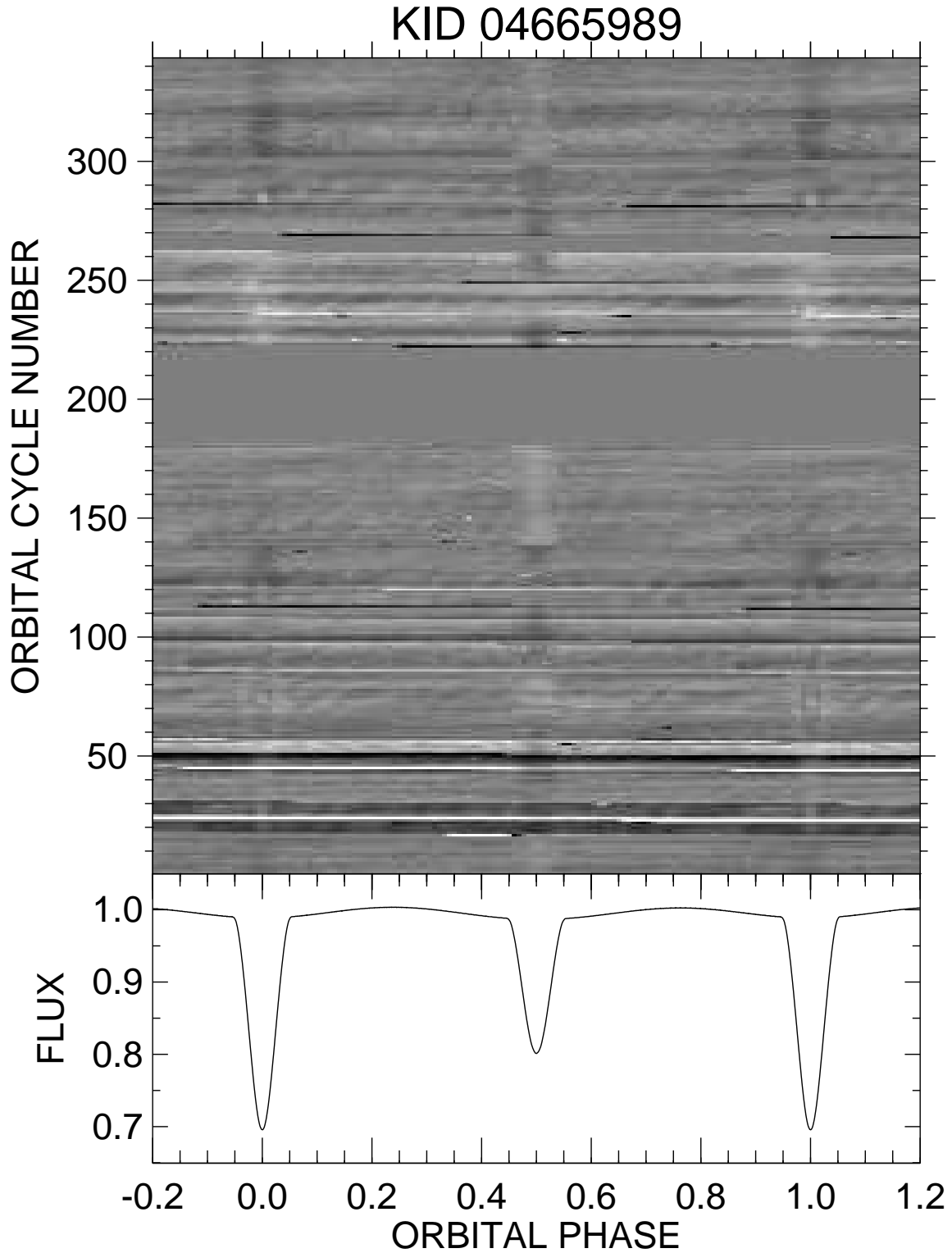


Fig. 1.9.— The lower panel shows a mean, normalized light curve formed by binning in orbital phase. The top panel shows the flux differences as a function of orbital phase and cycle number, represented as a gray scale diagram (range  $\pm 0.2\%$ ).

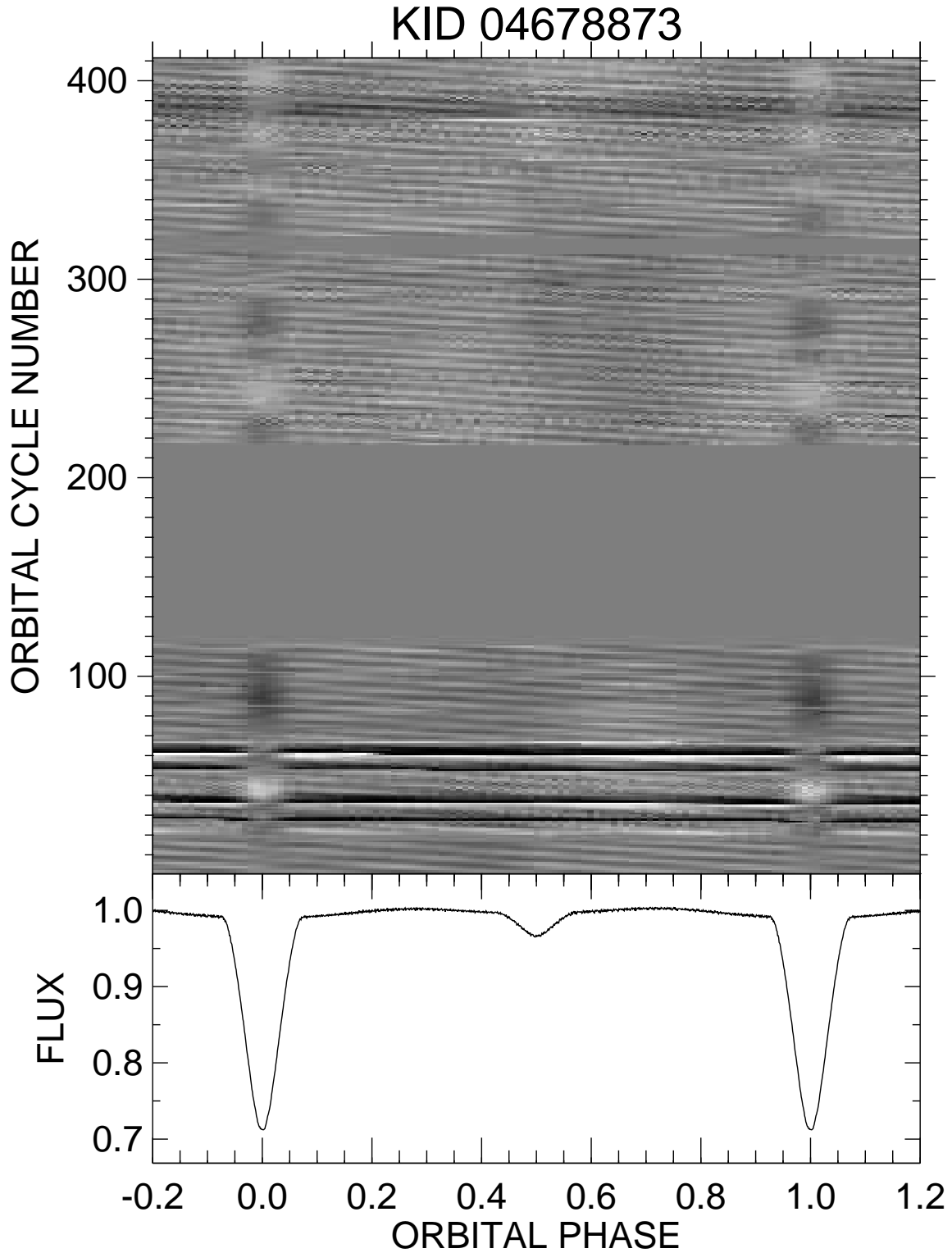


Fig. 1.10.— The lower panel shows a mean, normalized light curve formed by binning in orbital phase. The top panel shows the flux differences as a function of orbital phase and cycle number, represented as a gray scale diagram (range  $\pm 2\%$ ).

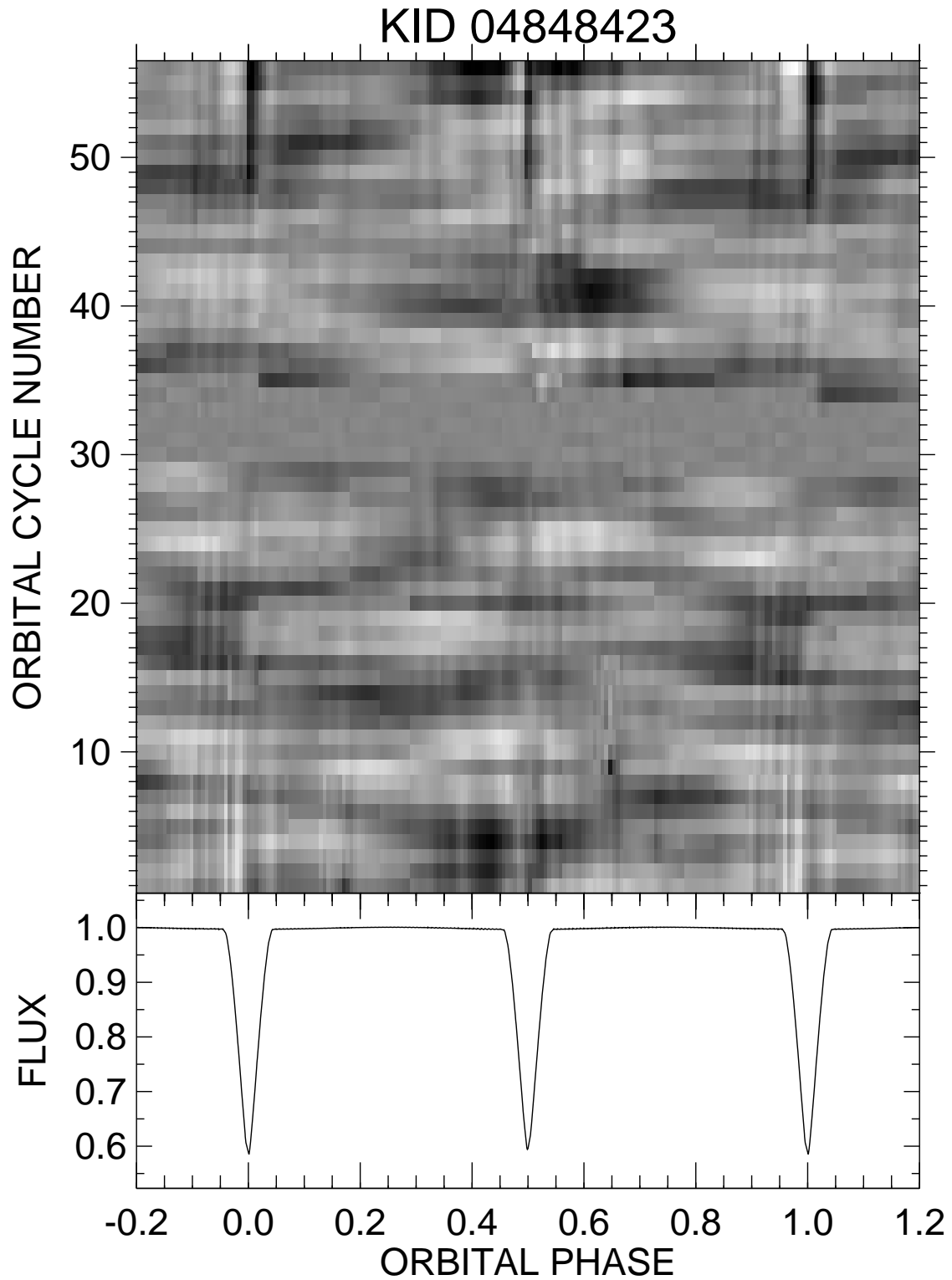


Fig. 1.11.— The lower panel shows a mean, normalized light curve formed by binning in orbital phase. The top panel shows the flux differences as a function of orbital phase and cycle number, represented as a gray scale diagram (range  $\pm 0.2\%$ ).



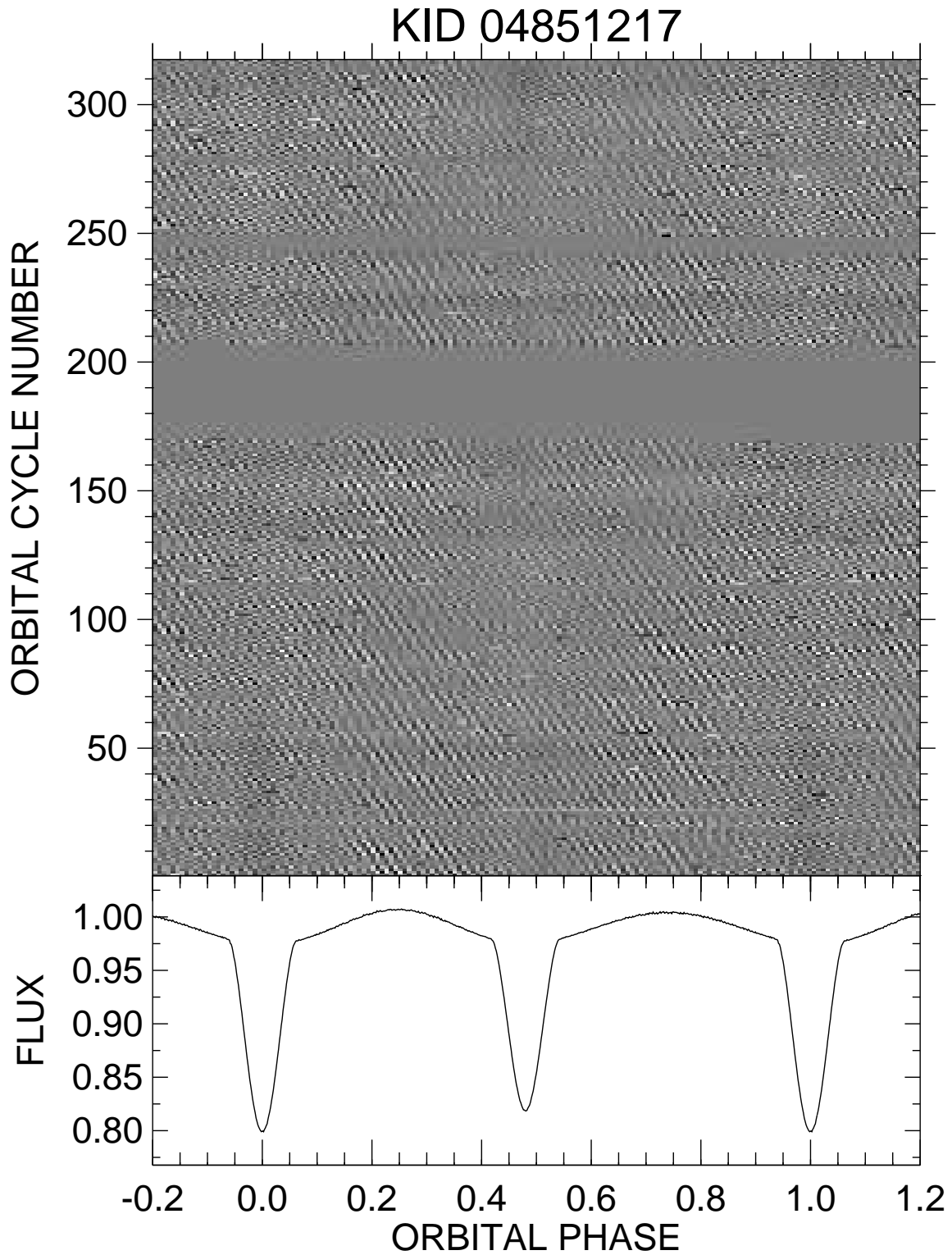


Fig. 1.12.— The lower panel shows a mean, normalized light curve formed by binning in orbital phase. The top panel shows the flux differences as a function of orbital phase and cycle number, represented as a gray scale diagram (range  $\pm 1\%$ ).

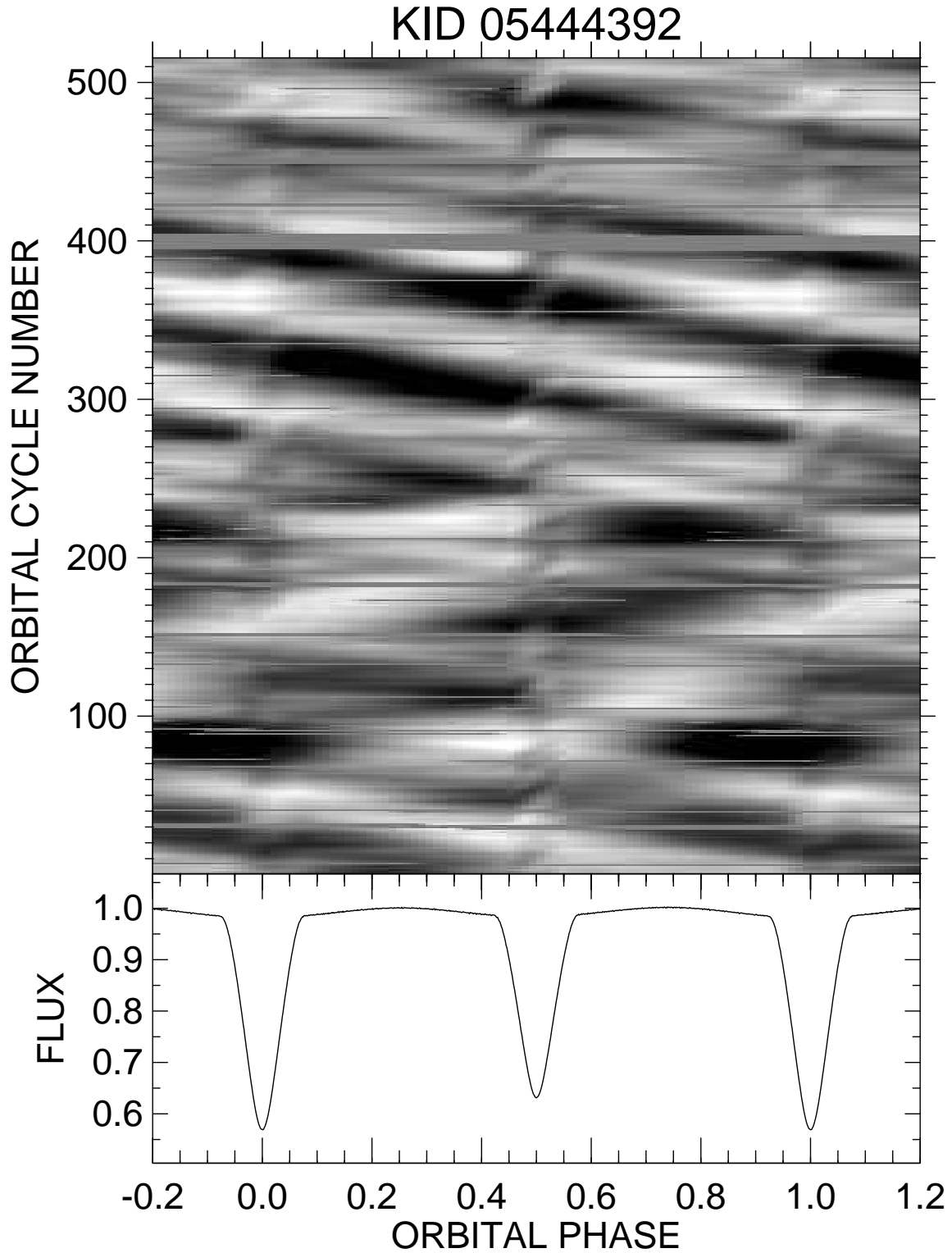


Fig. 1.13.— The lower panel shows a mean, normalized light curve formed by binning in orbital phase. The top panel shows the flux differences as a function of orbital phase and cycle number, represented as a gray scale diagram (range  $\pm 2\%$ ).

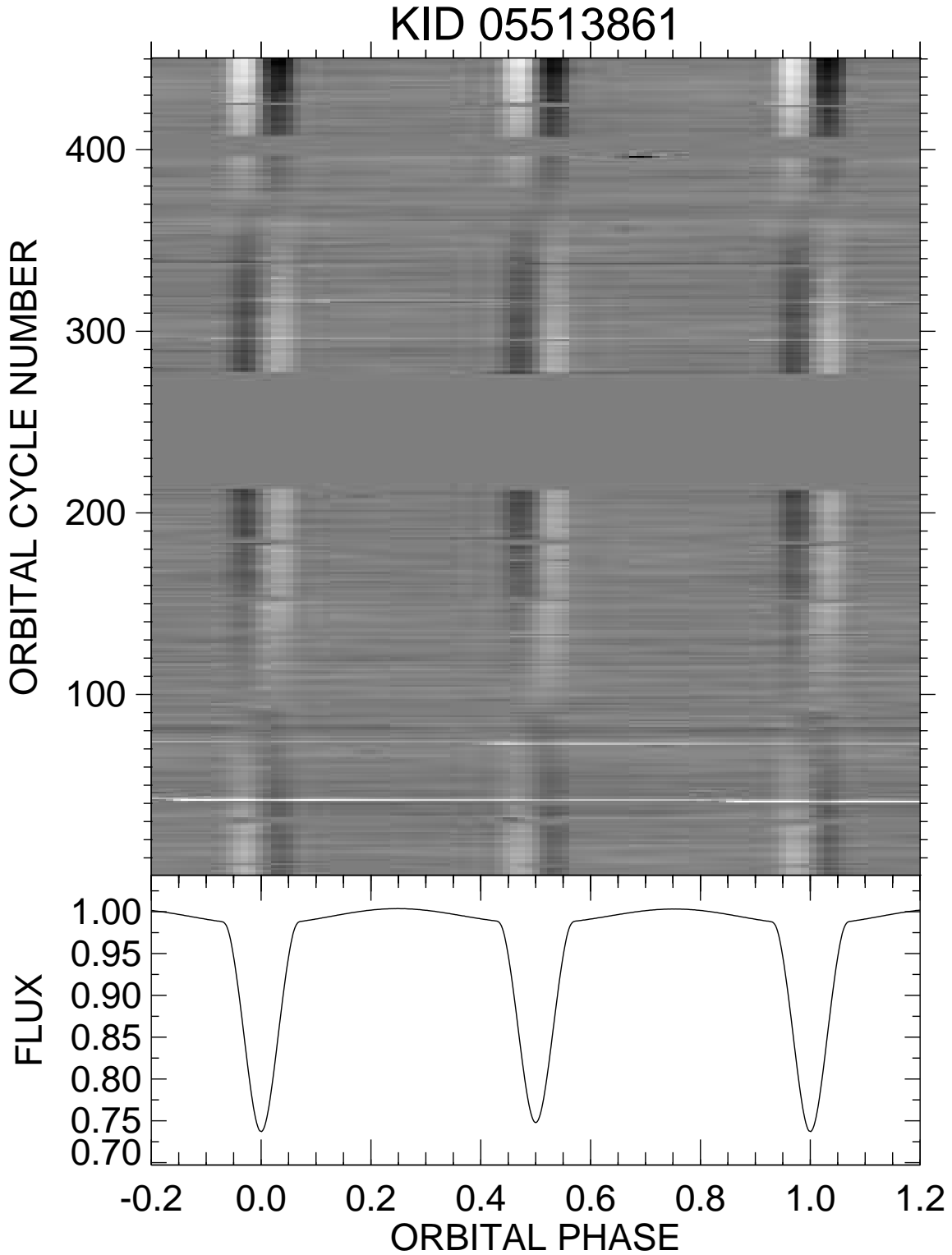


Fig. 1.14.— The lower panel shows a mean, normalized light curve formed by binning in orbital phase. The top panel shows the flux differences as a function of orbital phase and cycle number, represented as a gray scale diagram (range  $\pm 0.5\%$ ).

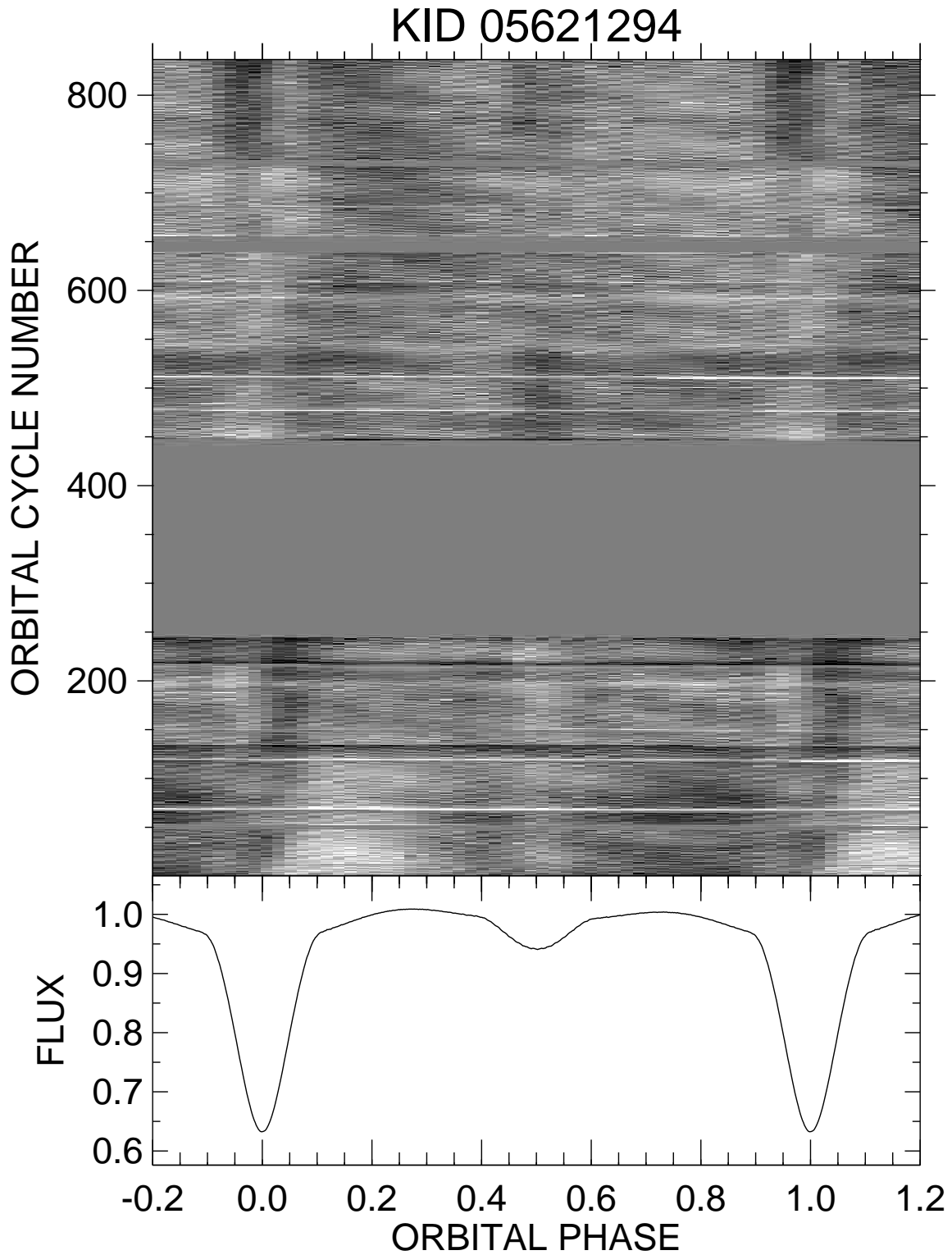


Fig. 1.15.— The lower panel shows a mean, normalized light curve formed by binning in orbital phase. The top panel shows the flux differences as a function of orbital phase and cycle number, represented as a gray scale diagram (range  $\pm 0.5\%$ ).

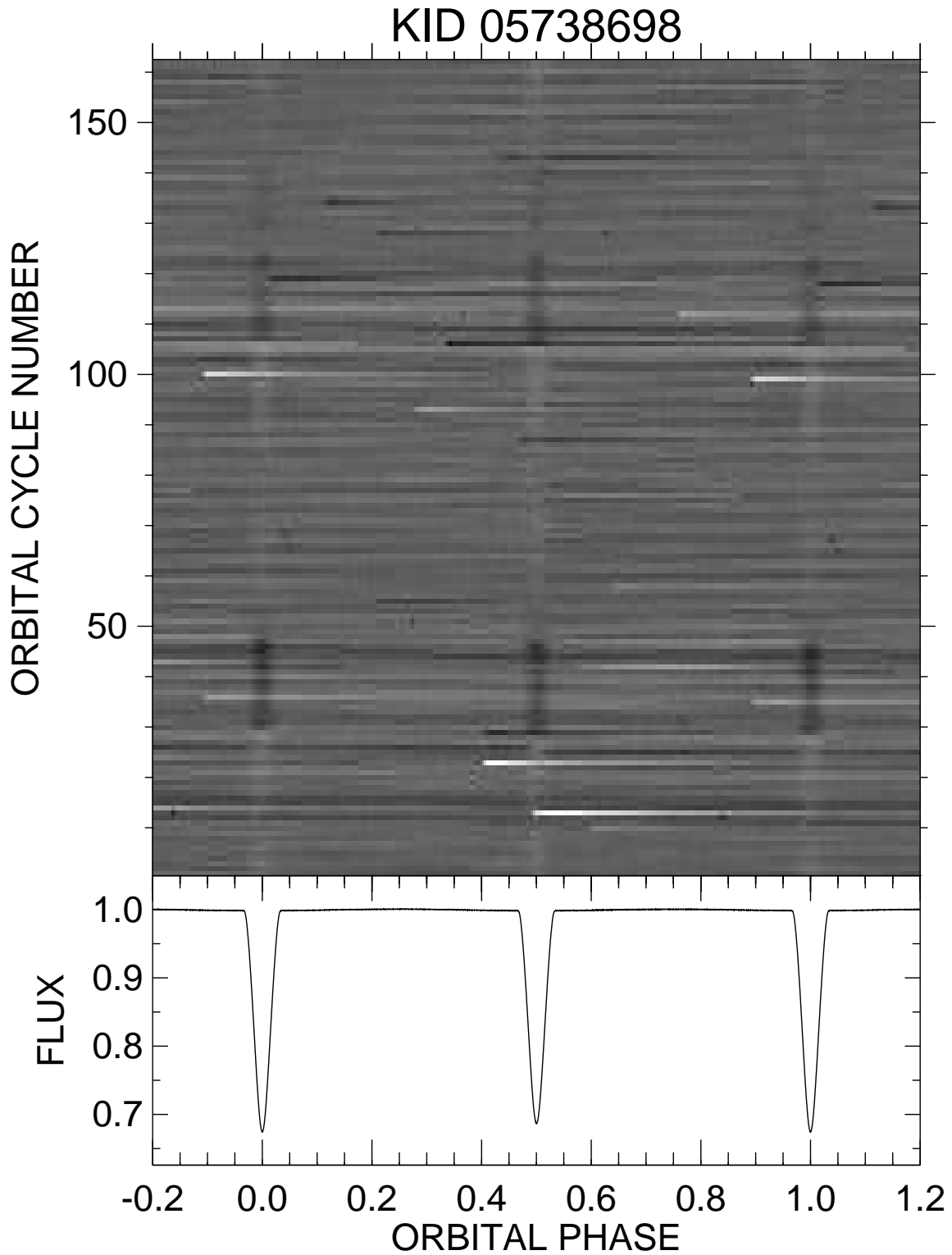


Fig. 1.16.— The lower panel shows a mean, normalized light curve formed by binning in orbital phase. The top panel shows the flux differences as a function of orbital phase and cycle number, represented as a gray scale diagram (range  $\pm 0.5\%$ ).

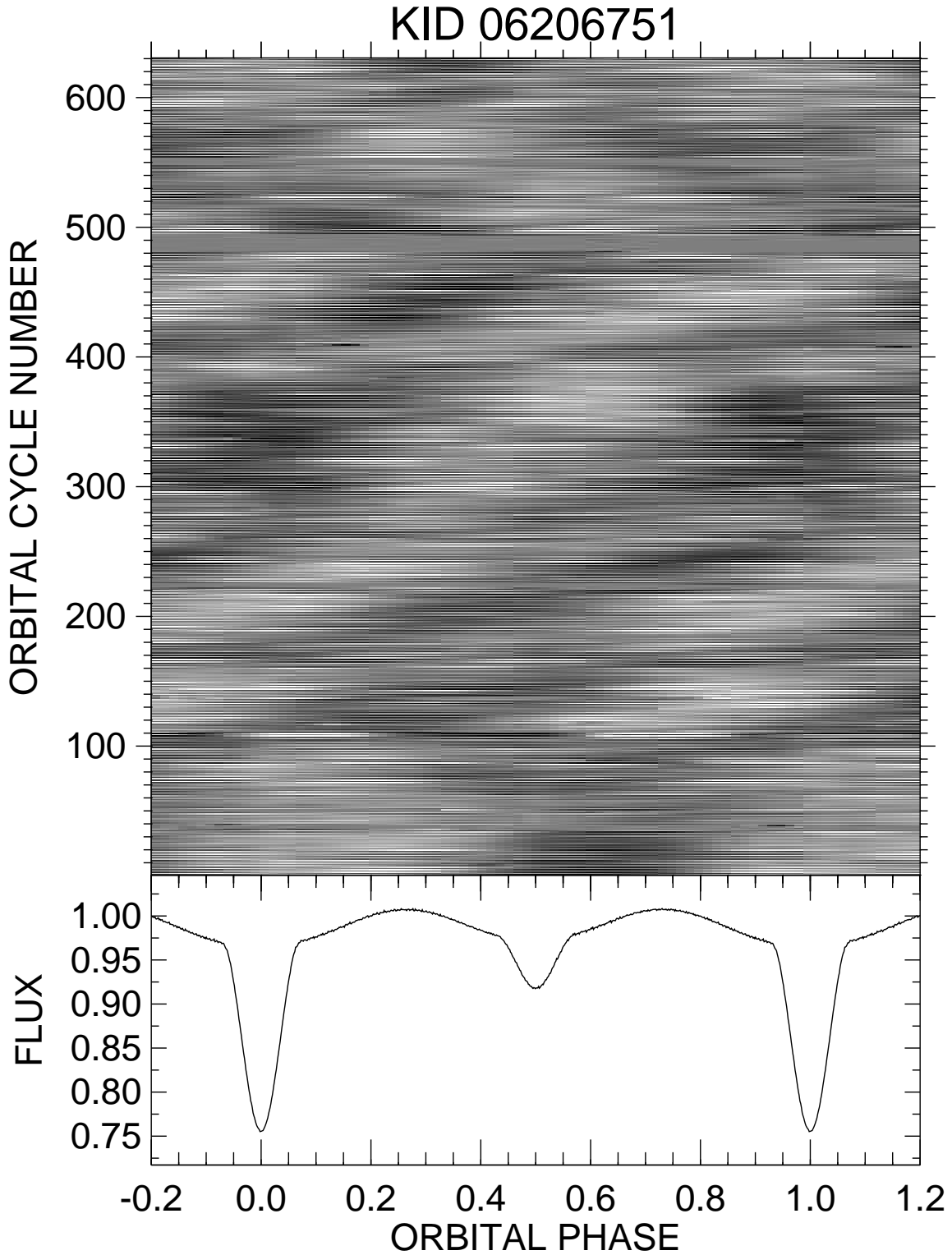


Fig. 1.17.— The lower panel shows a mean, normalized light curve formed by binning in orbital phase. The top panel shows the flux differences as a function of orbital phase and cycle number, represented as a gray scale diagram (range  $\pm 1.5\%$ ).

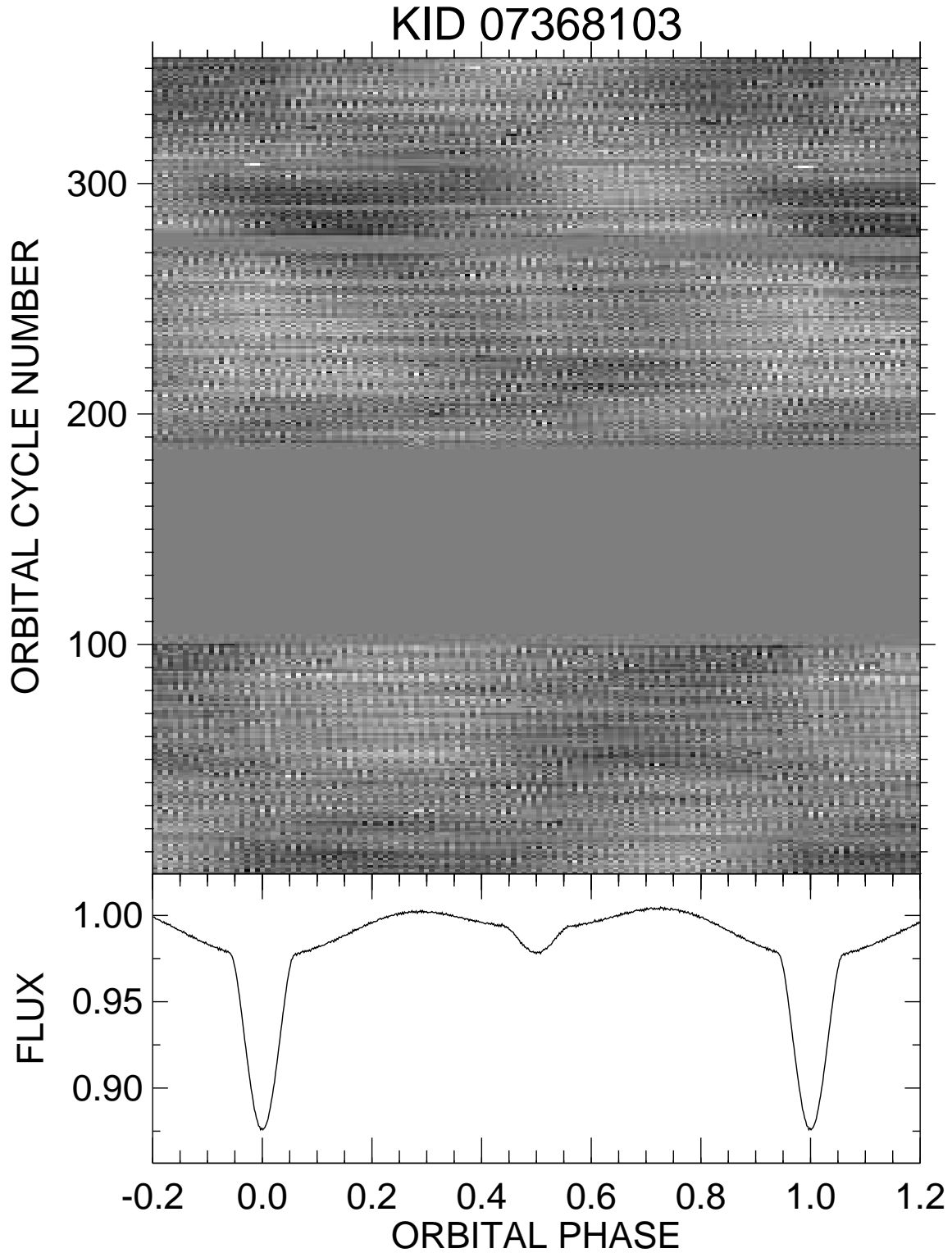


Fig. 1.18.— The lower panel shows a mean, normalized light curve formed by binning in orbital phase. The top panel shows the flux differences as a function of orbital phase and cycle number, represented as a gray scale diagram (range  $\pm 1\%$ ).

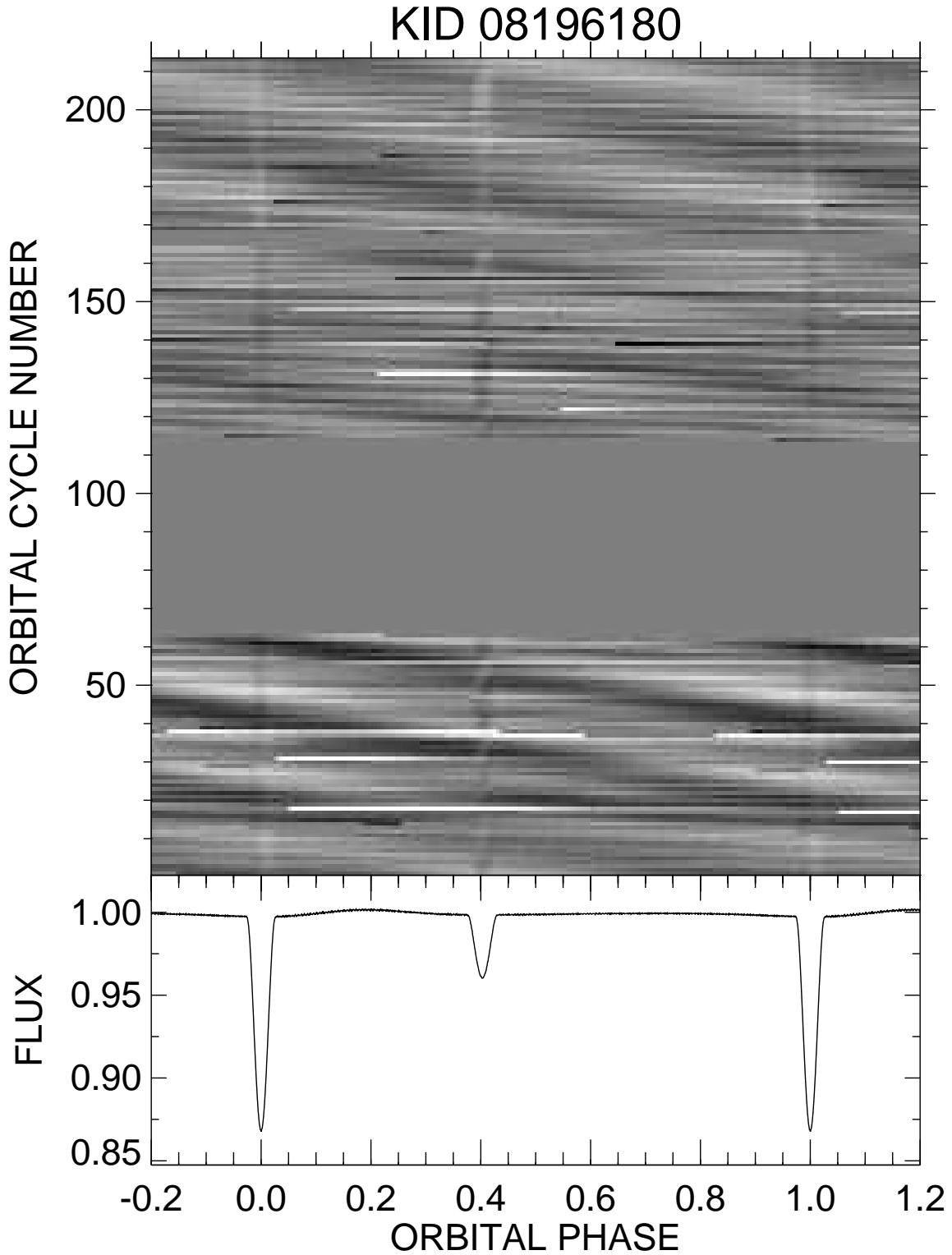


Fig. 1.19.— The lower panel shows a mean, normalized light curve formed by binning in orbital phase. The top panel shows the flux differences as a function of orbital phase and cycle number, represented as a gray scale diagram (range  $\pm 0.5\%$ ).



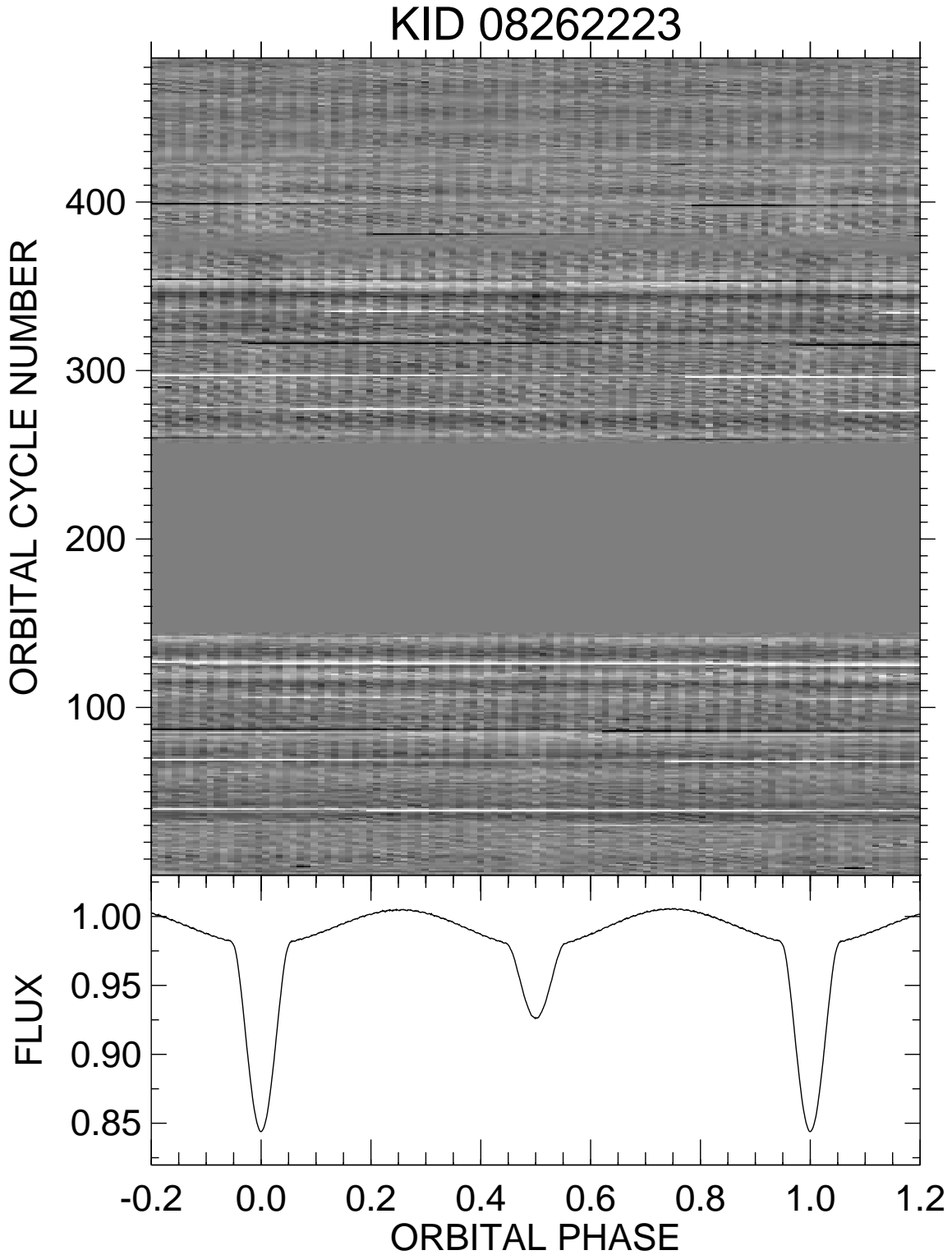


Fig. 1.20.— The lower panel shows a mean, normalized light curve formed by binning in orbital phase. The top panel shows the flux differences as a function of orbital phase and cycle number, represented as a gray scale diagram (range  $\pm 0.3\%$ ).

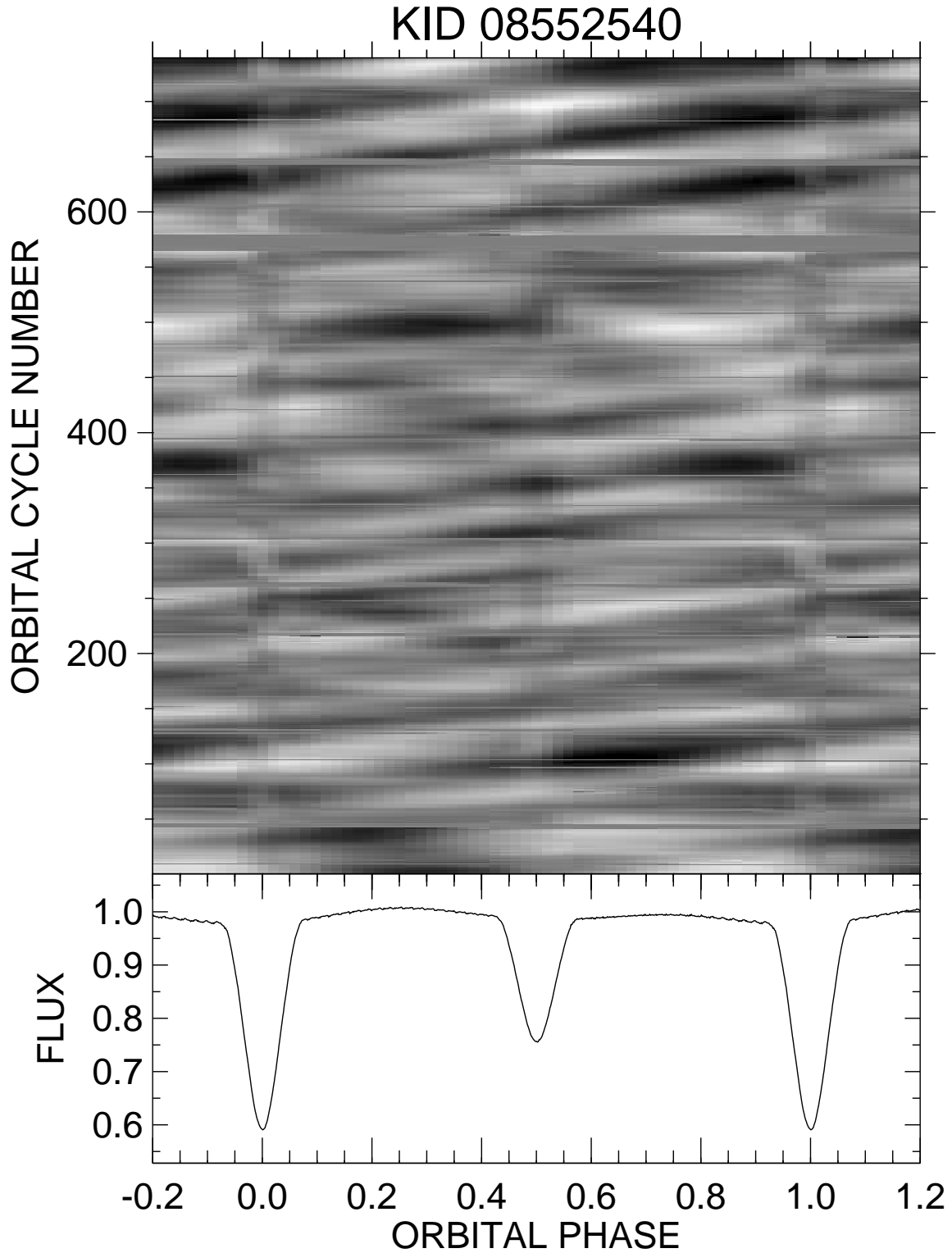


Fig. 1.21.— The lower panel shows a mean, normalized light curve formed by binning in orbital phase. The top panel shows the flux differences as a function of orbital phase and cycle number, represented as a gray scale diagram (range  $\pm 3\%$ ).

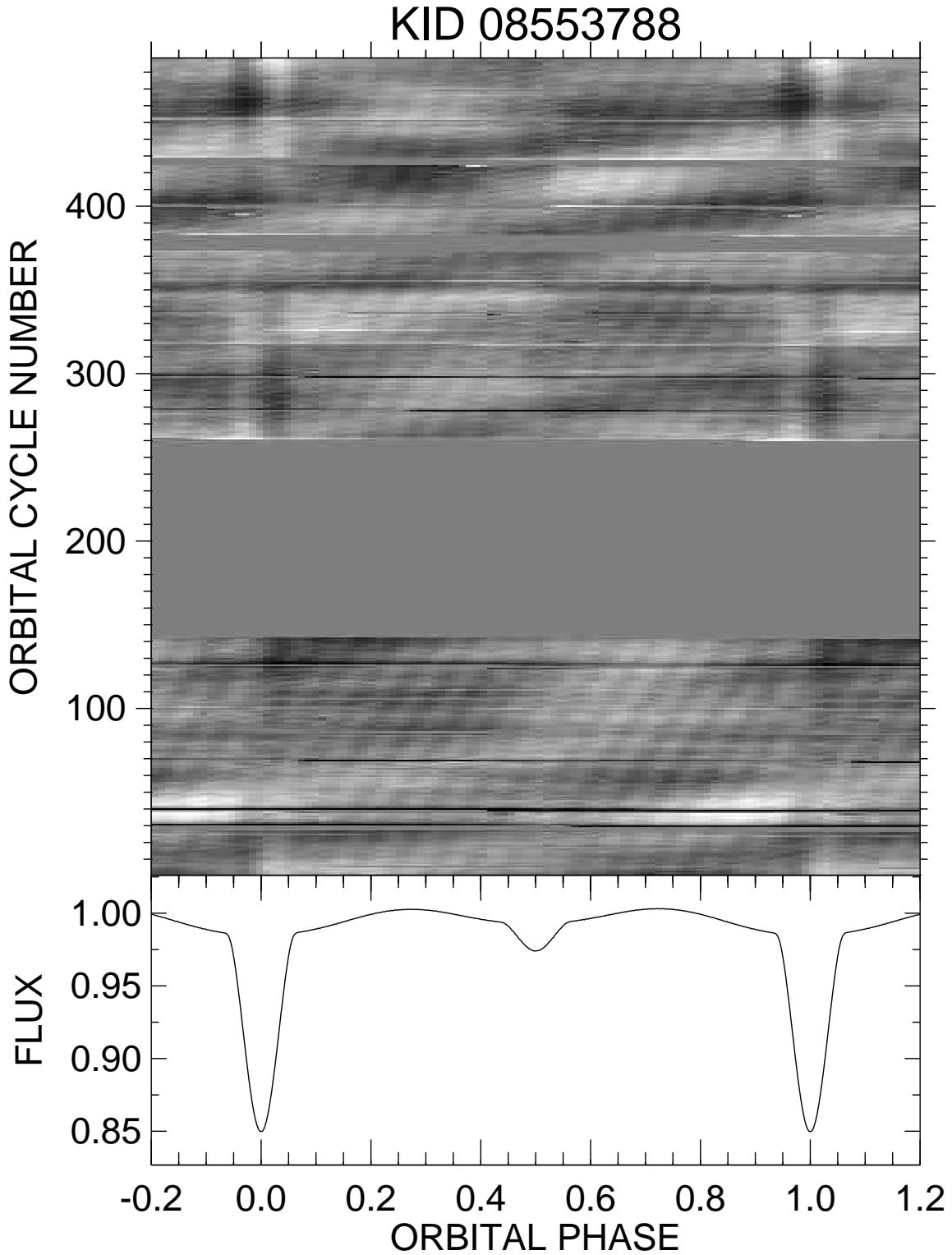


Fig. 1.22.— The lower panel shows a mean, normalized light curve formed by binning in orbital phase. The top panel shows the flux differences as a function of orbital phase and cycle number, represented as a gray scale diagram (range  $\pm 0.3\%$ ).

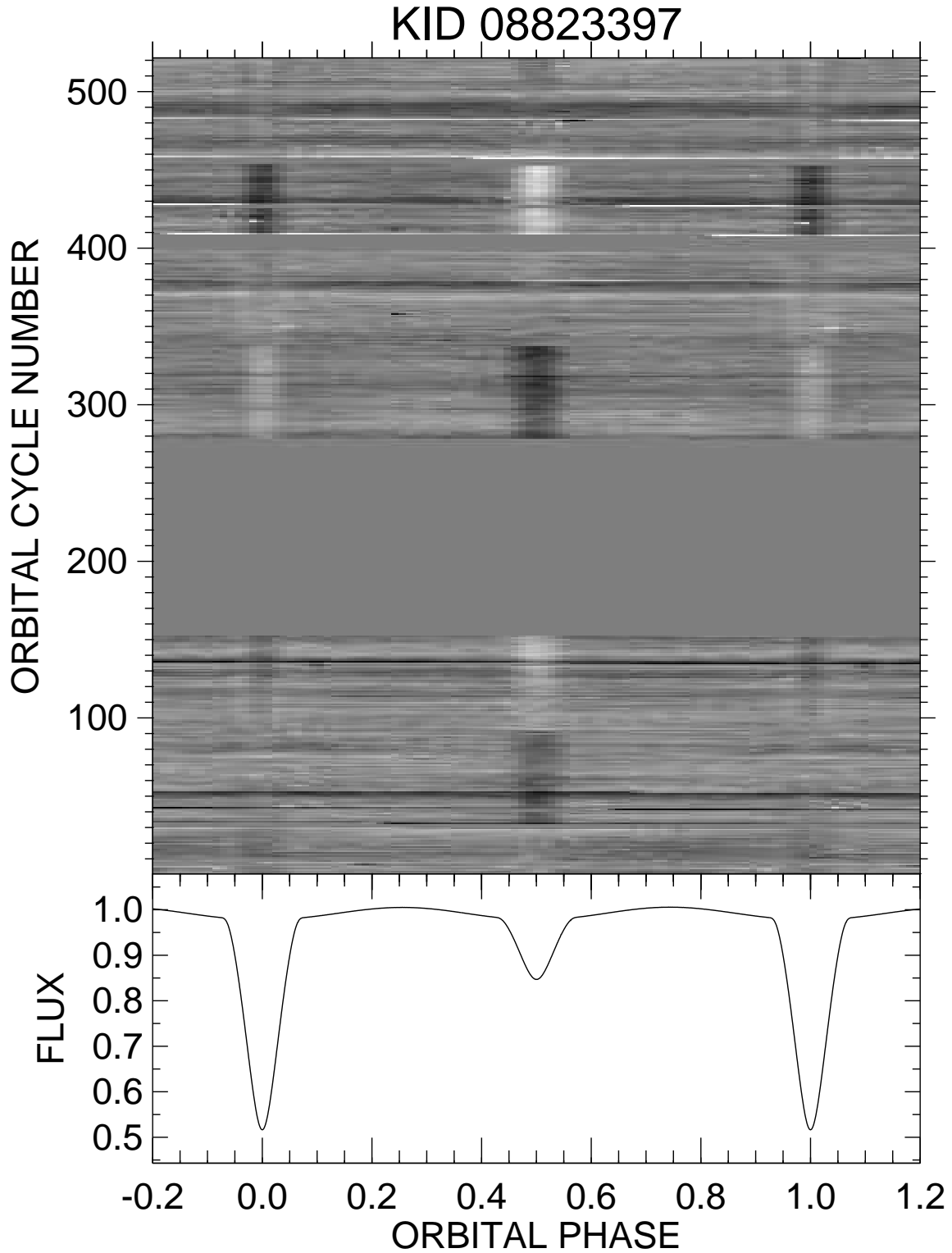


Fig. 1.23.— The lower panel shows a mean, normalized light curve formed by binning in orbital phase. The top panel shows the flux differences as a function of orbital phase and cycle number, represented as a gray scale diagram (range  $\pm 0.2\%$ ).

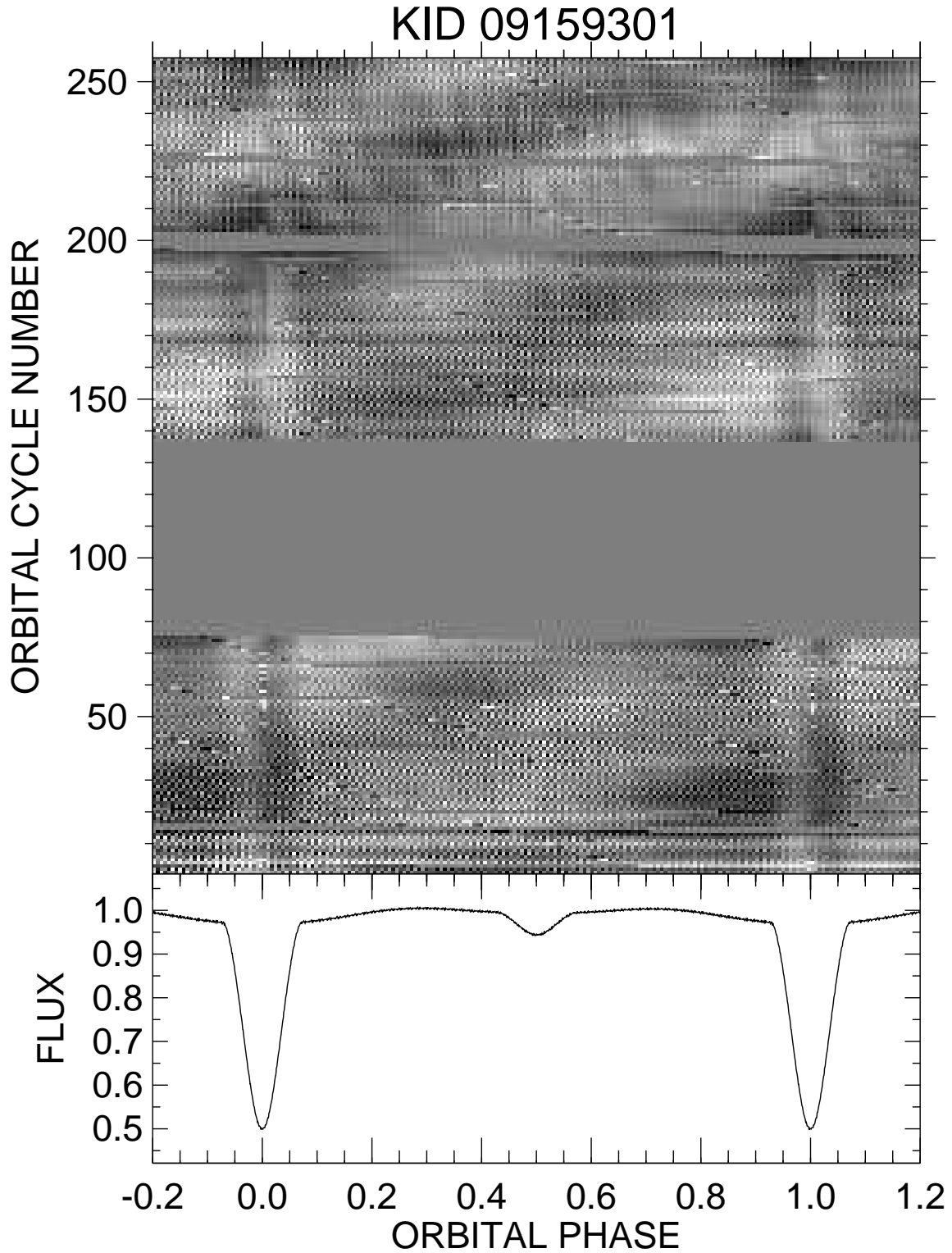


Fig. 1.24.— The lower panel shows a mean, normalized light curve formed by binning in orbital phase. The top panel shows the flux differences as a function of orbital phase and cycle number, represented as a gray scale diagram (range  $\pm 0.4\%$ ).

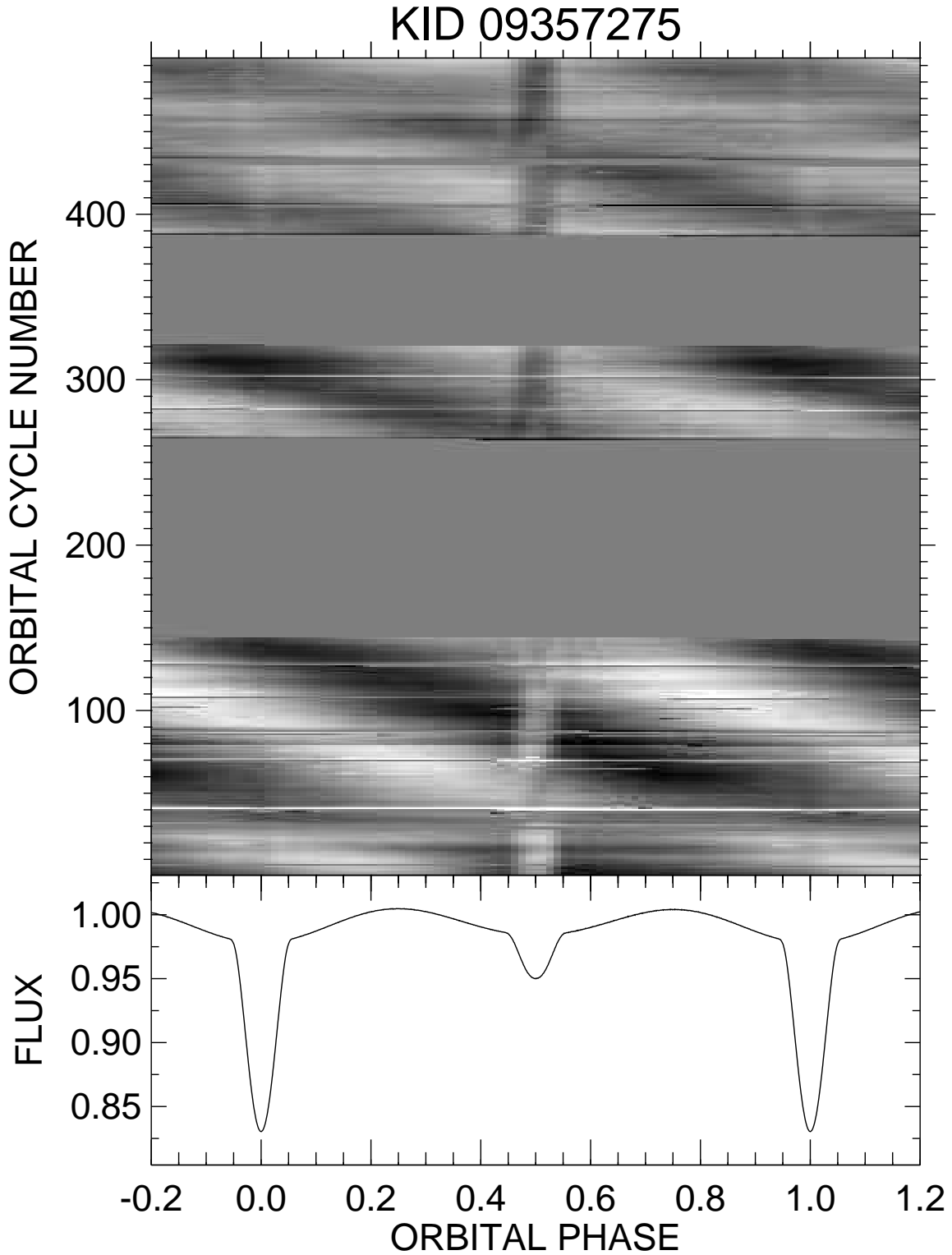


Fig. 1.25.— The lower panel shows a mean, normalized light curve formed by binning in orbital phase. The top panel shows the flux differences as a function of orbital phase and cycle number, represented as a gray scale diagram (range  $\pm 0.2\%$ ).

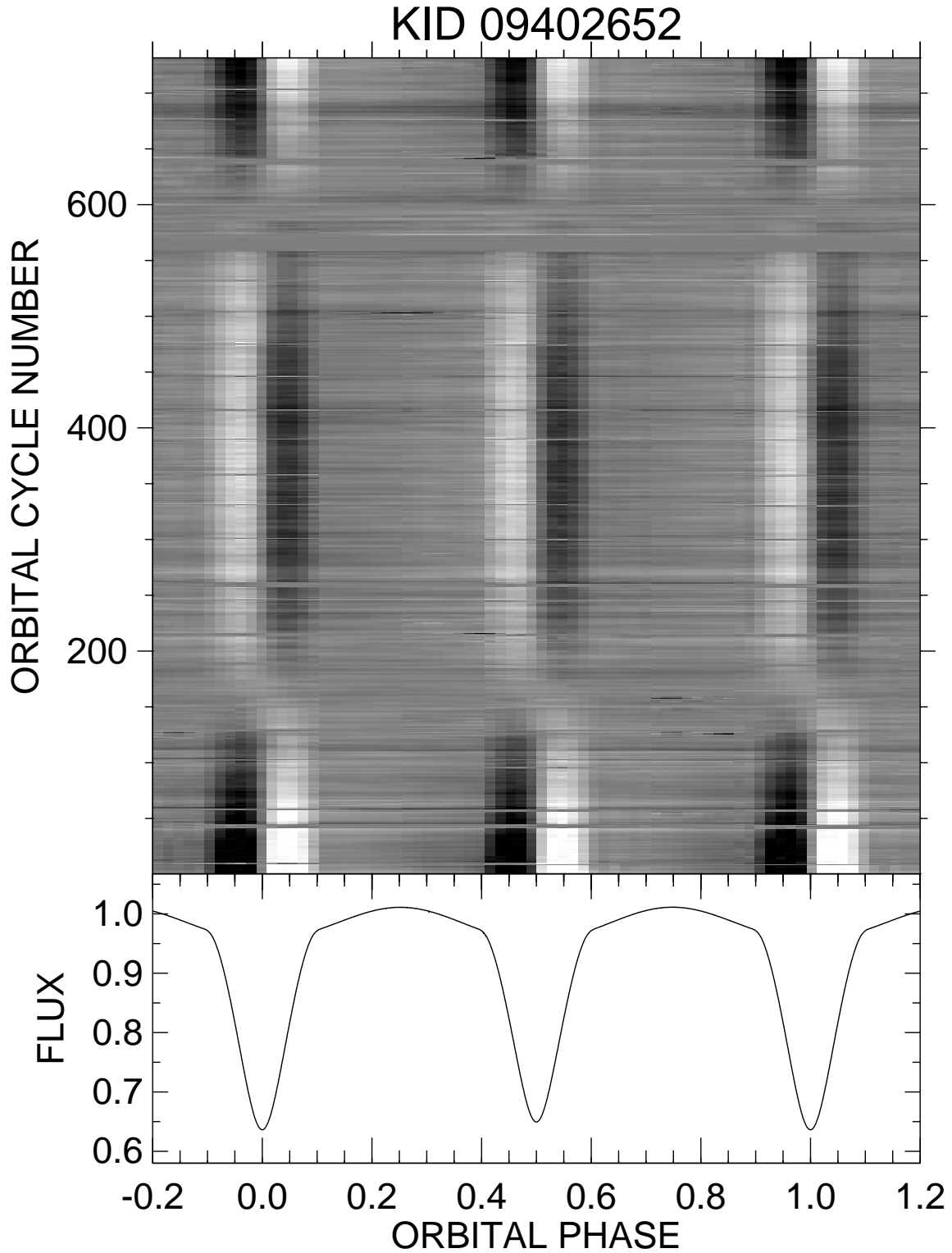


Fig. 1.26.— The lower panel shows a mean, normalized light curve formed by binning in orbital phase. The top panel shows the flux differences as a function of orbital phase and cycle number, represented as a gray scale diagram (range  $\pm 0.5\%$ ).

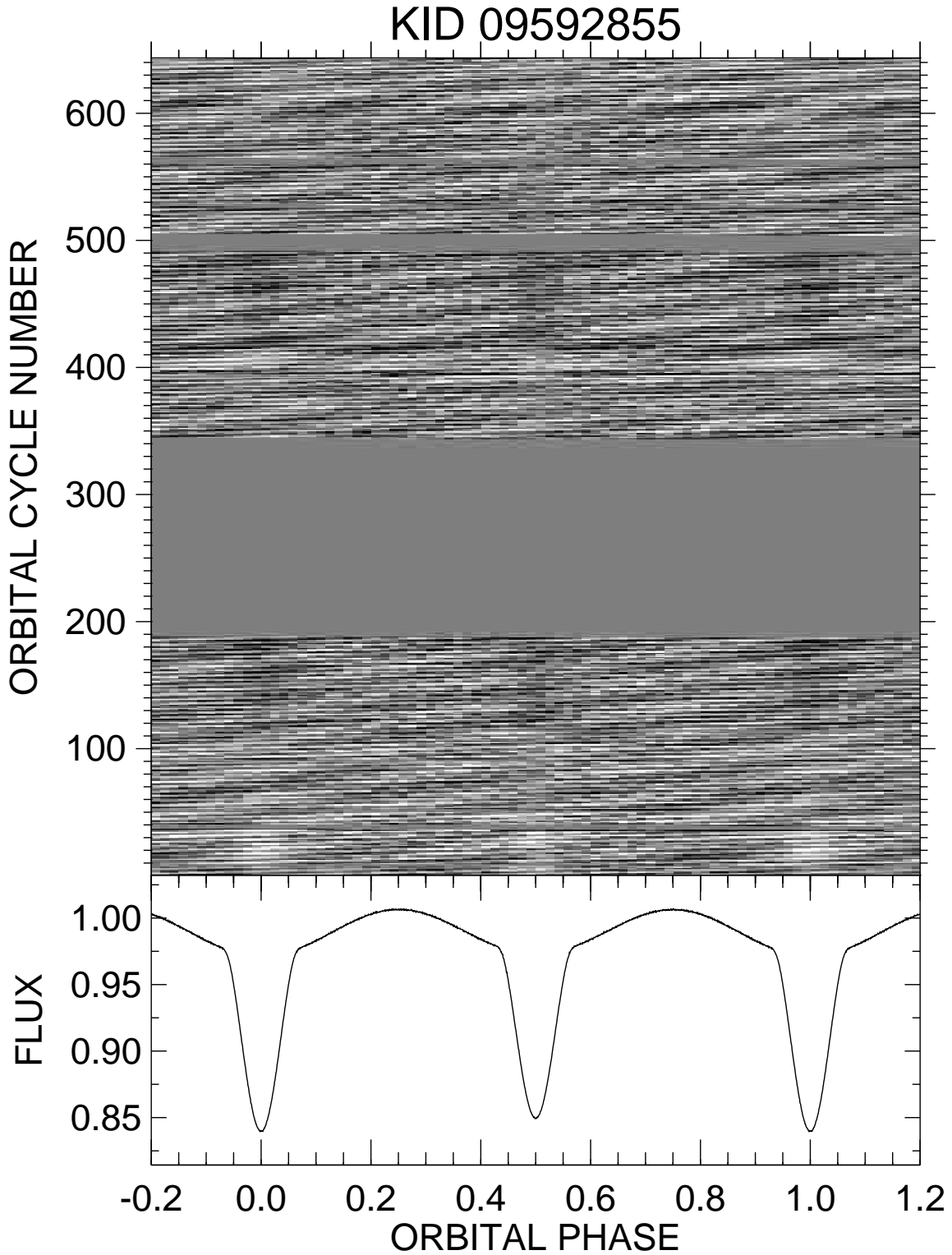


Fig. 1.27.— The lower panel shows a mean, normalized light curve formed by binning in orbital phase. The top panel shows the flux differences as a function of orbital phase and cycle number, represented as a gray scale diagram (range  $\pm 0.3\%$ ).



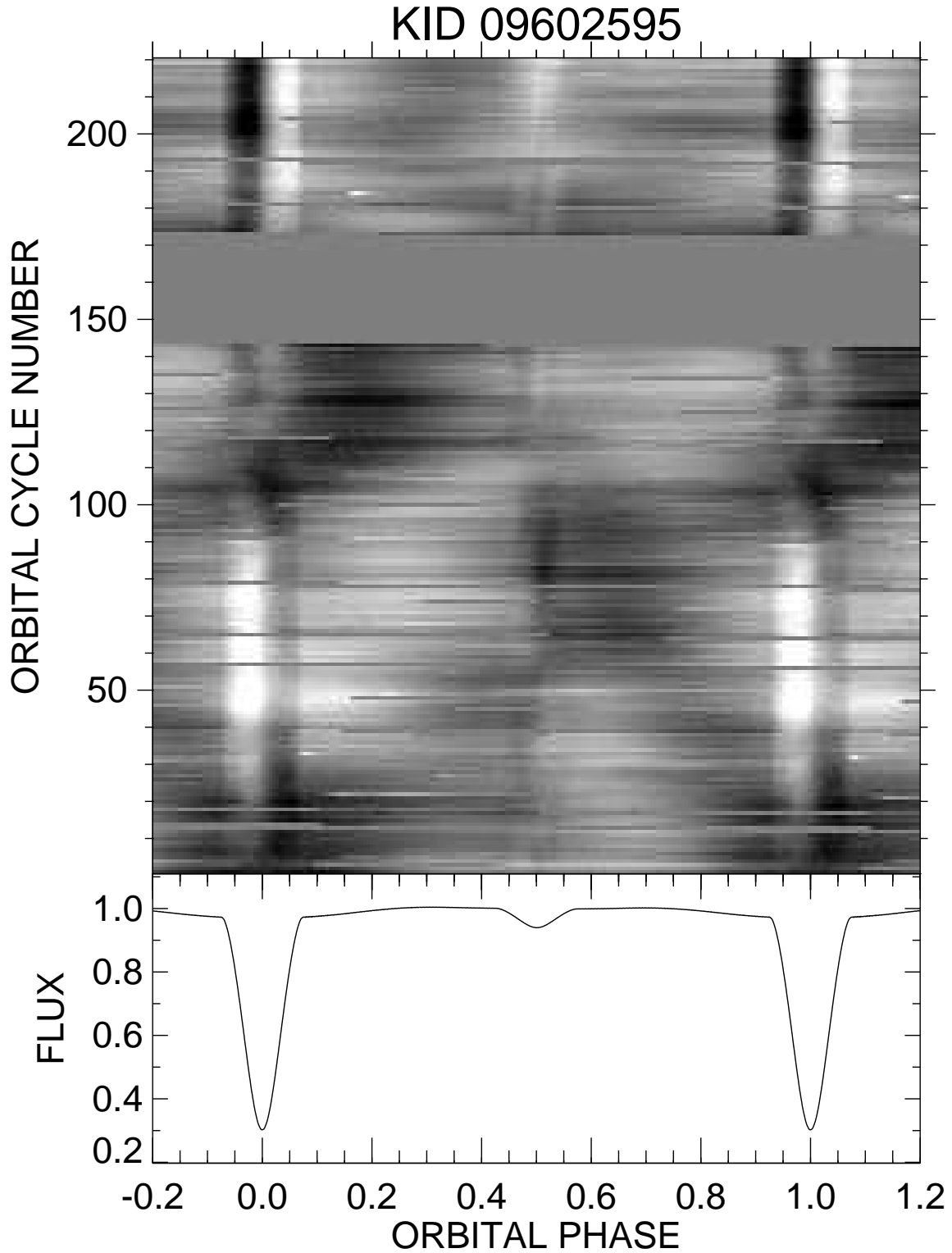


Fig. 1.28.— The lower panel shows a mean, normalized light curve formed by binning in orbital phase. The top panel shows the flux differences as a function of orbital phase and cycle number, represented as a gray scale diagram (range  $\pm 0.5\%$ ).

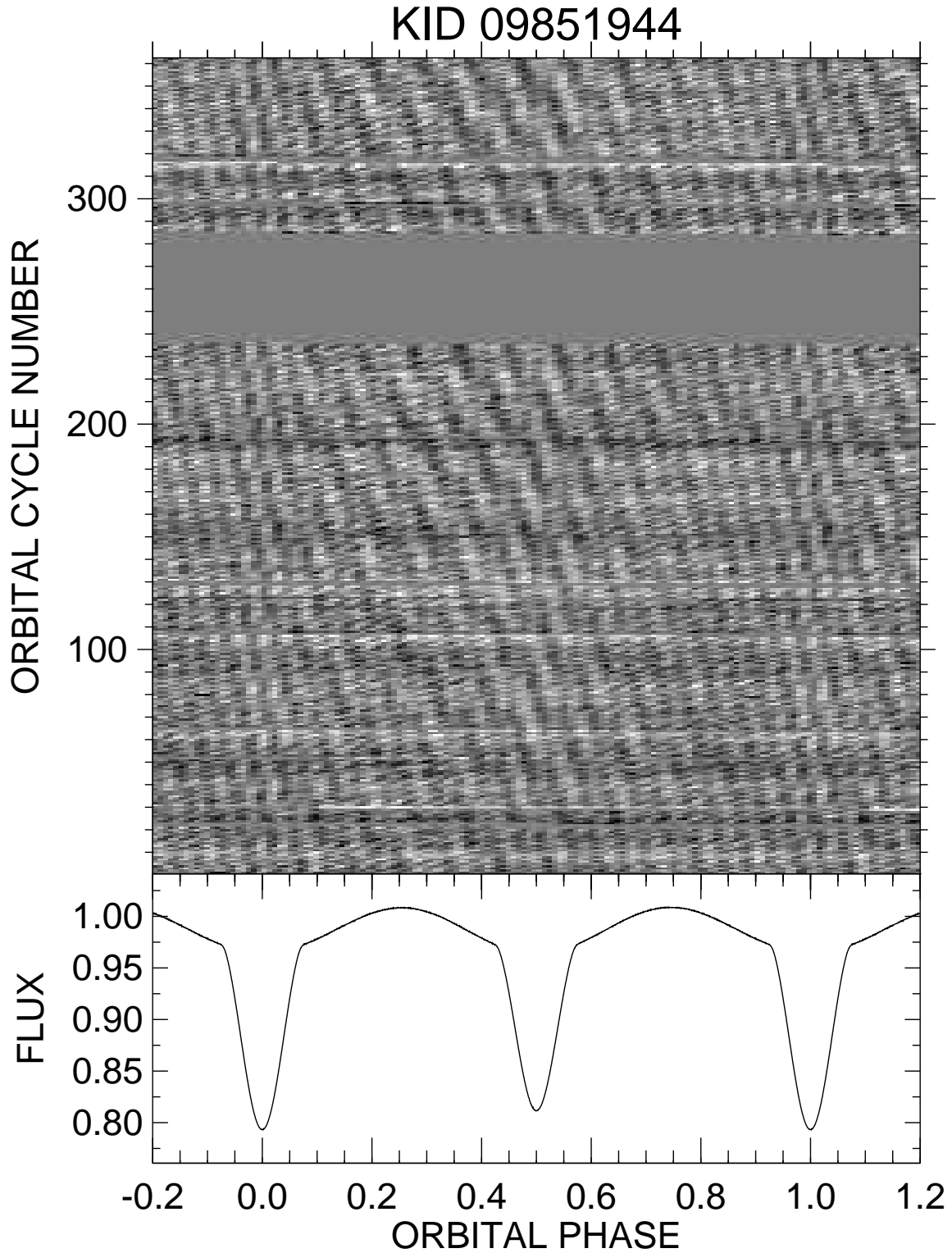


Fig. 1.29.— The lower panel shows a mean, normalized light curve formed by binning in orbital phase. The top panel shows the flux differences as a function of orbital phase and cycle number, represented as a gray scale diagram (range  $\pm 0.3\%$ ).

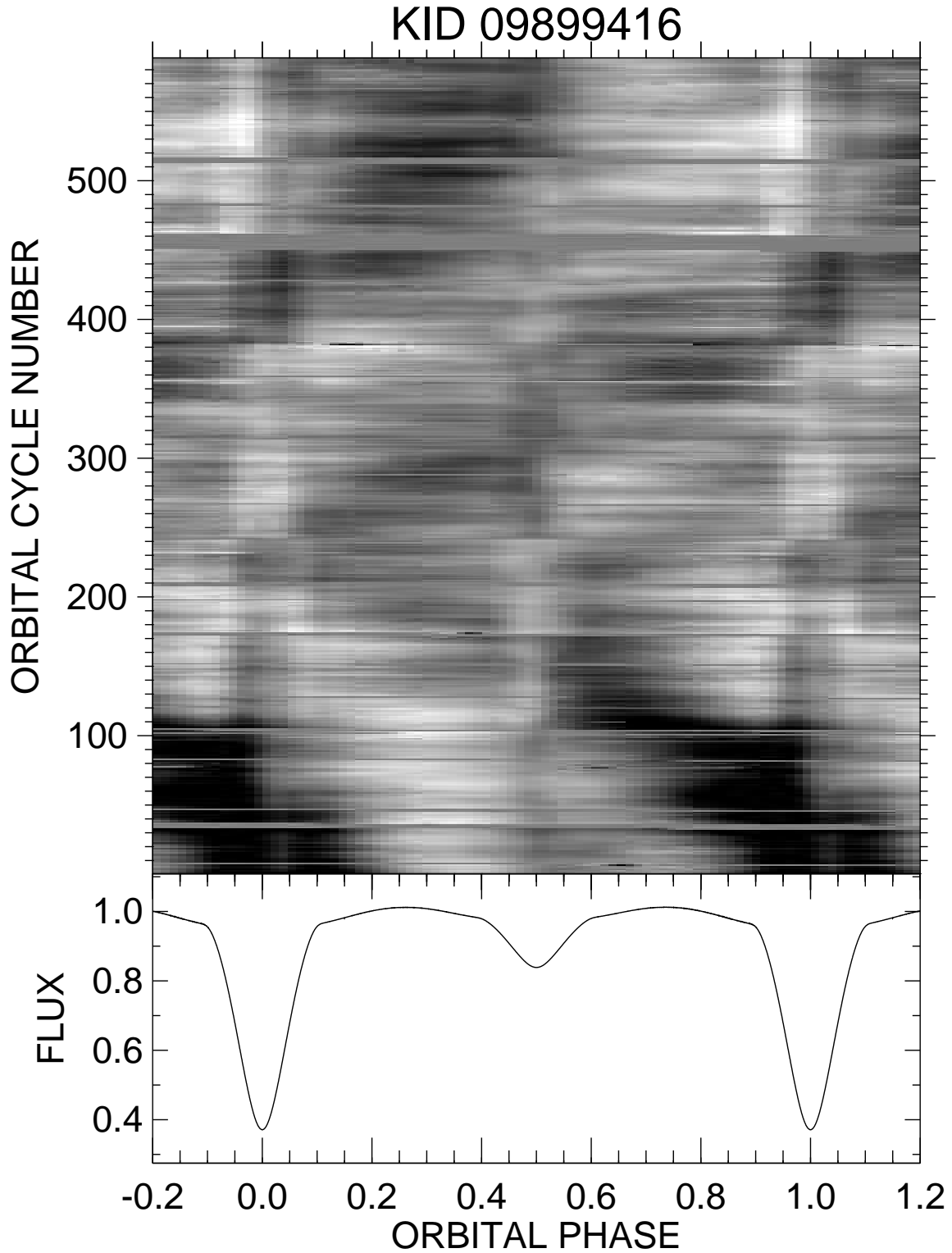


Fig. 1.30.— The lower panel shows a mean, normalized light curve formed by binning in orbital phase. The top panel shows the flux differences as a function of orbital phase and cycle number, represented as a gray scale diagram (range  $\pm 0.4\%$ ).

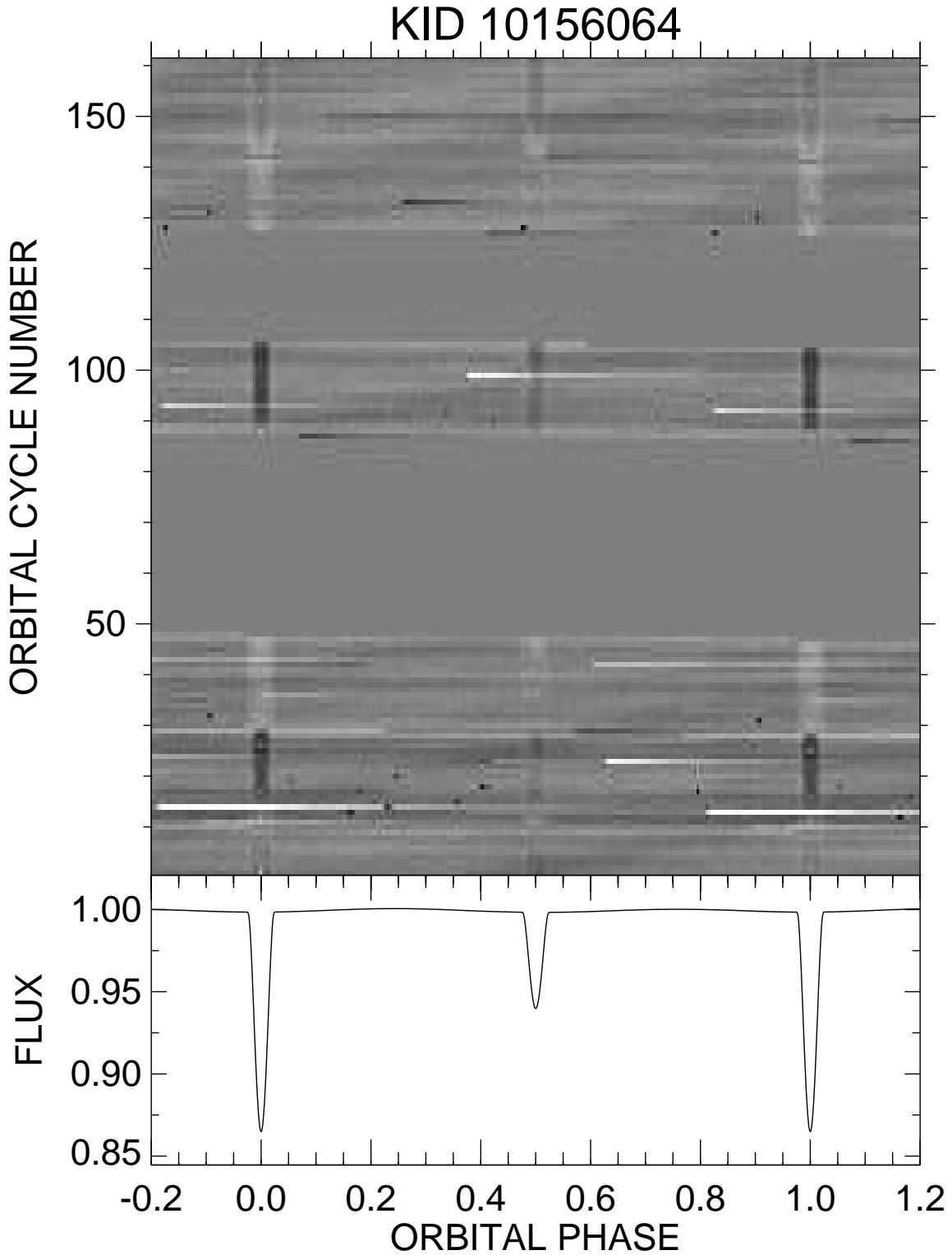


Fig. 1.31.— The lower panel shows a mean, normalized light curve formed by binning in orbital phase. The top panel shows the flux differences as a function of orbital phase and cycle number, represented as a gray scale diagram (range  $\pm 0.1\%$ ).

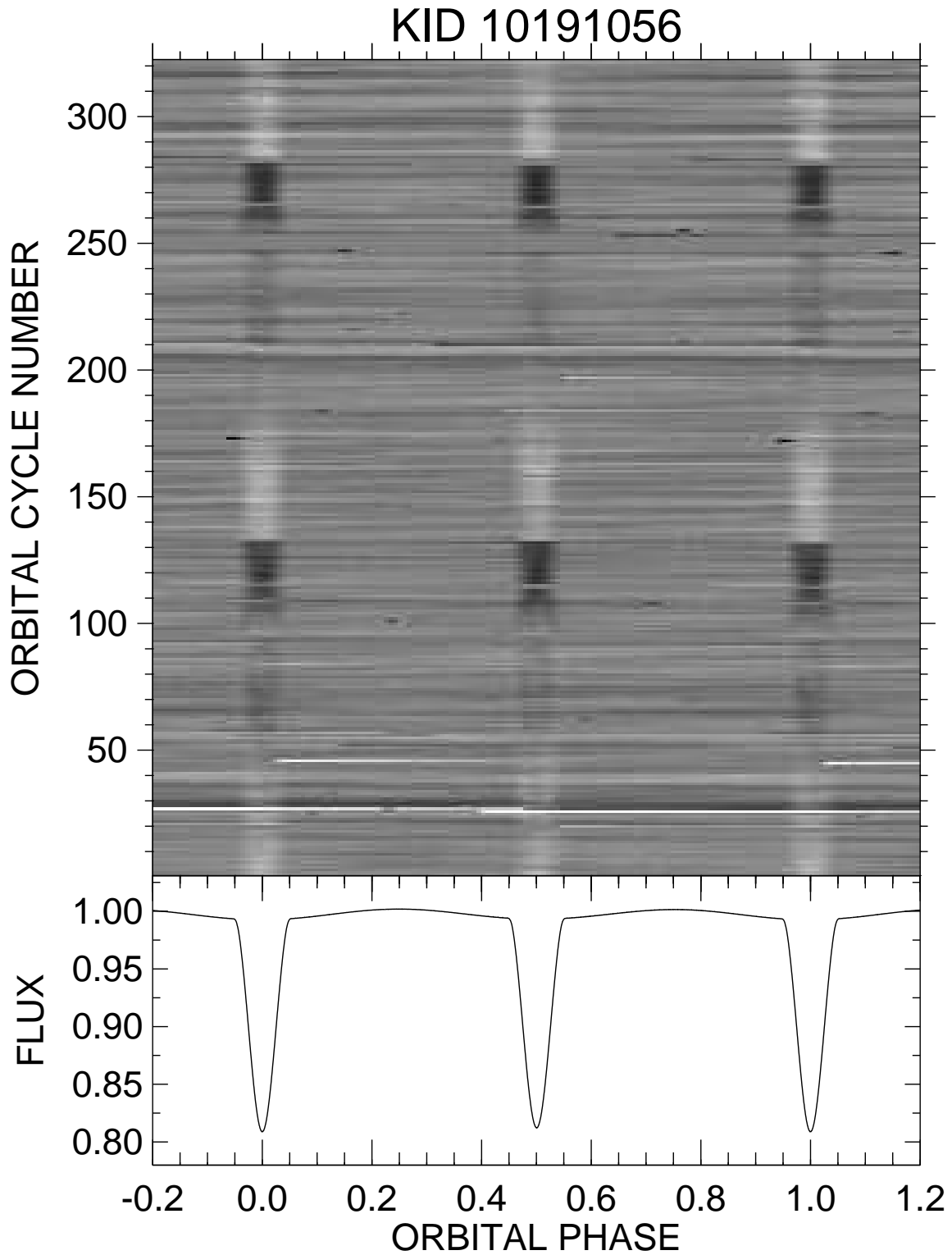


Fig. 1.32.— The lower panel shows a mean, normalized light curve formed by binning in orbital phase. The top panel shows the flux differences as a function of orbital phase and cycle number, represented as a gray scale diagram (range  $\pm 0.2\%$ ).

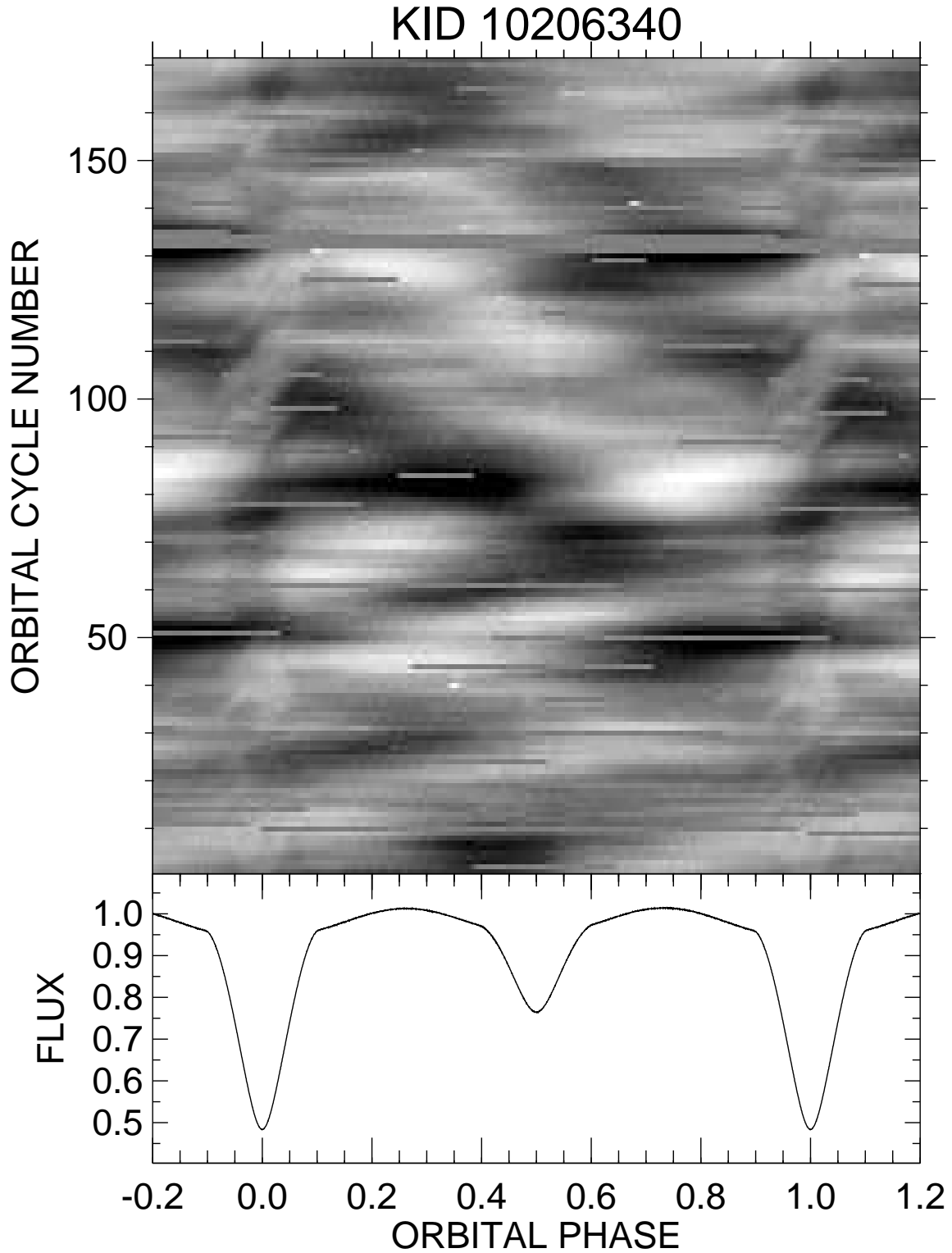


Fig. 1.33.— The lower panel shows a mean, normalized light curve formed by binning in orbital phase. The top panel shows the flux differences as a function of orbital phase and cycle number, represented as a gray scale diagram (range  $\pm 2\%$ ).

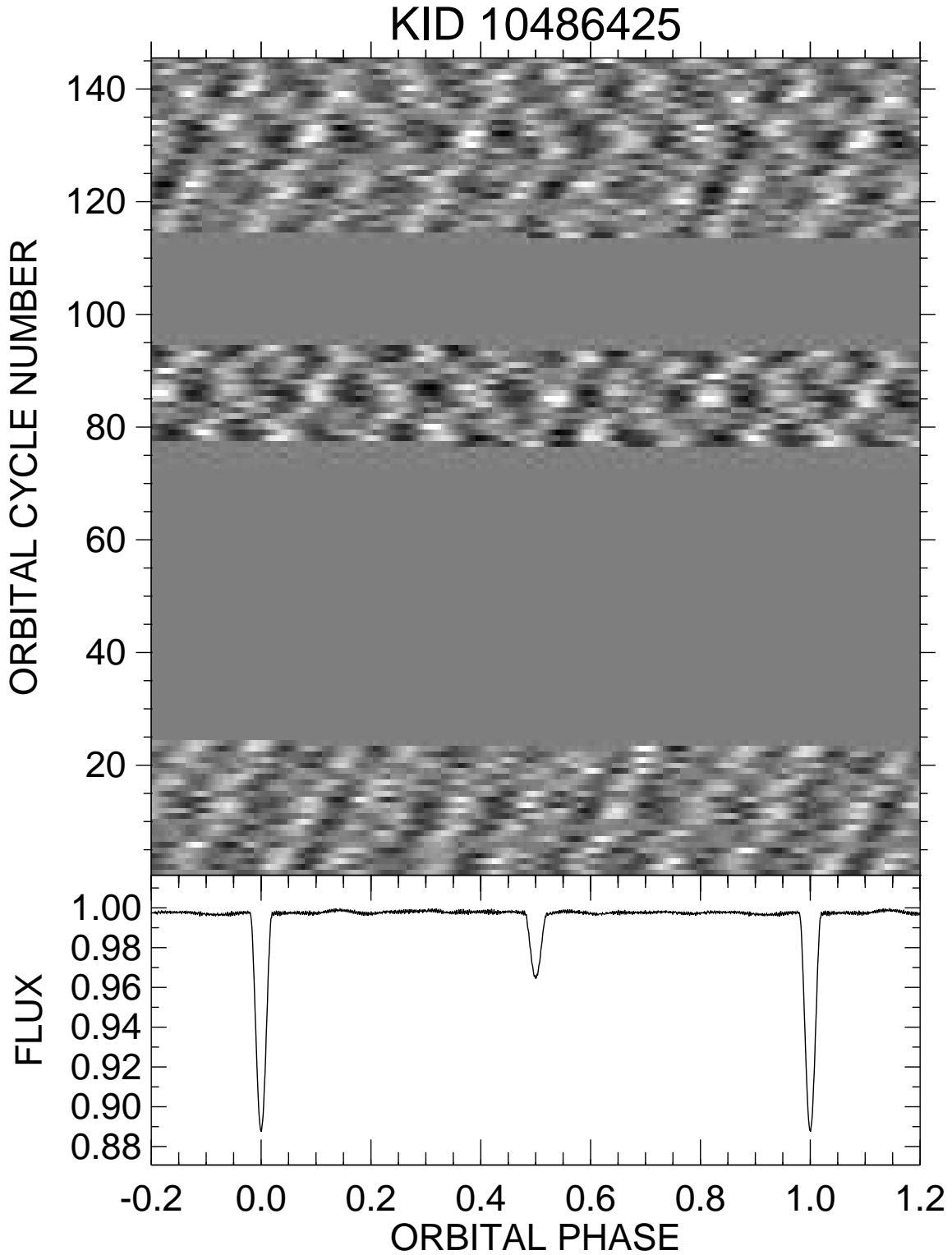


Fig. 1.34.— The lower panel shows a mean, normalized light curve formed by binning in orbital phase. The top panel shows the flux differences as a function of orbital phase and cycle number, represented as a gray scale diagram (range  $\pm 1\%$ ).

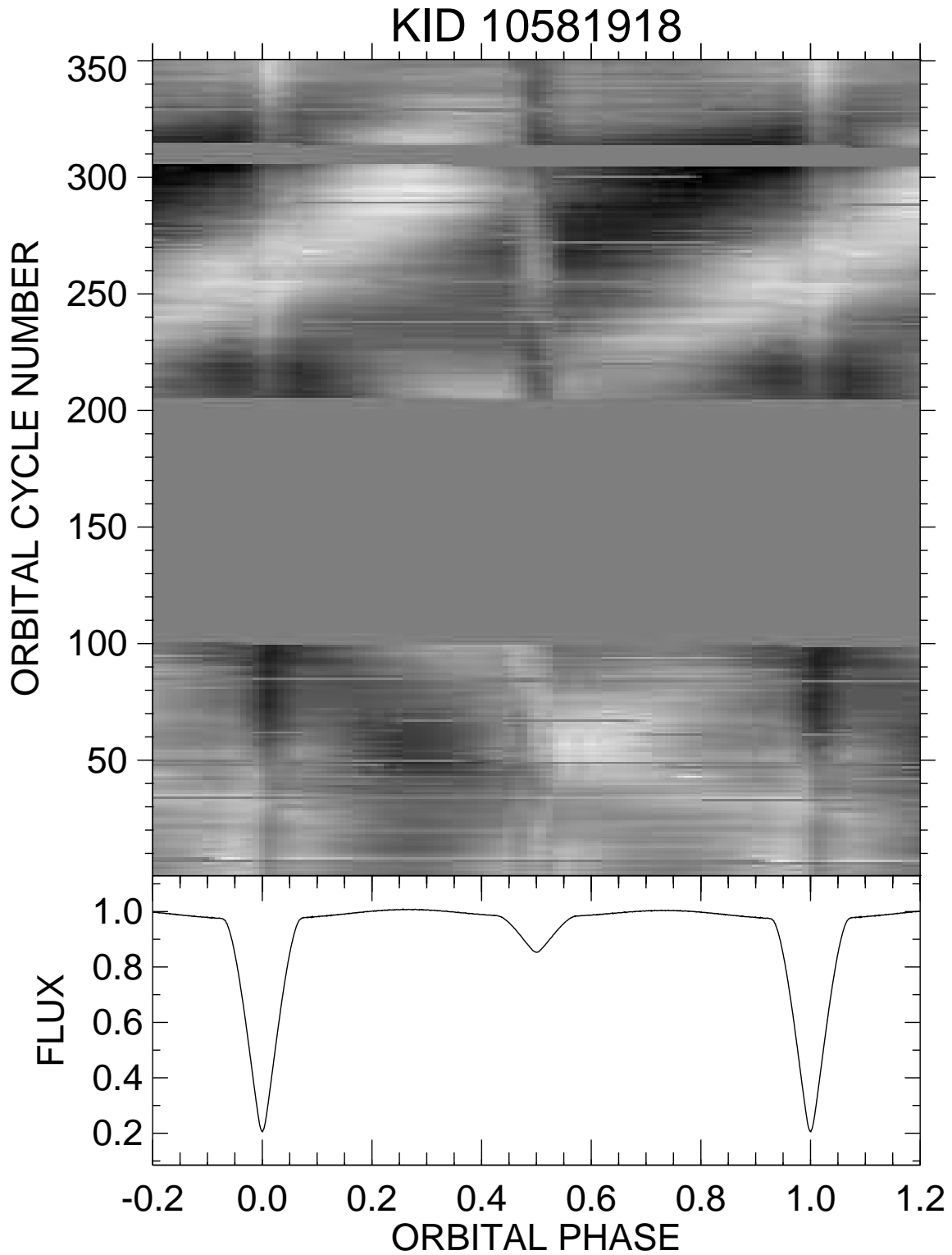


Fig. 1.35.— The lower panel shows a mean, normalized light curve formed by binning in orbital phase. The top panel shows the flux differences as a function of orbital phase and cycle number, represented as a gray scale diagram (range  $\pm 2\%$ ).



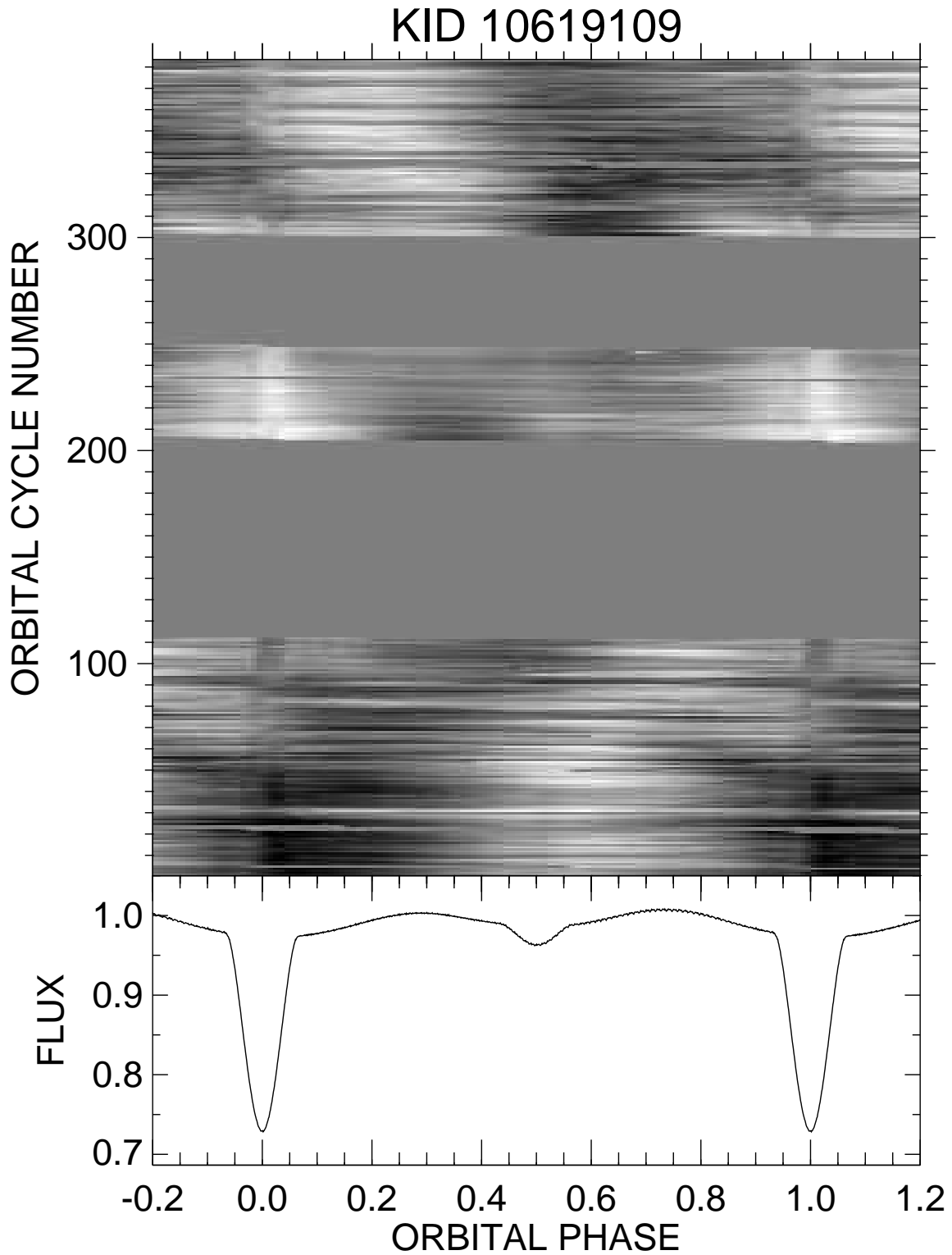


Fig. 1.36.— The lower panel shows a mean, normalized light curve formed by binning in orbital phase. The top panel shows the flux differences as a function of orbital phase and cycle number, represented as a gray scale diagram (range  $\pm 1\%$ ).

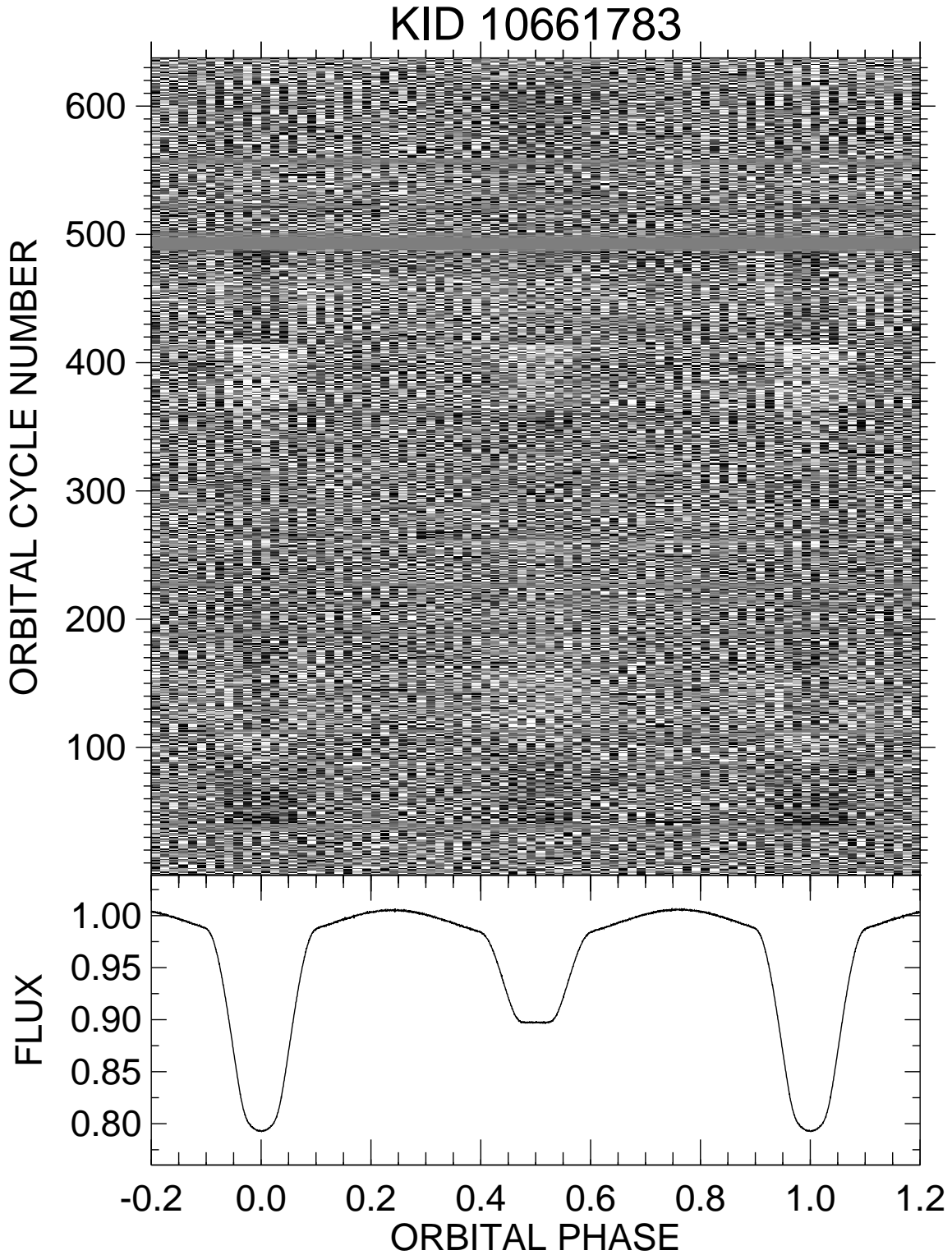


Fig. 1.37.— The lower panel shows a mean, normalized light curve formed by binning in orbital phase. The top panel shows the flux differences as a function of orbital phase and cycle number, represented as a gray scale diagram (range  $\pm 0.2\%$ ).

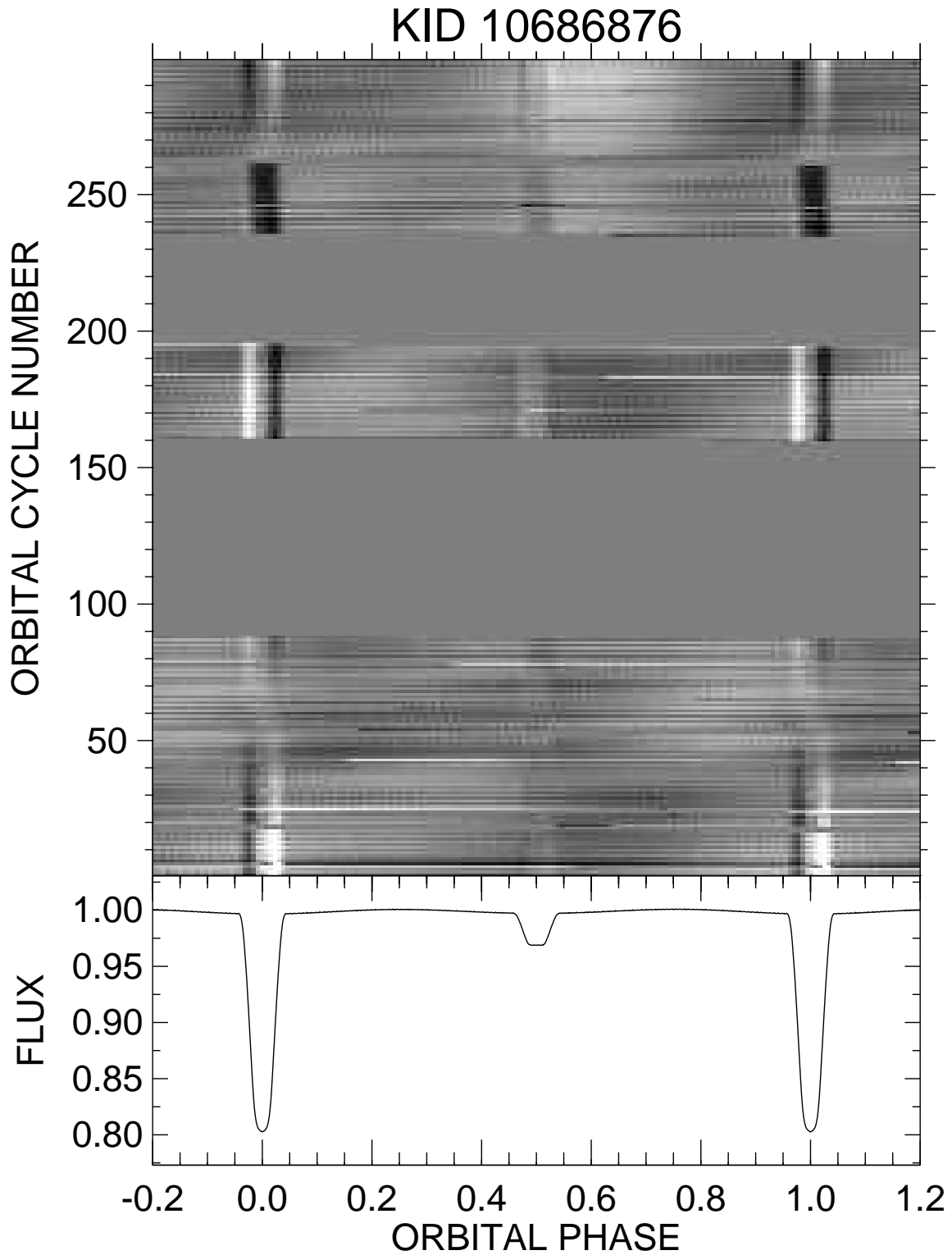


Fig. 1.38.— The lower panel shows a mean, normalized light curve formed by binning in orbital phase. The top panel shows the flux differences as a function of orbital phase and cycle number, represented as a gray scale diagram (range  $\pm 0.3\%$ ).

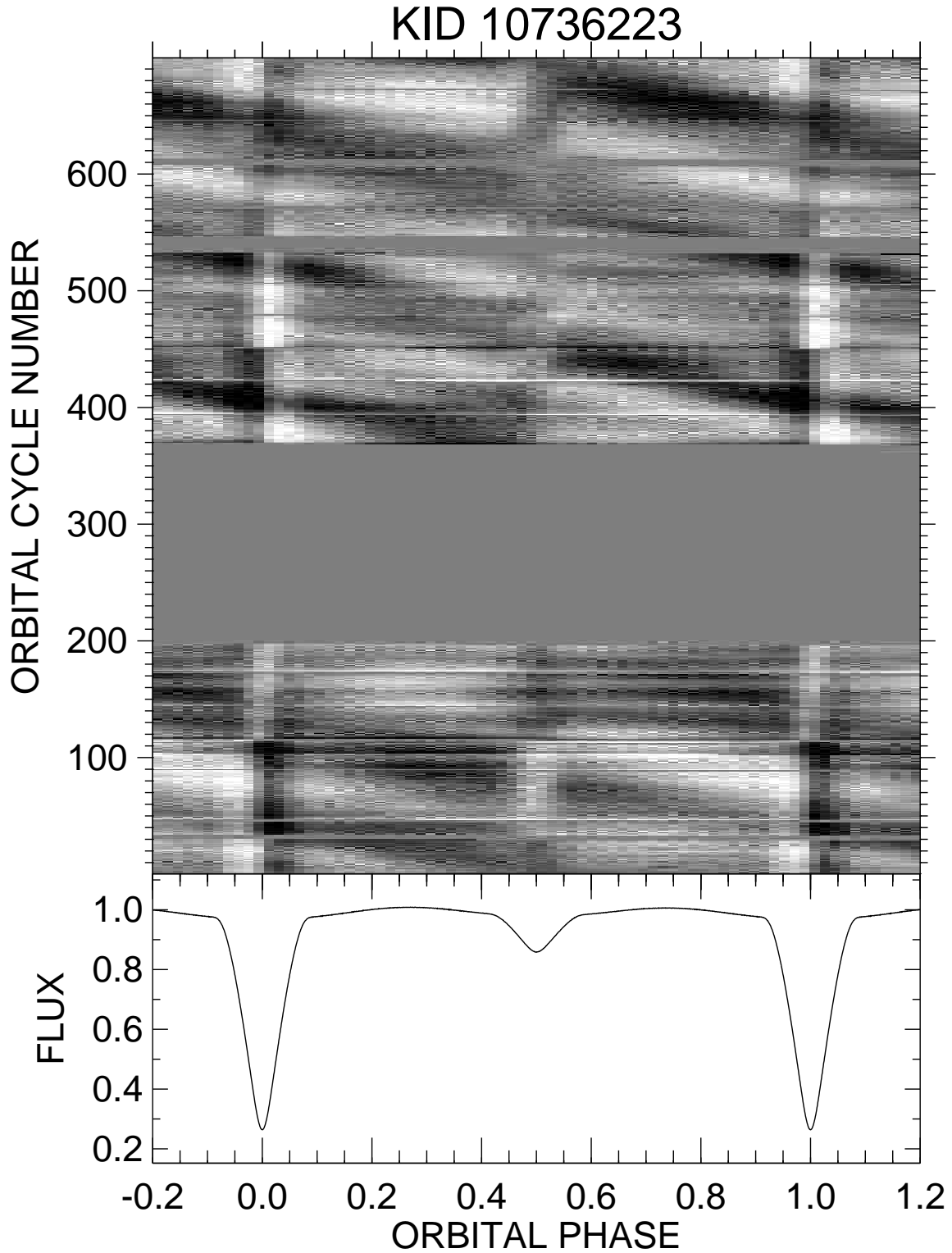


Fig. 1.39.— The lower panel shows a mean, normalized light curve formed by binning in orbital phase. The top panel shows the flux differences as a function of orbital phase and cycle number, represented as a gray scale diagram (range  $\pm 0.5\%$ ).

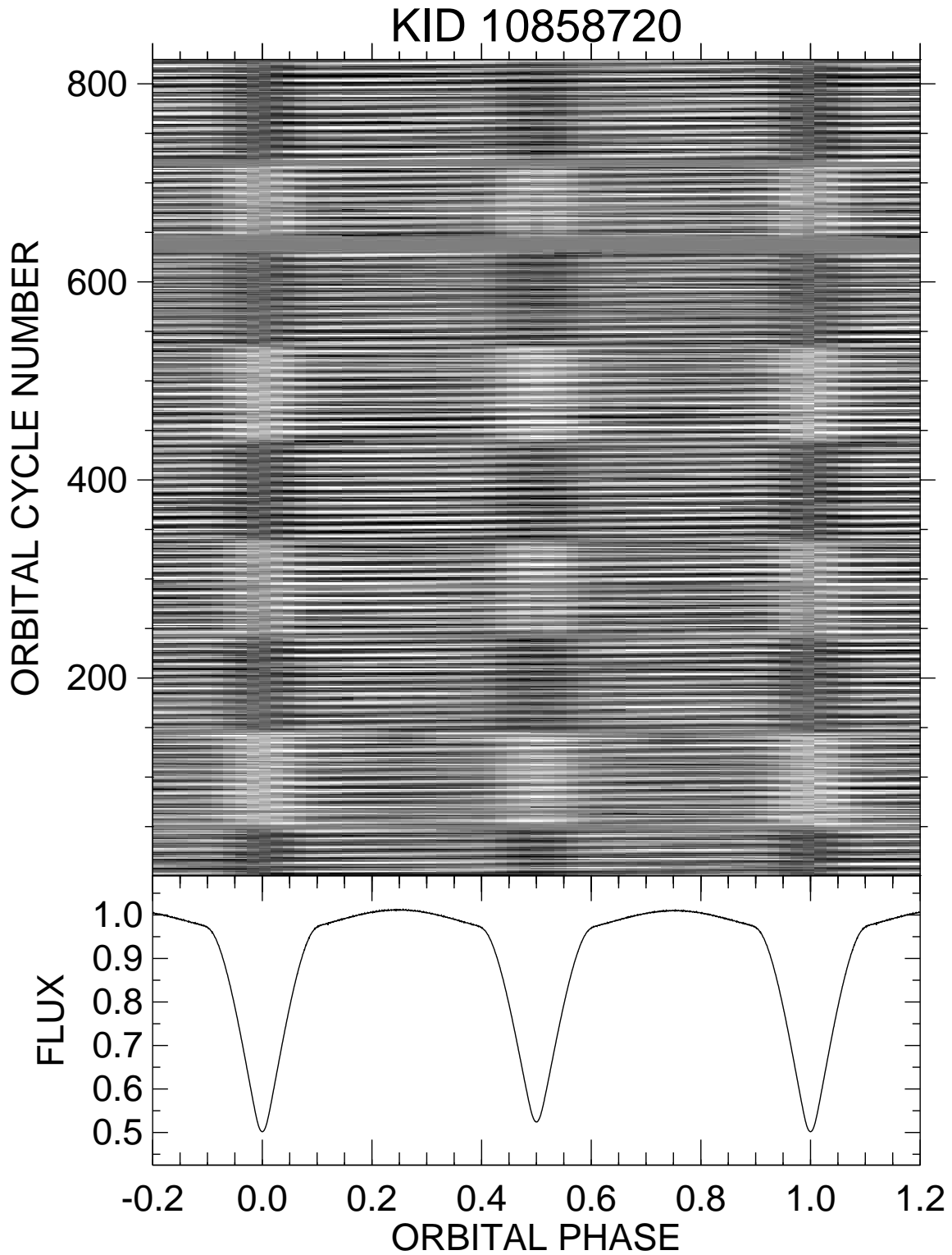


Fig. 1.40.— The lower panel shows a mean, normalized light curve formed by binning in orbital phase. The top panel shows the flux differences as a function of orbital phase and cycle number, represented as a gray scale diagram (range  $\pm 0.5\%$ ).

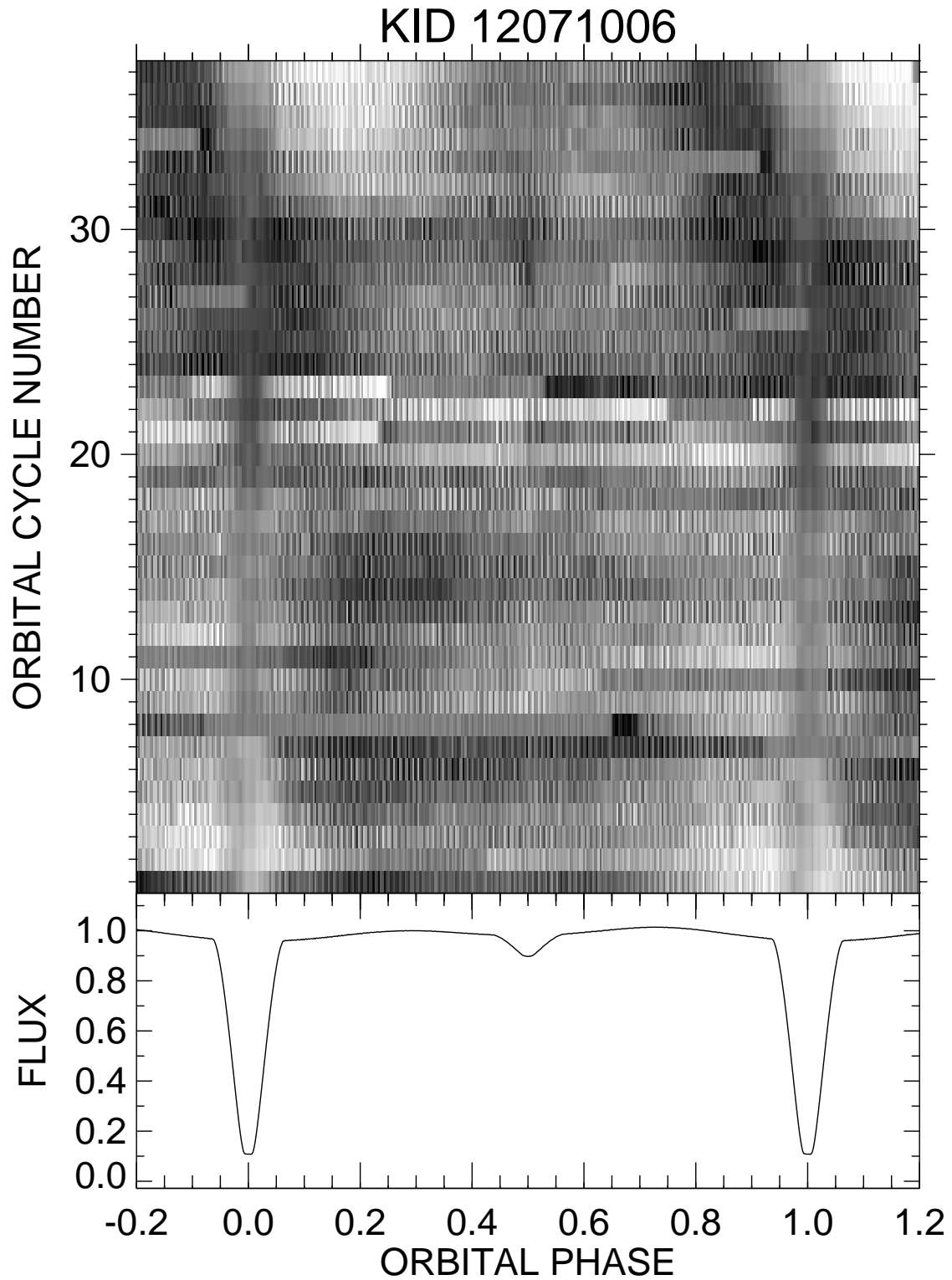


Fig. 1.41.— The lower panel shows a mean, normalized light curve formed by binning in orbital phase. The top panel shows the flux differences as a function of orbital phase and cycle number, represented as a gray scale diagram (range  $\pm 1\%$ ).

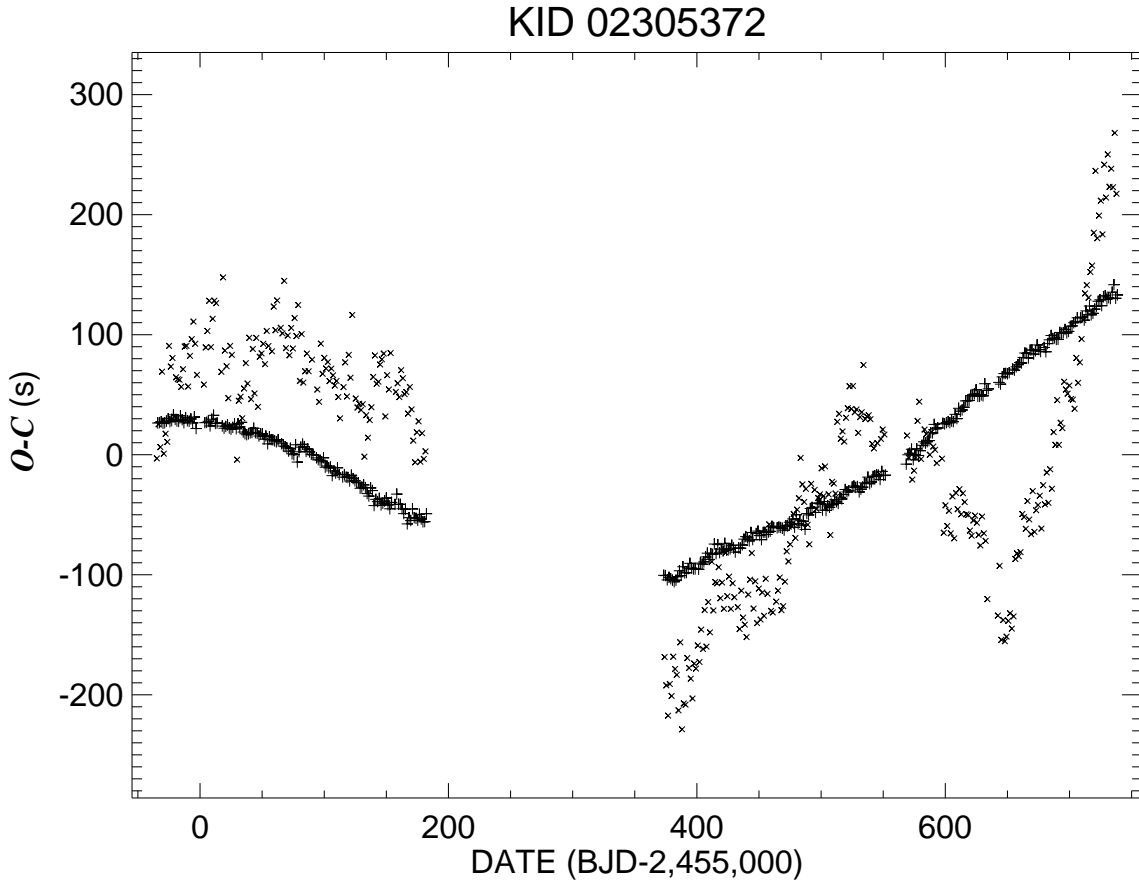


Fig. 2.1.— The observed minus calculated eclipse times relative to a linear ephemeris. The primary and secondary eclipse times are indicated by + and × symbols, respectively.

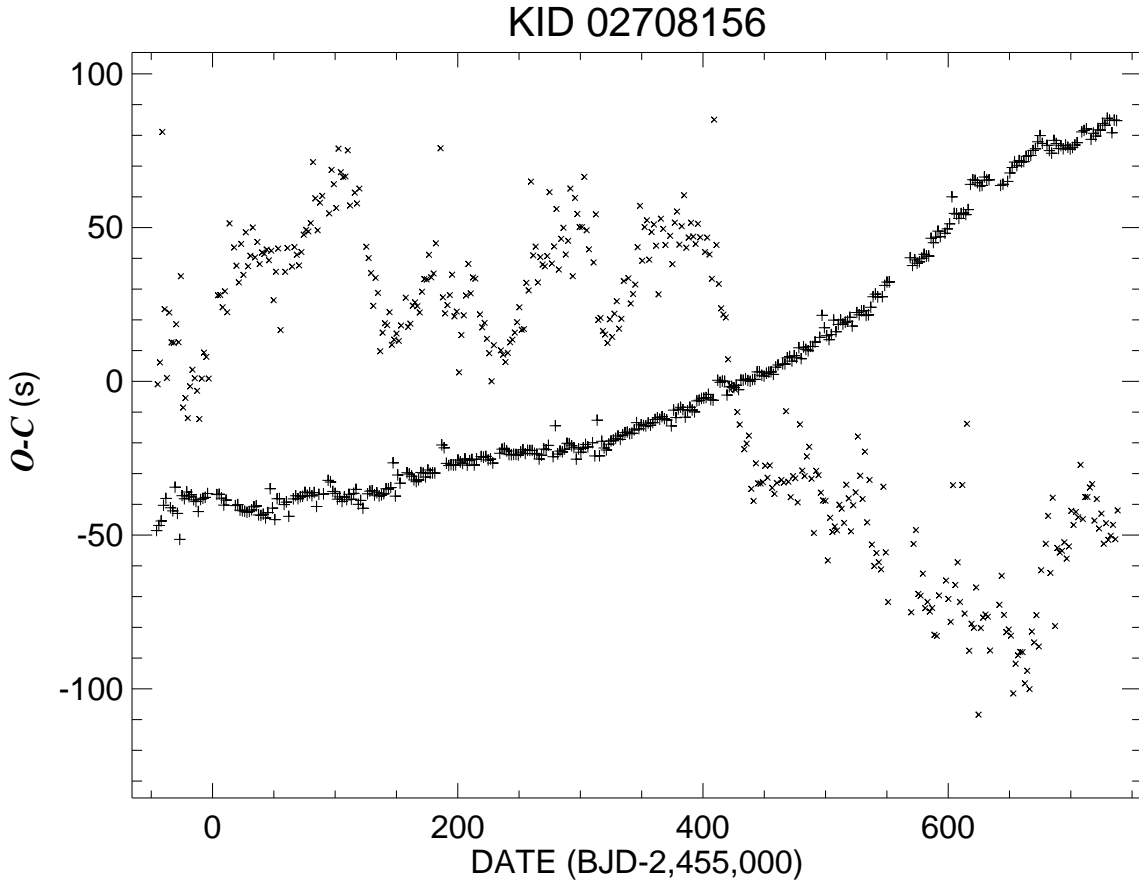


Fig. 2.2.— The observed minus calculated eclipse times relative to a linear ephemeris. The primary and secondary eclipse times are indicated by + and × symbols, respectively.



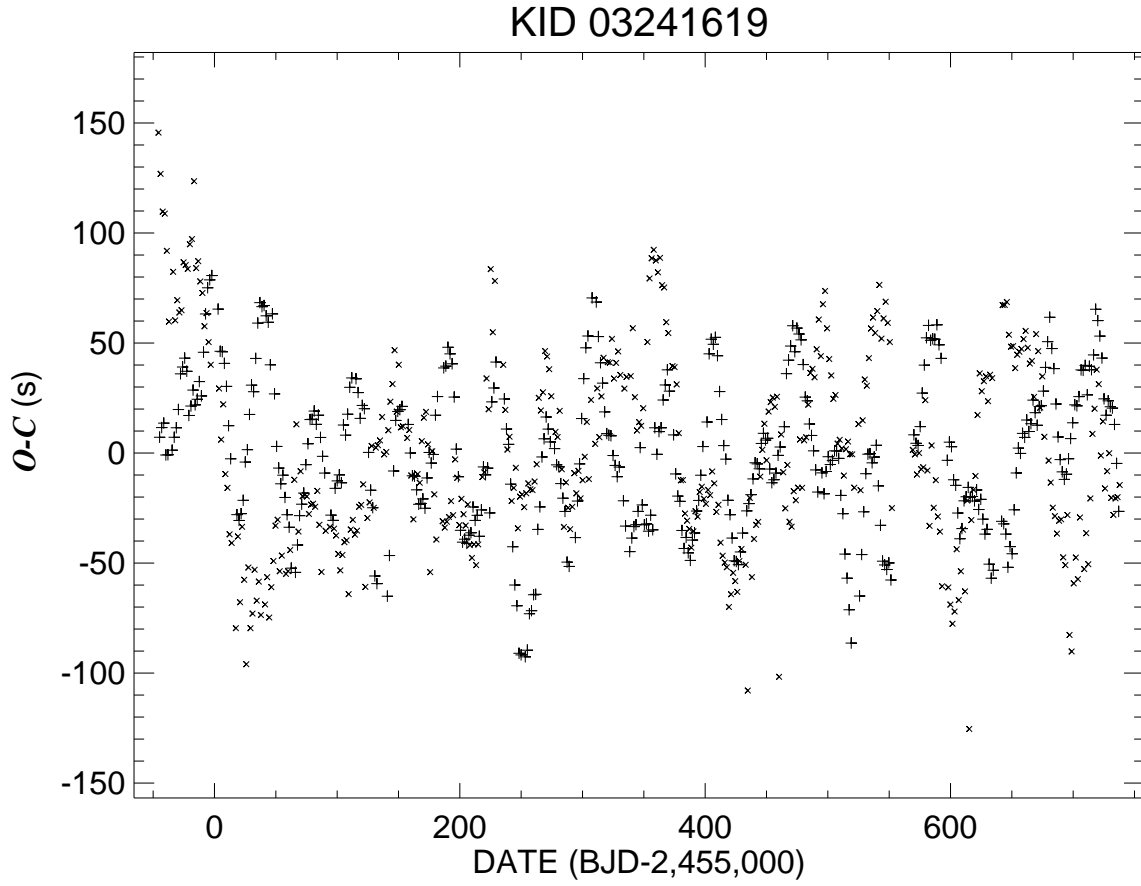


Fig. 2.3.— The observed minus calculated eclipse times relative to a linear ephemeris. The primary and secondary eclipse times are indicated by + and  $\times$  symbols, respectively.

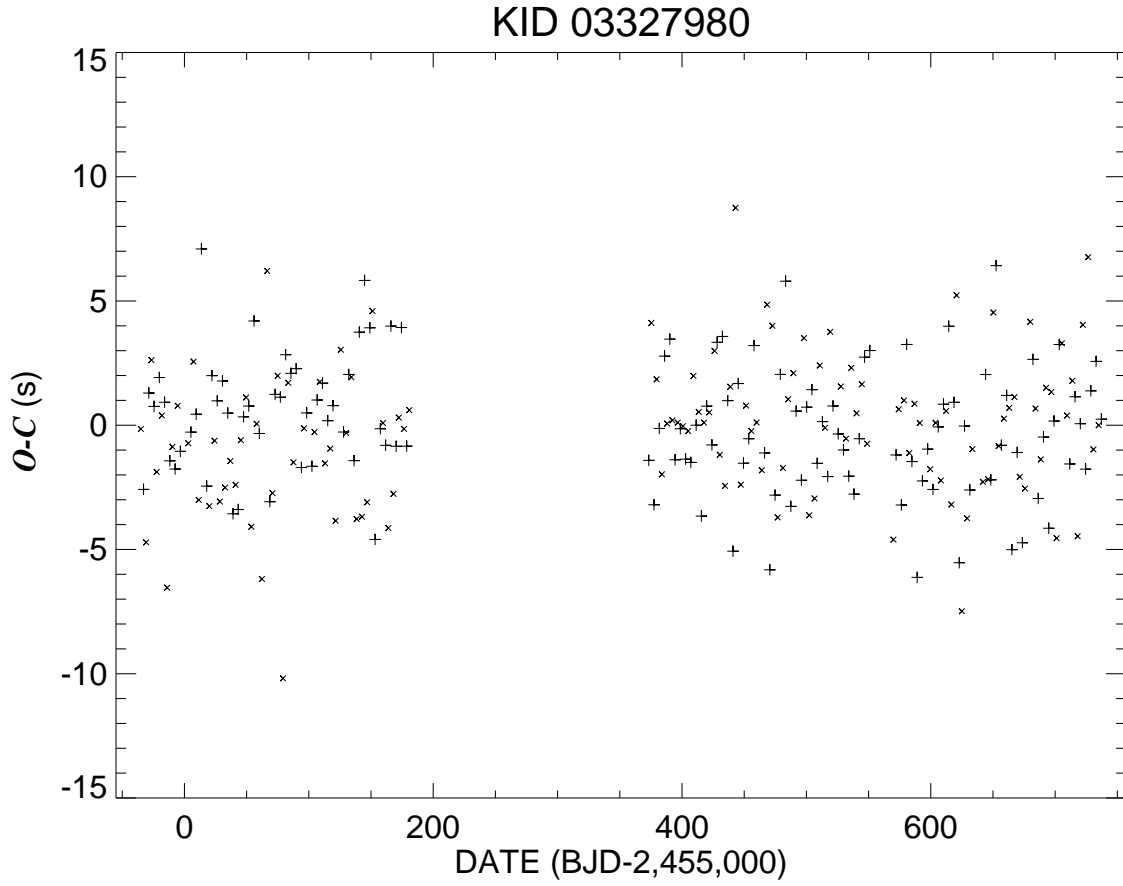


Fig. 2.4.— The observed minus calculated eclipse times relative to a linear ephemeris. The primary and secondary eclipse times are indicated by + and × symbols, respectively.

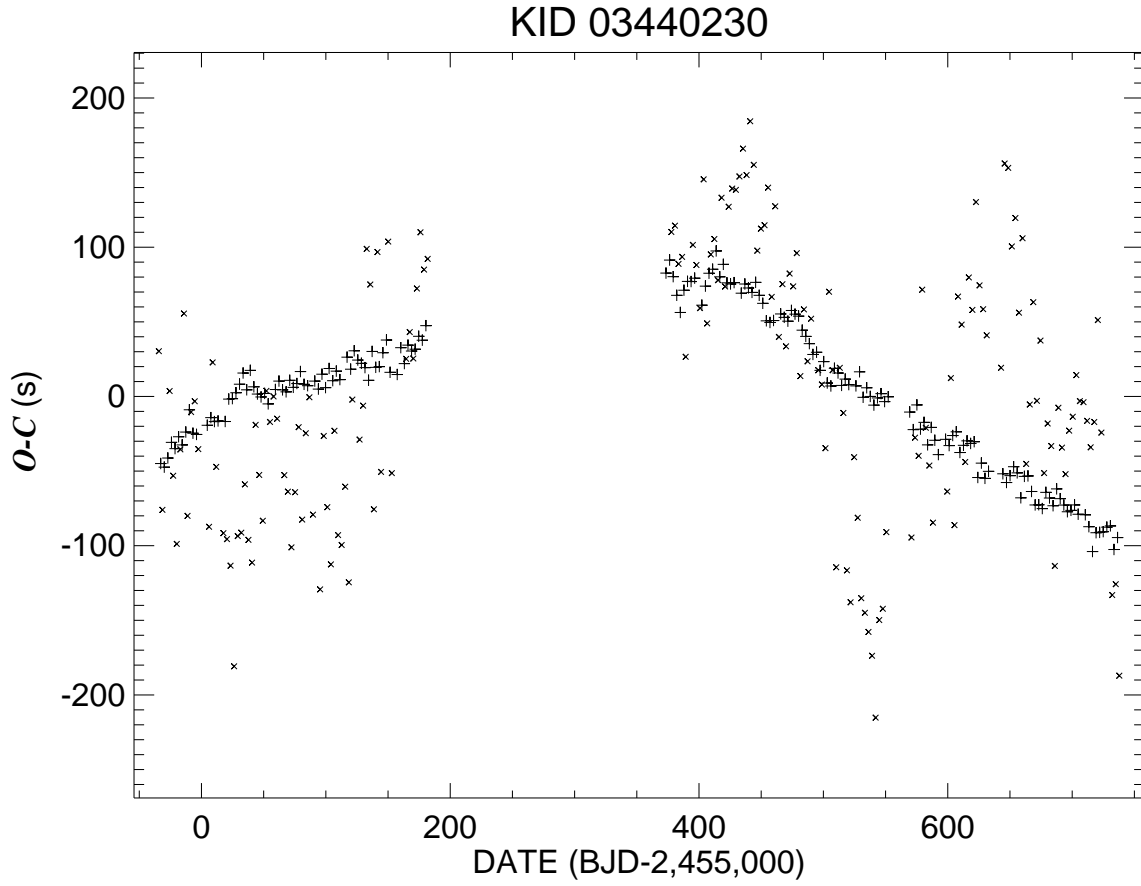


Fig. 2.5.— The observed minus calculated eclipse times relative to a linear ephemeris. The primary and secondary eclipse times are indicated by + and  $\times$  symbols, respectively.

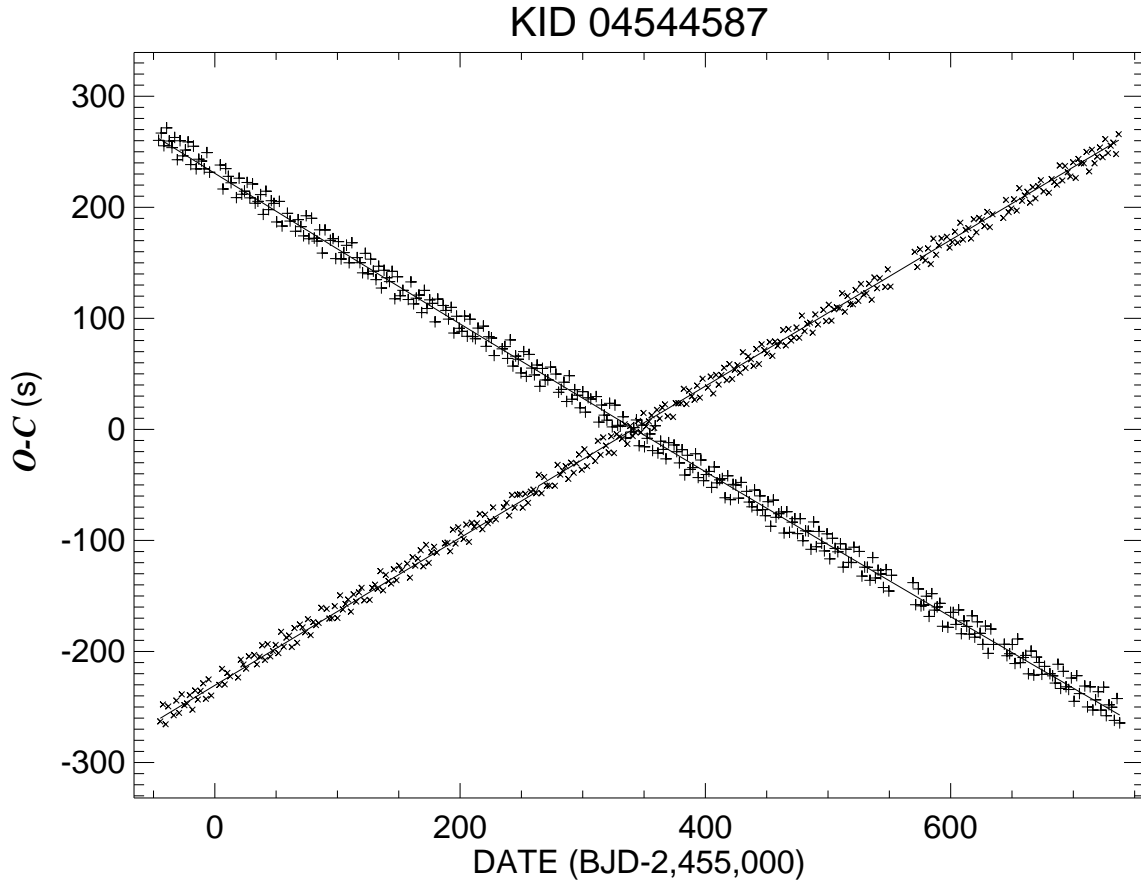


Fig. 2.6.— The observed minus calculated eclipse times relative to a linear ephemeris. The primary and secondary eclipse times are indicated by + and × symbols, respectively.

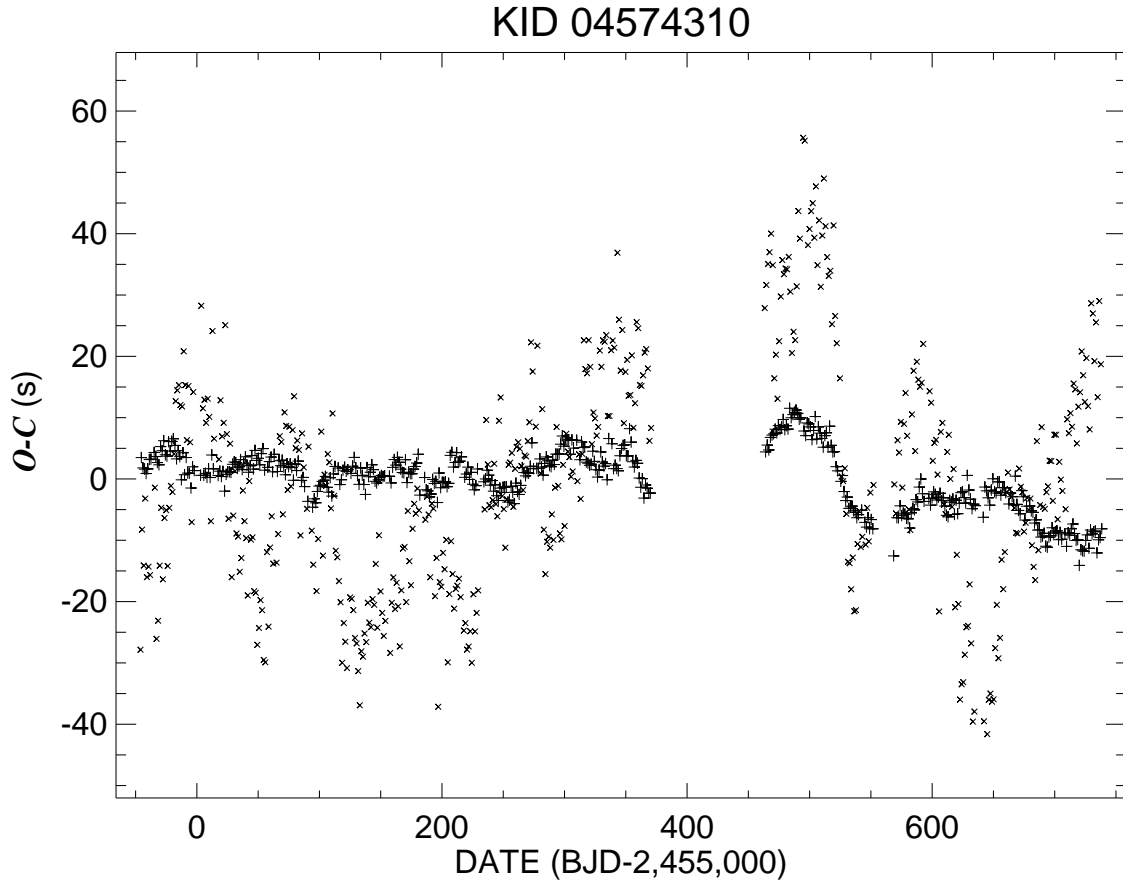


Fig. 2.7.— The observed minus calculated eclipse times relative to a linear ephemeris. The primary and secondary eclipse times are indicated by + and × symbols, respectively.

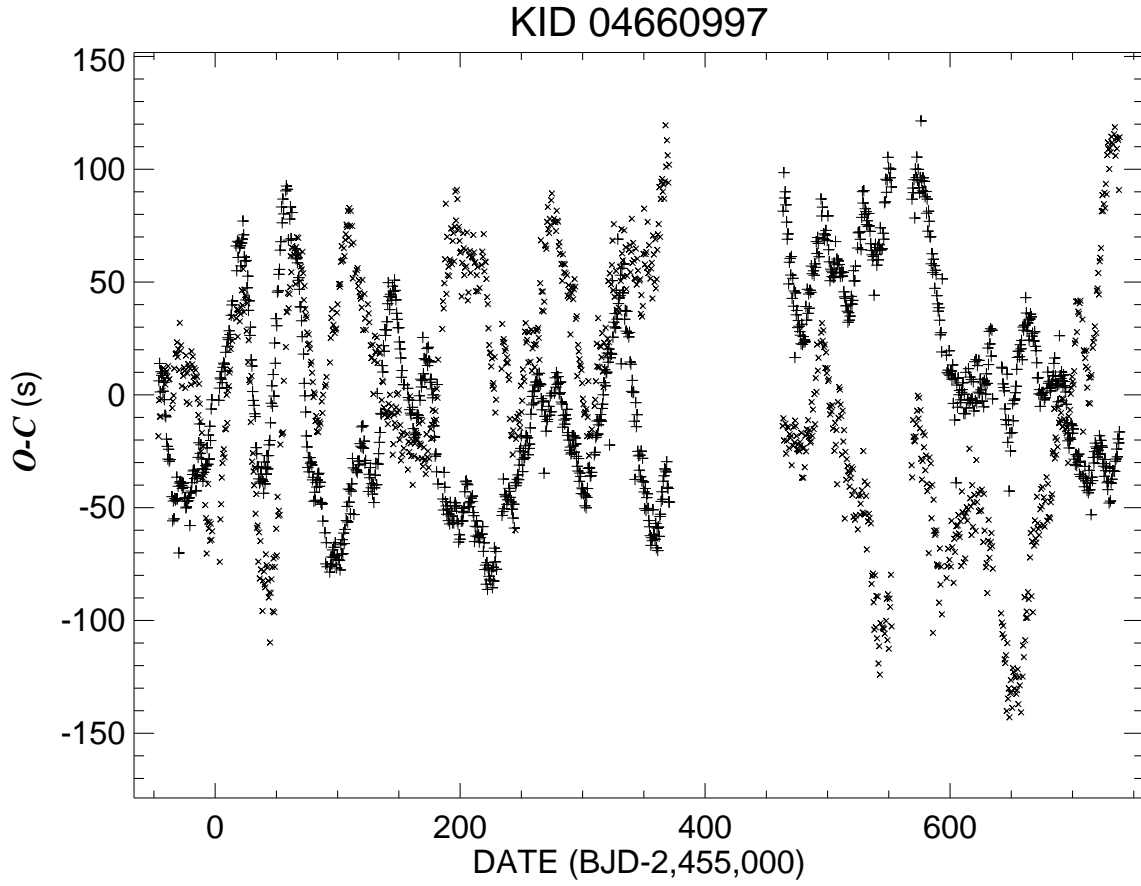


Fig. 2.8.— The observed minus calculated eclipse times relative to a linear ephemeris. The primary and secondary eclipse times are indicated by + and  $\times$  symbols, respectively.

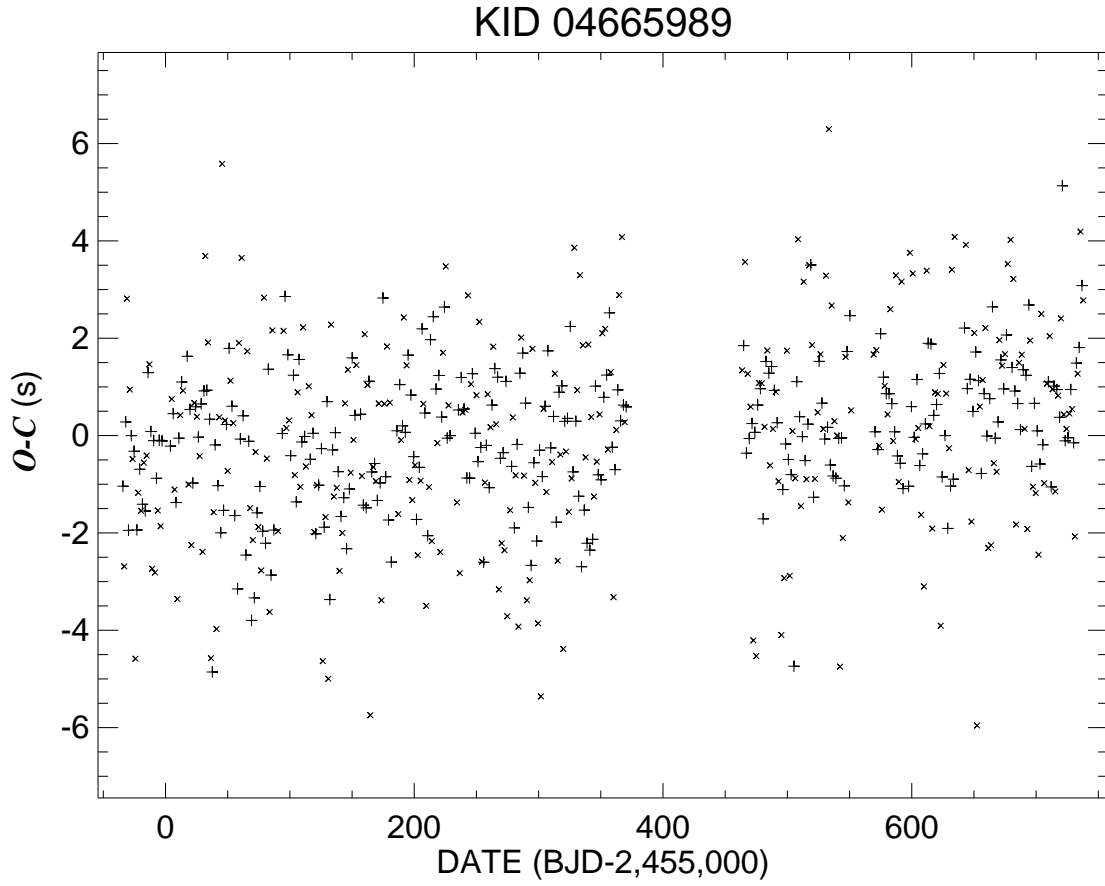


Fig. 2.9.— The observed minus calculated eclipse times relative to a linear ephemeris. The primary and secondary eclipse times are indicated by + and  $\times$  symbols, respectively.

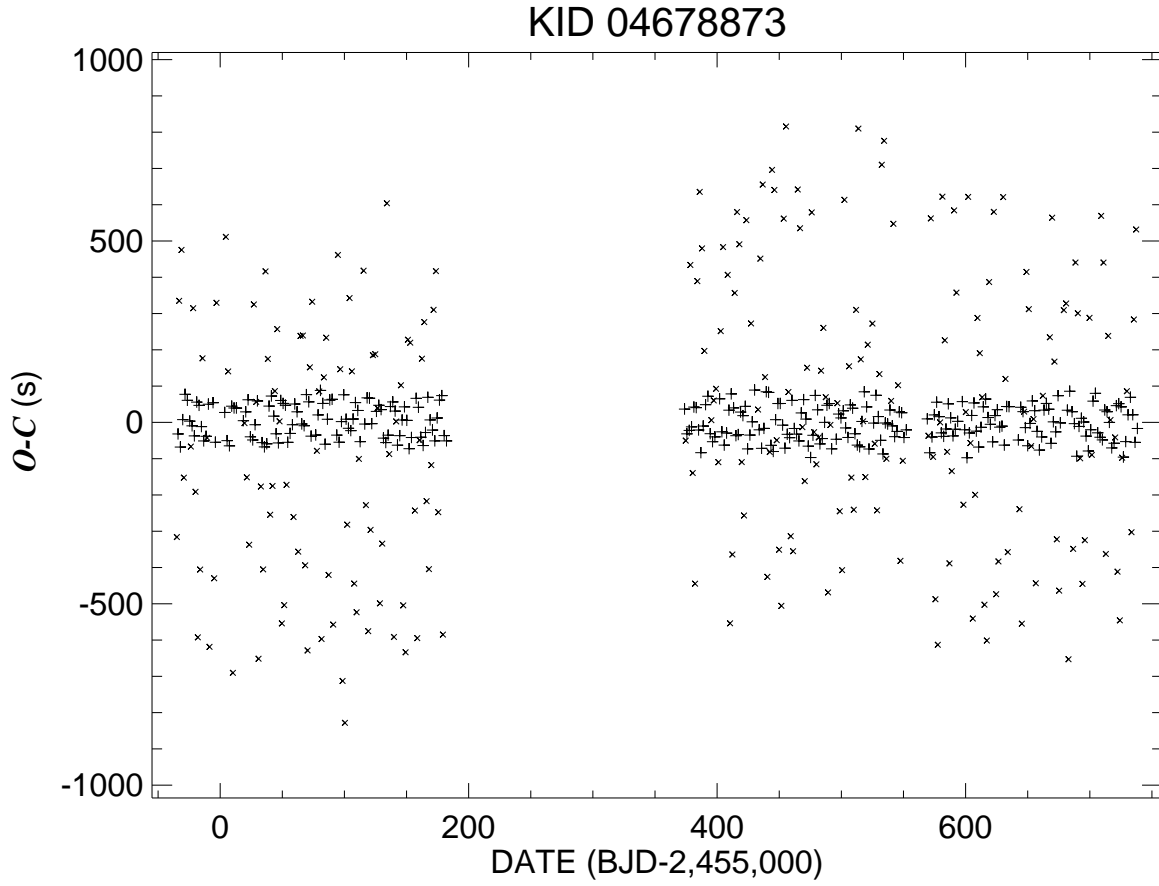


Fig. 2.10.— The observed minus calculated eclipse times relative to a linear ephemeris. The primary and secondary eclipse times are indicated by + and  $\times$  symbols, respectively.



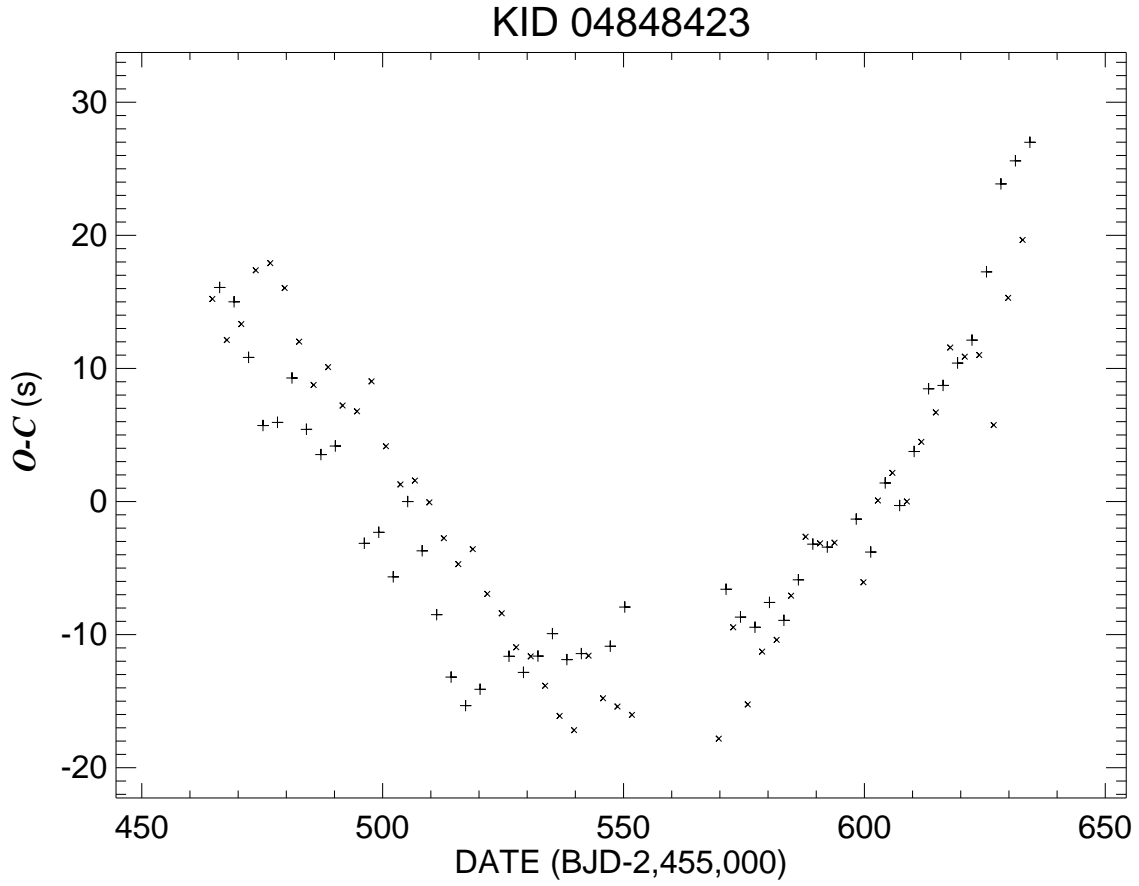


Fig. 2.11.— The observed minus calculated eclipse times relative to a linear ephemeris. The primary and secondary eclipse times are indicated by + and  $\times$  symbols, respectively.

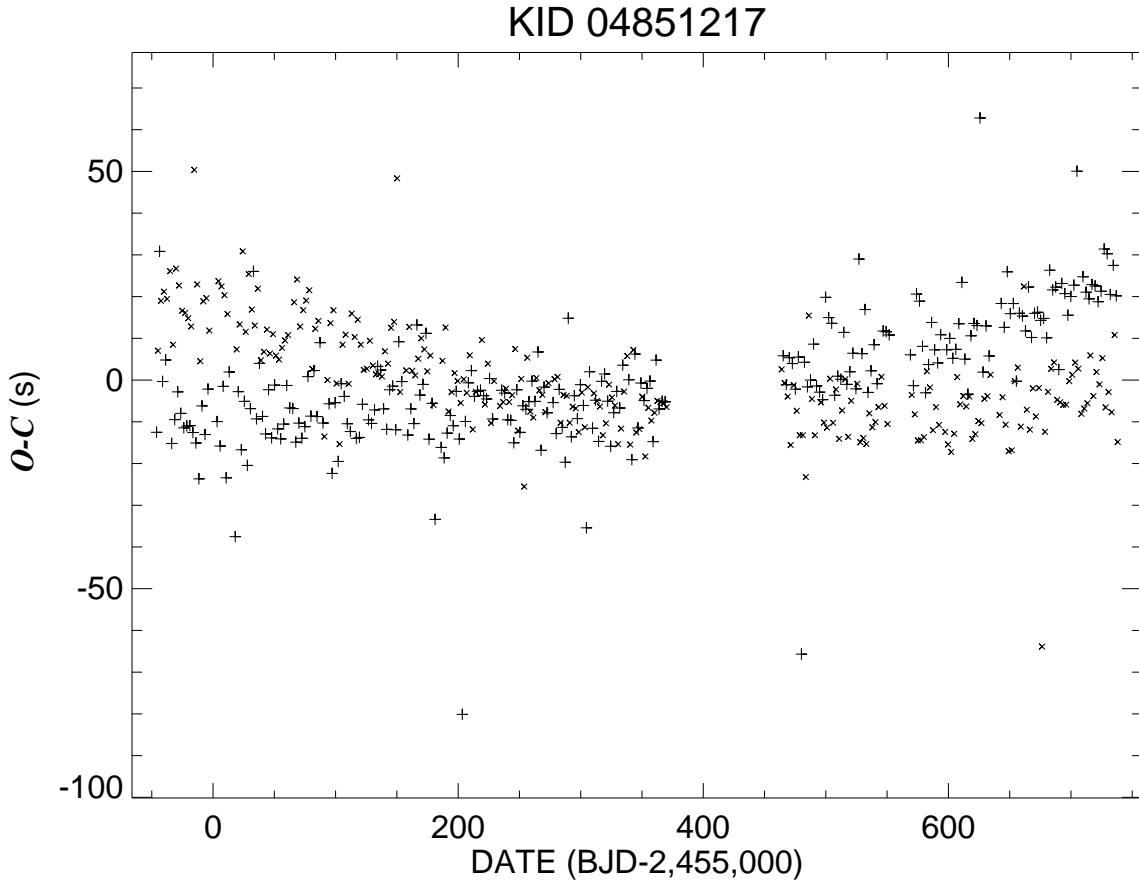


Fig. 2.12.— The observed minus calculated eclipse times relative to a linear ephemeris. The primary and secondary eclipse times are indicated by + and × symbols, respectively.

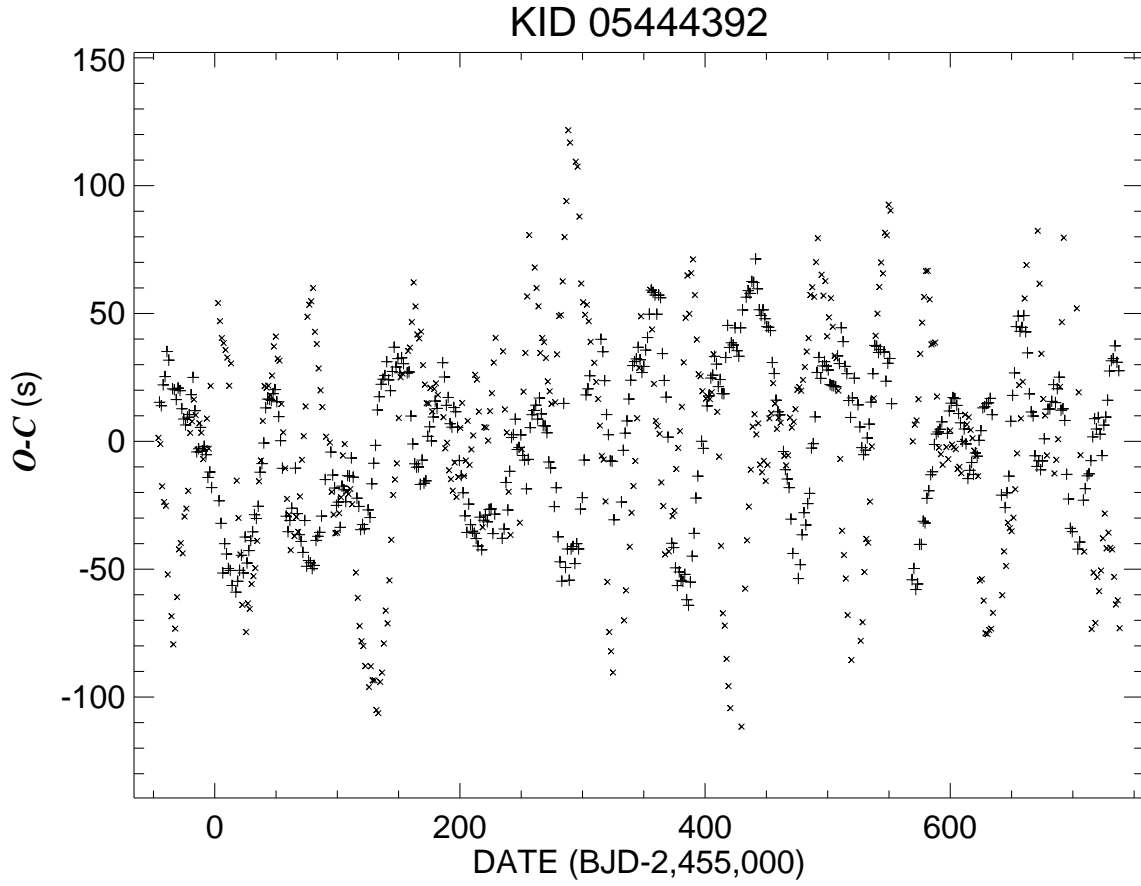


Fig. 2.13.— The observed minus calculated eclipse times relative to a linear ephemeris. The primary and secondary eclipse times are indicated by + and × symbols, respectively.

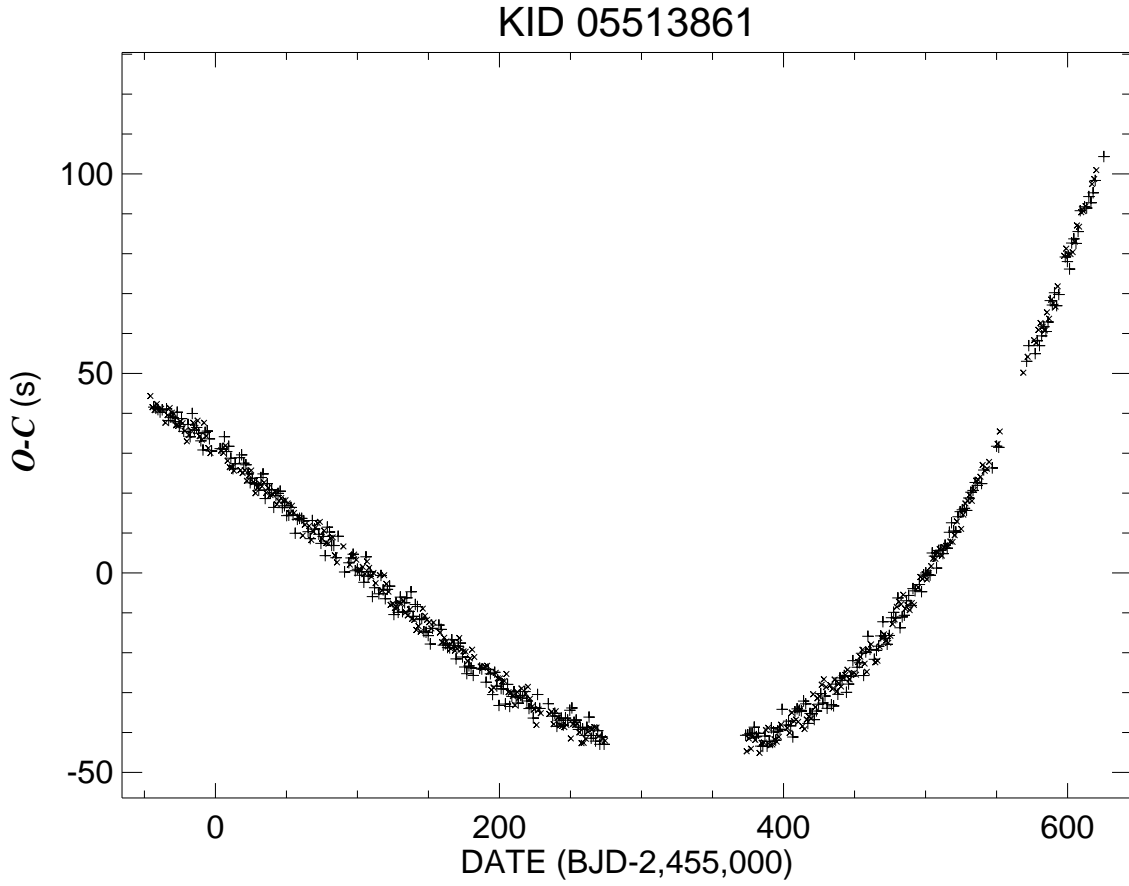


Fig. 2.14.— The observed minus calculated eclipse times relative to a linear ephemeris. The primary and secondary eclipse times are indicated by + and × symbols, respectively.

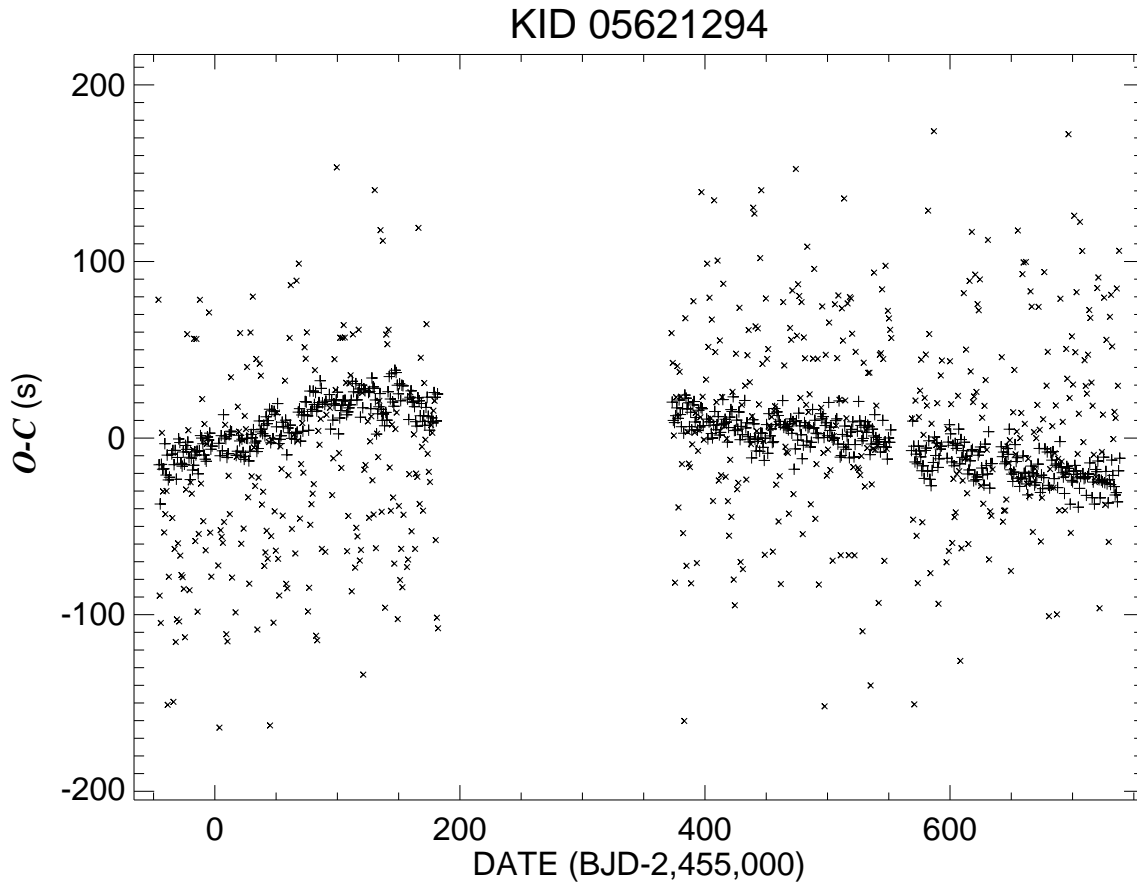


Fig. 2.15.— The observed minus calculated eclipse times relative to a linear ephemeris. The primary and secondary eclipse times are indicated by + and  $\times$  symbols, respectively.

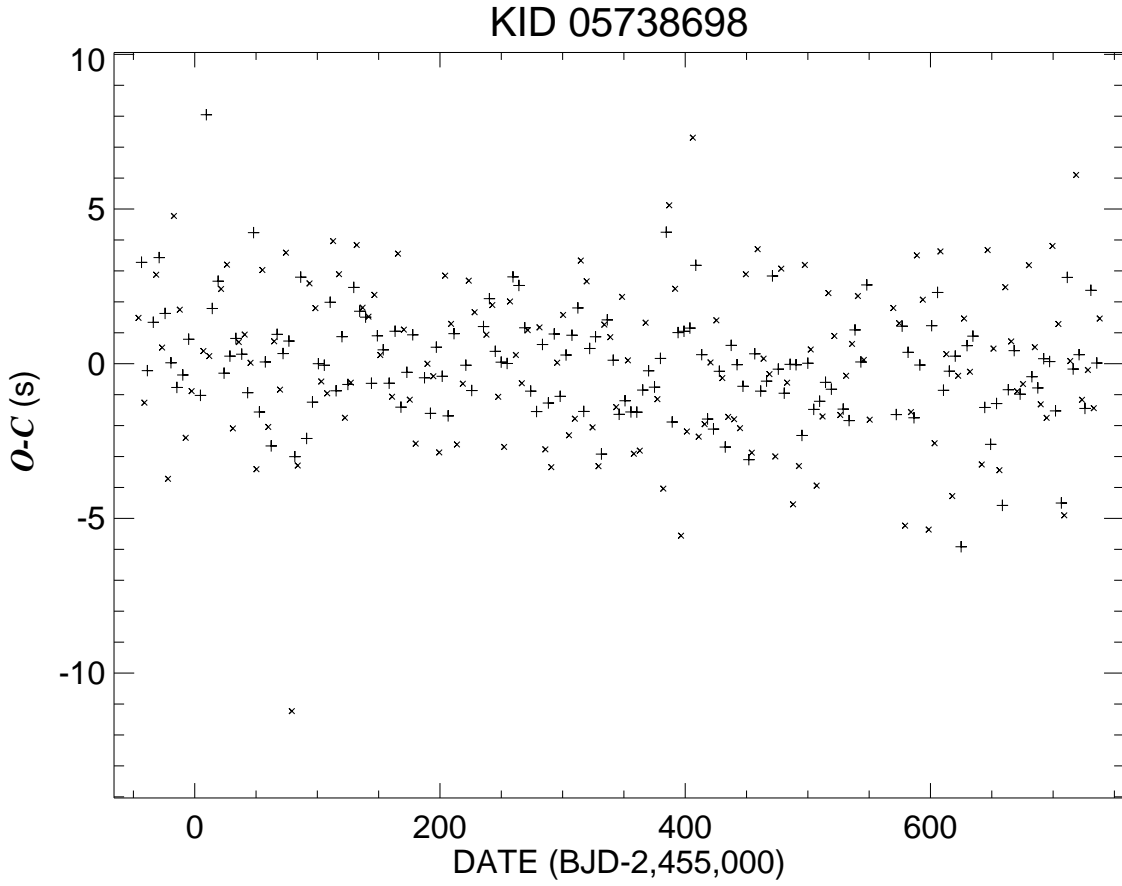


Fig. 2.16.— The observed minus calculated eclipse times relative to a linear ephemeris. The primary and secondary eclipse times are indicated by + and × symbols, respectively.

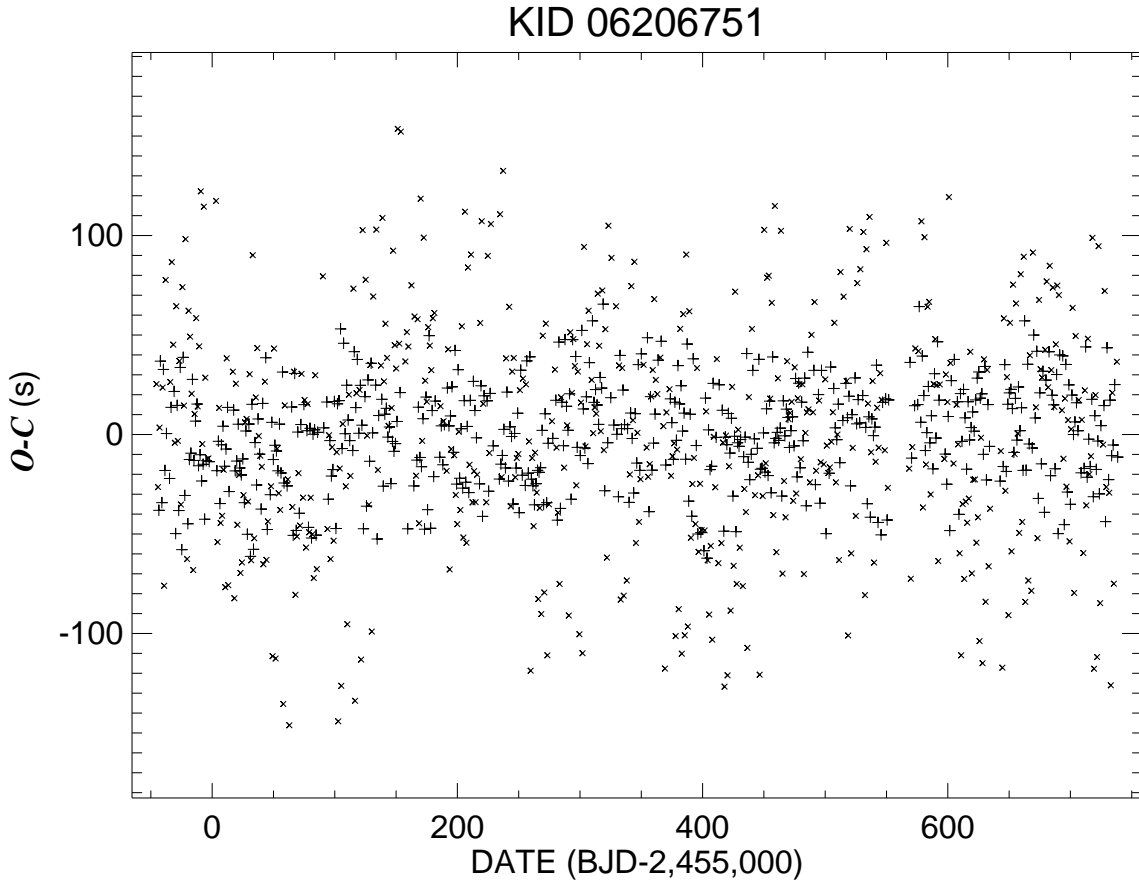


Fig. 2.17.— The observed minus calculated eclipse times relative to a linear ephemeris. The primary and secondary eclipse times are indicated by + and  $\times$  symbols, respectively.

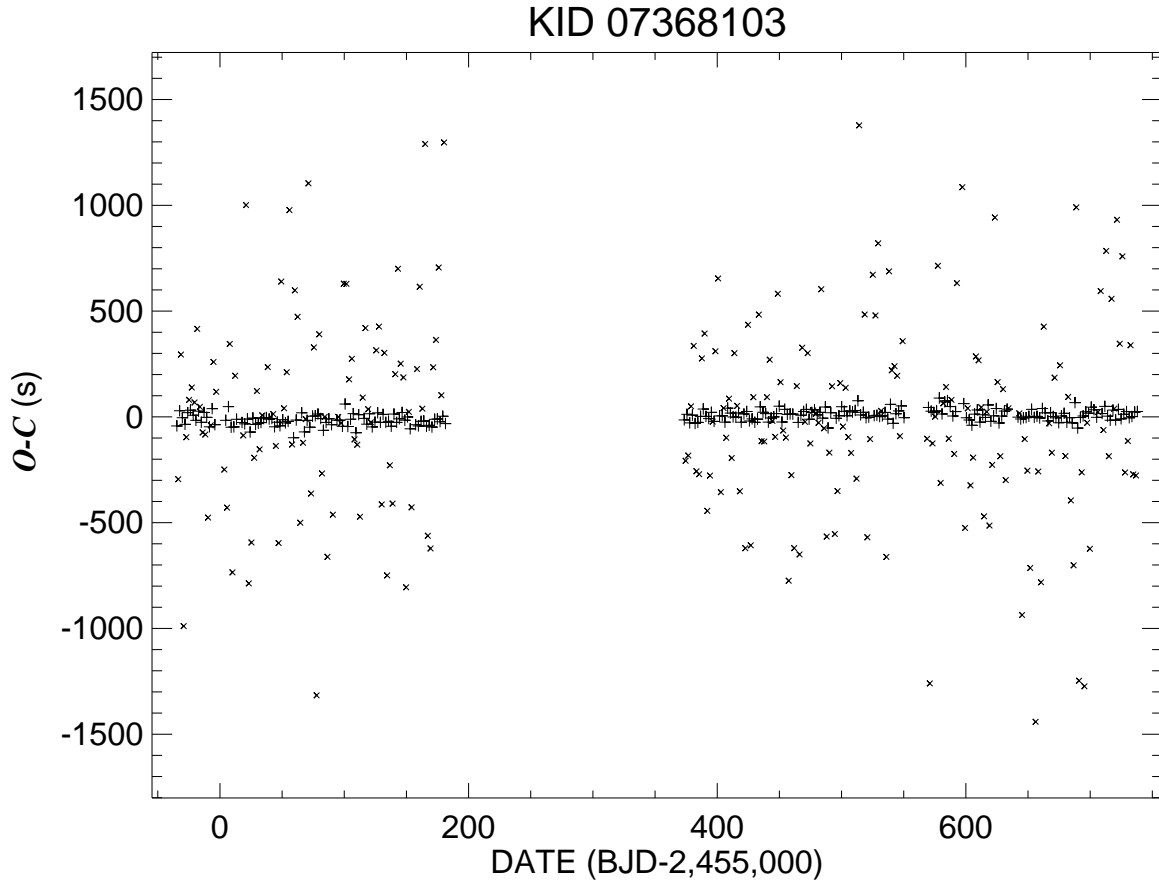


Fig. 2.18.— The observed minus calculated eclipse times relative to a linear ephemeris. The primary and secondary eclipse times are indicated by + and  $\times$  symbols, respectively.



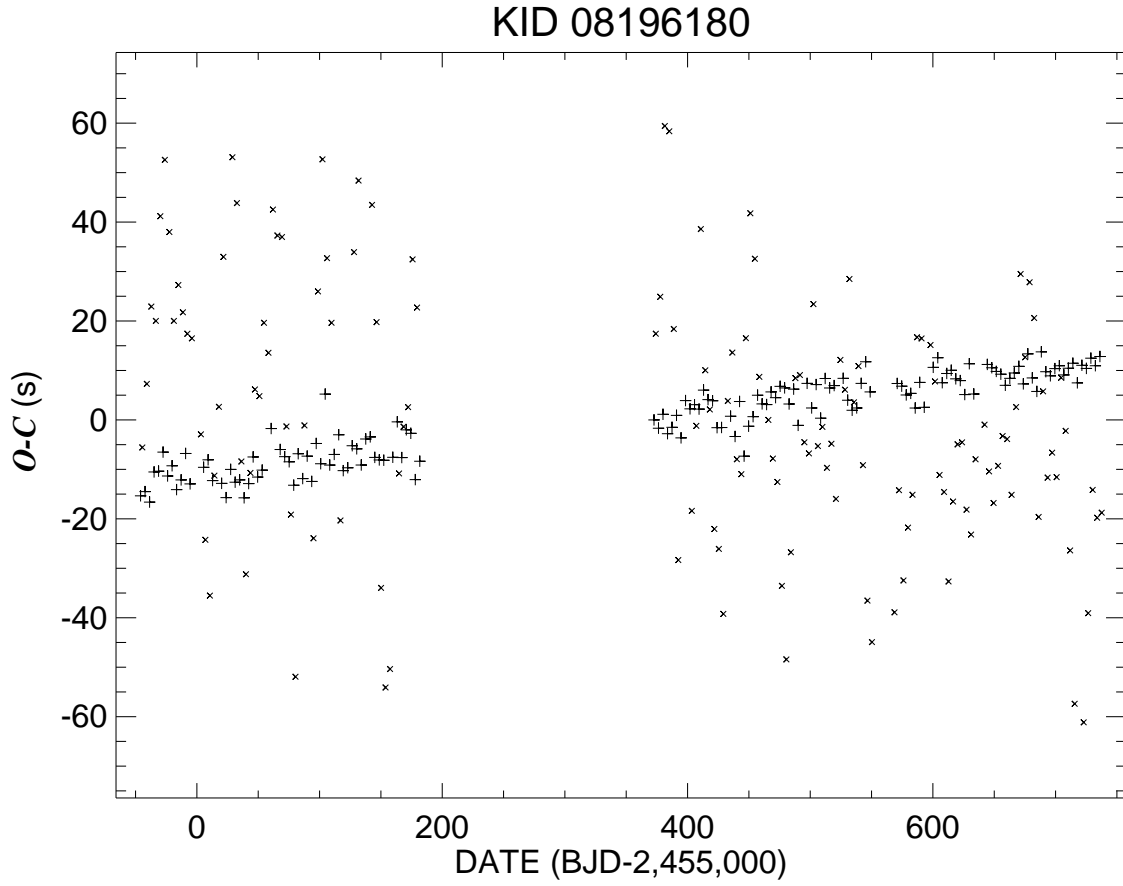


Fig. 2.19.— The observed minus calculated eclipse times relative to a linear ephemeris. The primary and secondary eclipse times are indicated by + and × symbols, respectively.

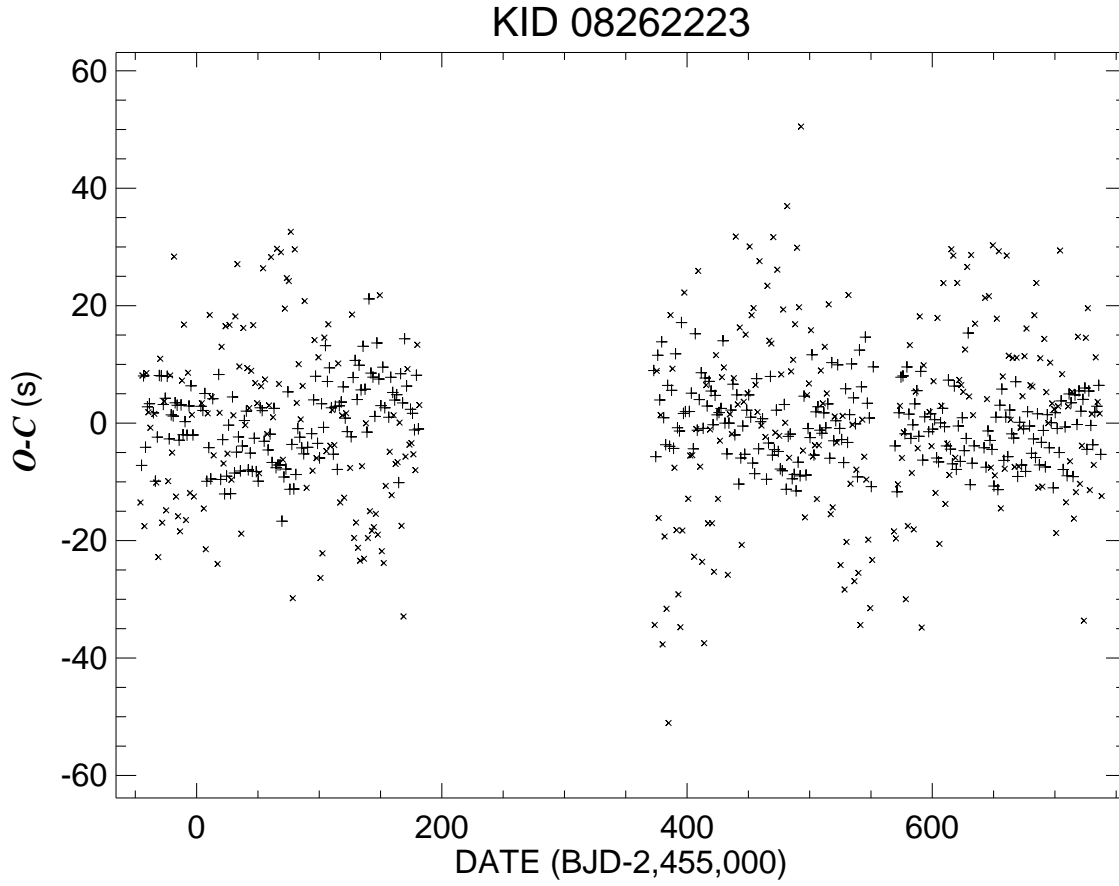


Fig. 2.20.— The observed minus calculated eclipse times relative to a linear ephemeris. The primary and secondary eclipse times are indicated by + and  $\times$  symbols, respectively.

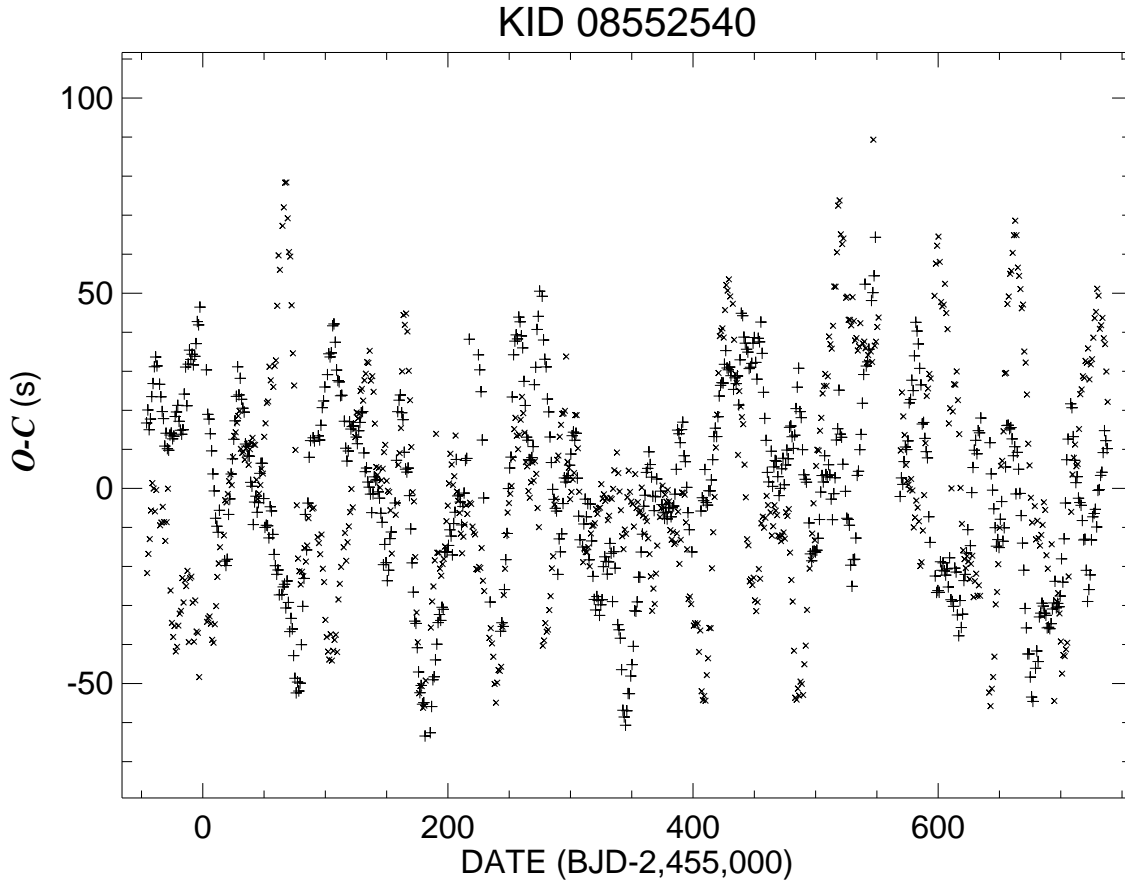


Fig. 2.21.— The observed minus calculated eclipse times relative to a linear ephemeris. The primary and secondary eclipse times are indicated by + and  $\times$  symbols, respectively.

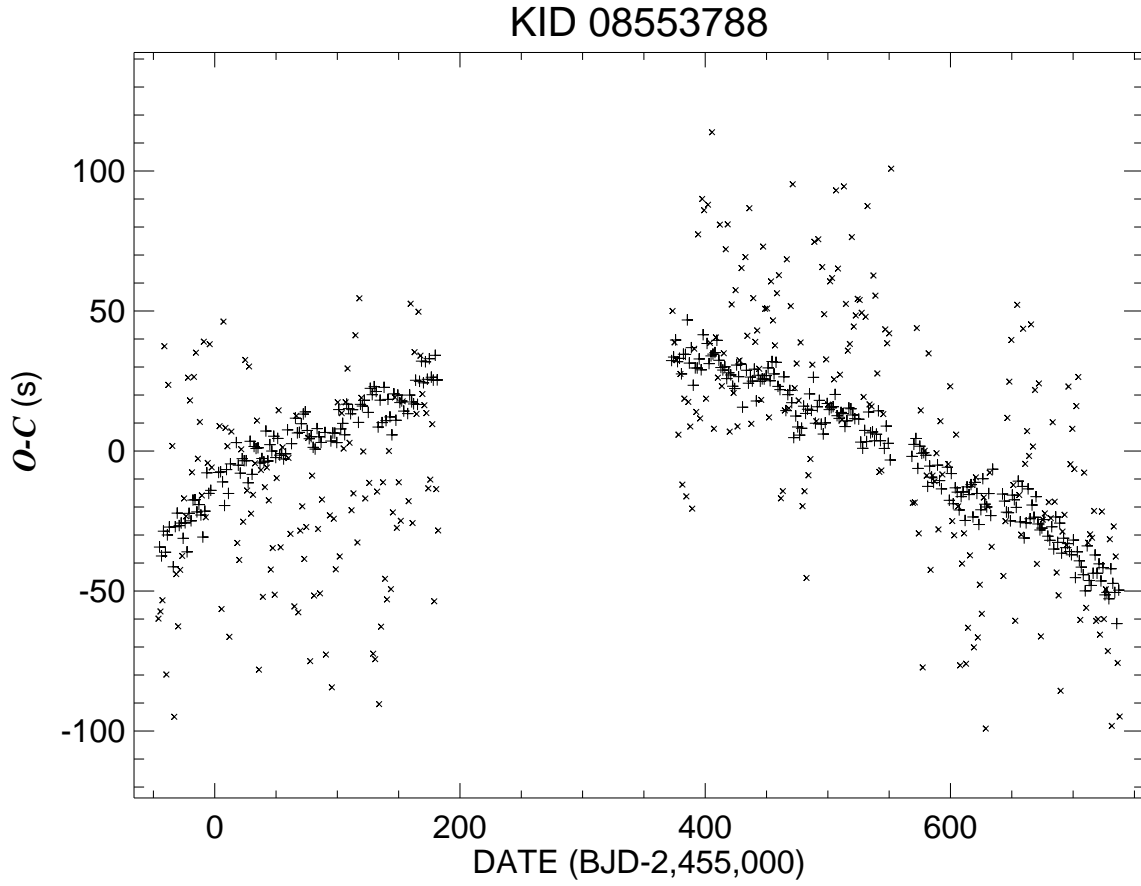


Fig. 2.22.— The observed minus calculated eclipse times relative to a linear ephemeris. The primary and secondary eclipse times are indicated by + and  $\times$  symbols, respectively.

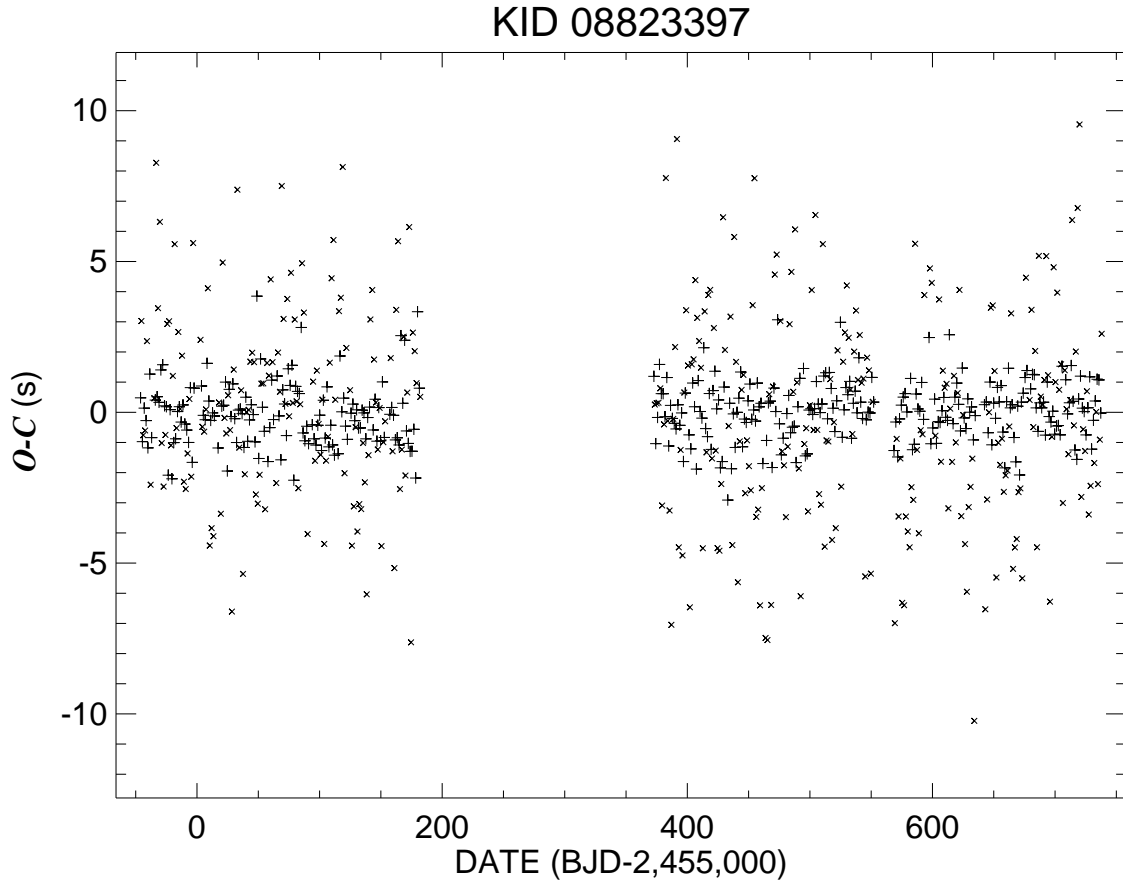


Fig. 2.23.— The observed minus calculated eclipse times relative to a linear ephemeris. The primary and secondary eclipse times are indicated by + and  $\times$  symbols, respectively.

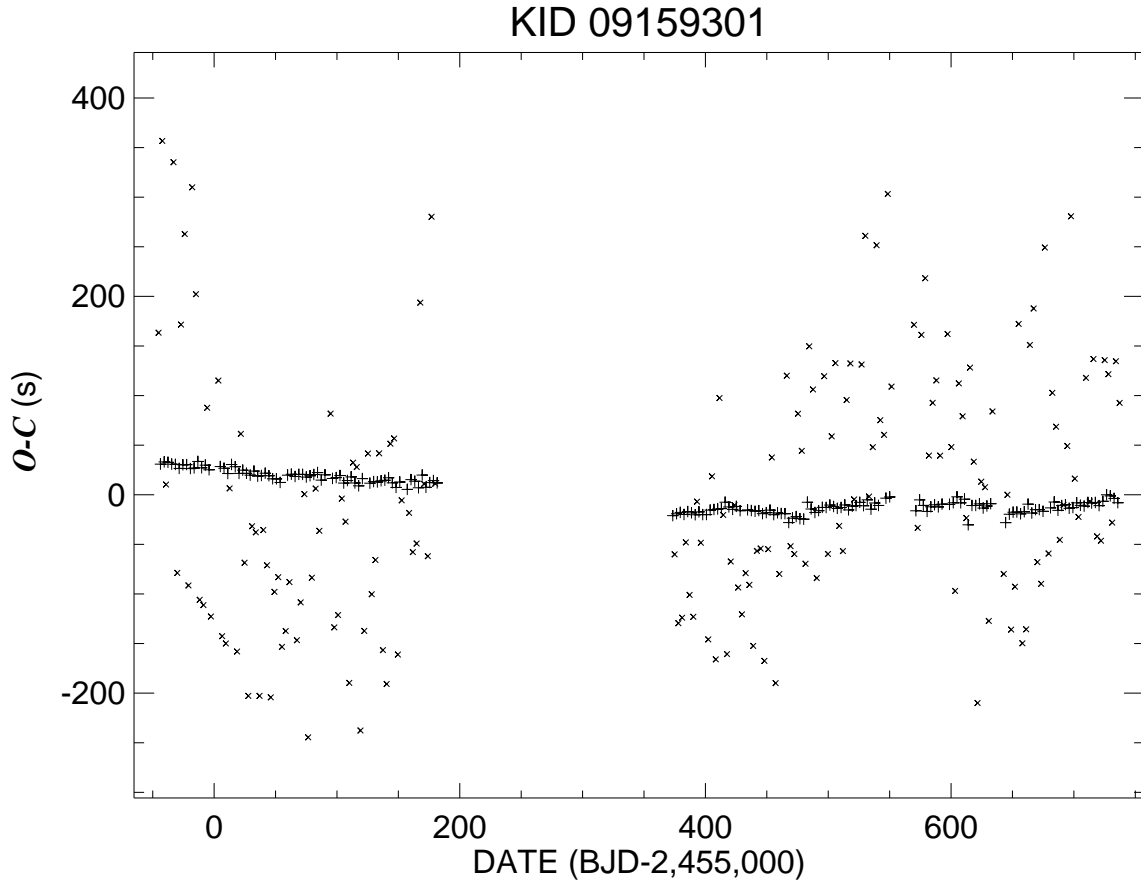


Fig. 2.24.— The observed minus calculated eclipse times relative to a linear ephemeris. The primary and secondary eclipse times are indicated by + and  $\times$  symbols, respectively.

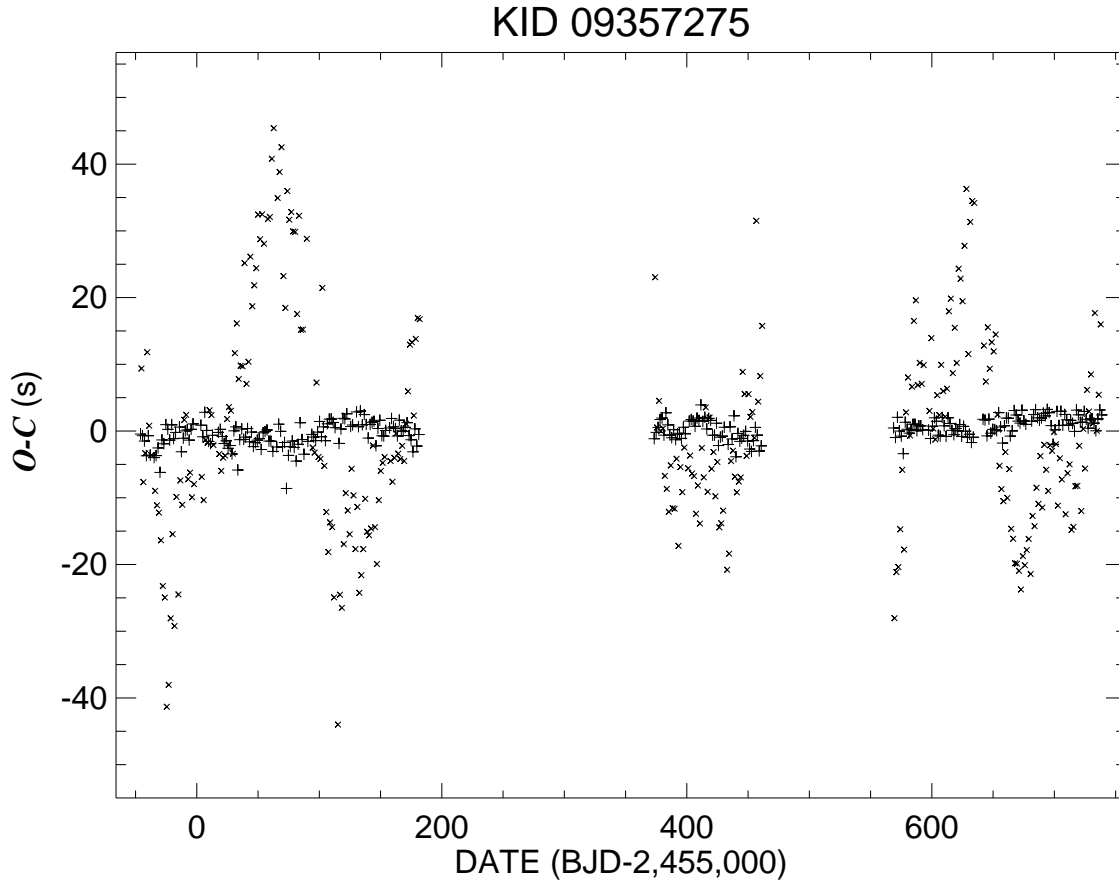


Fig. 2.25.— The observed minus calculated eclipse times relative to a linear ephemeris. The primary and secondary eclipse times are indicated by + and  $\times$  symbols, respectively.

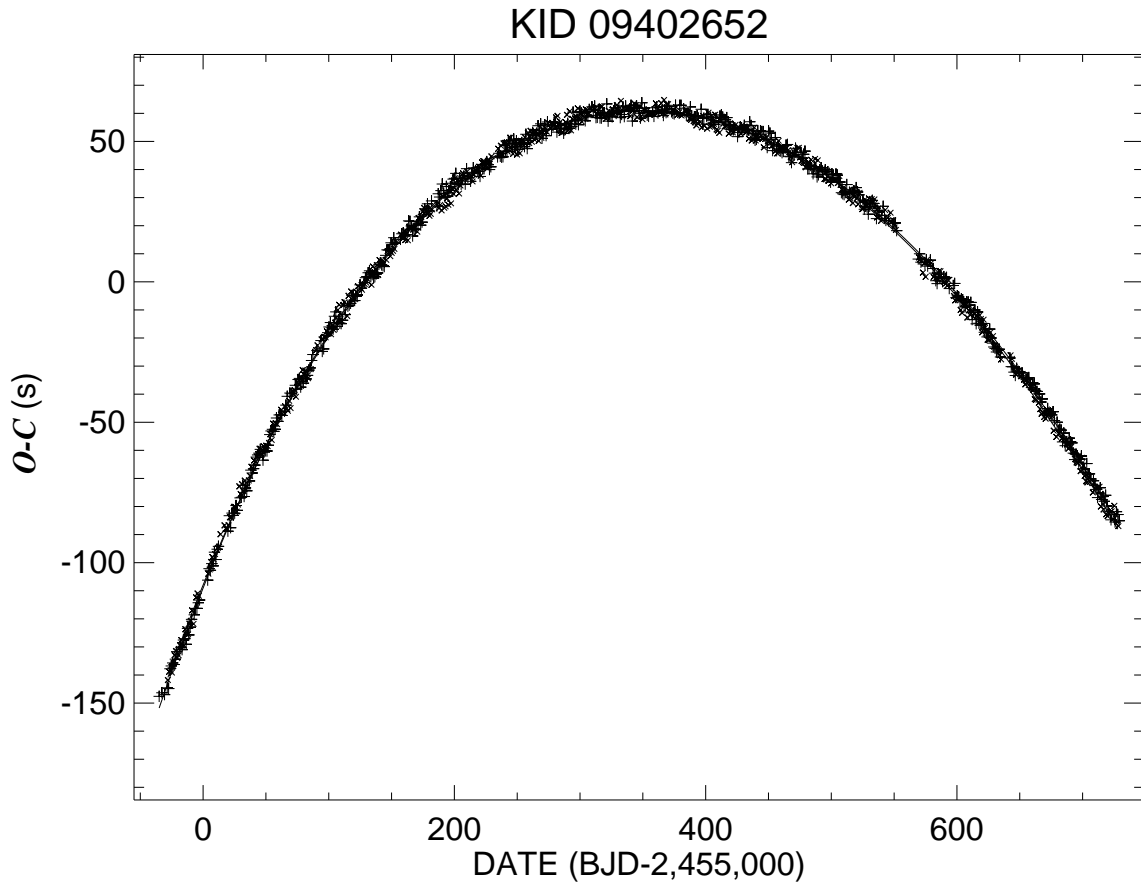


Fig. 2.26.— The observed minus calculated eclipse times relative to a linear ephemeris. The primary and secondary eclipse times are indicated by + and × symbols, respectively.



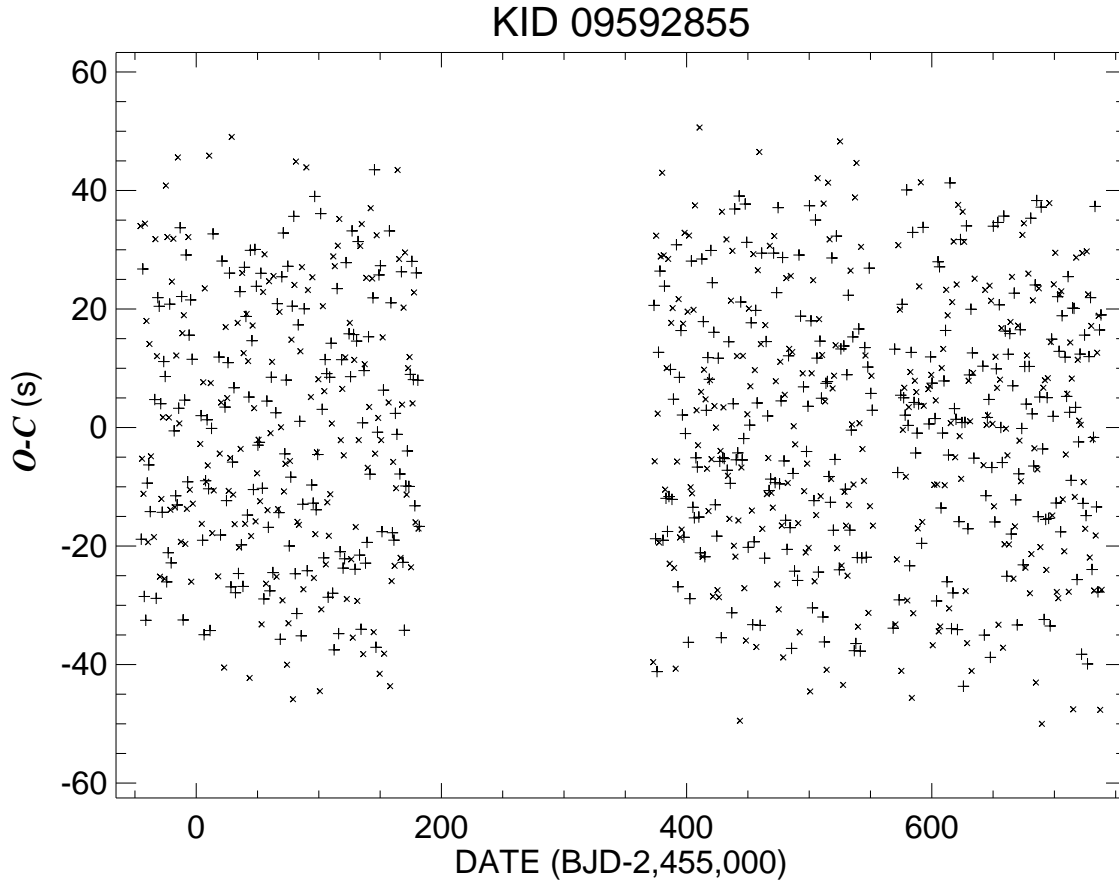


Fig. 2.27.— The observed minus calculated eclipse times relative to a linear ephemeris. The primary and secondary eclipse times are indicated by + and  $\times$  symbols, respectively.

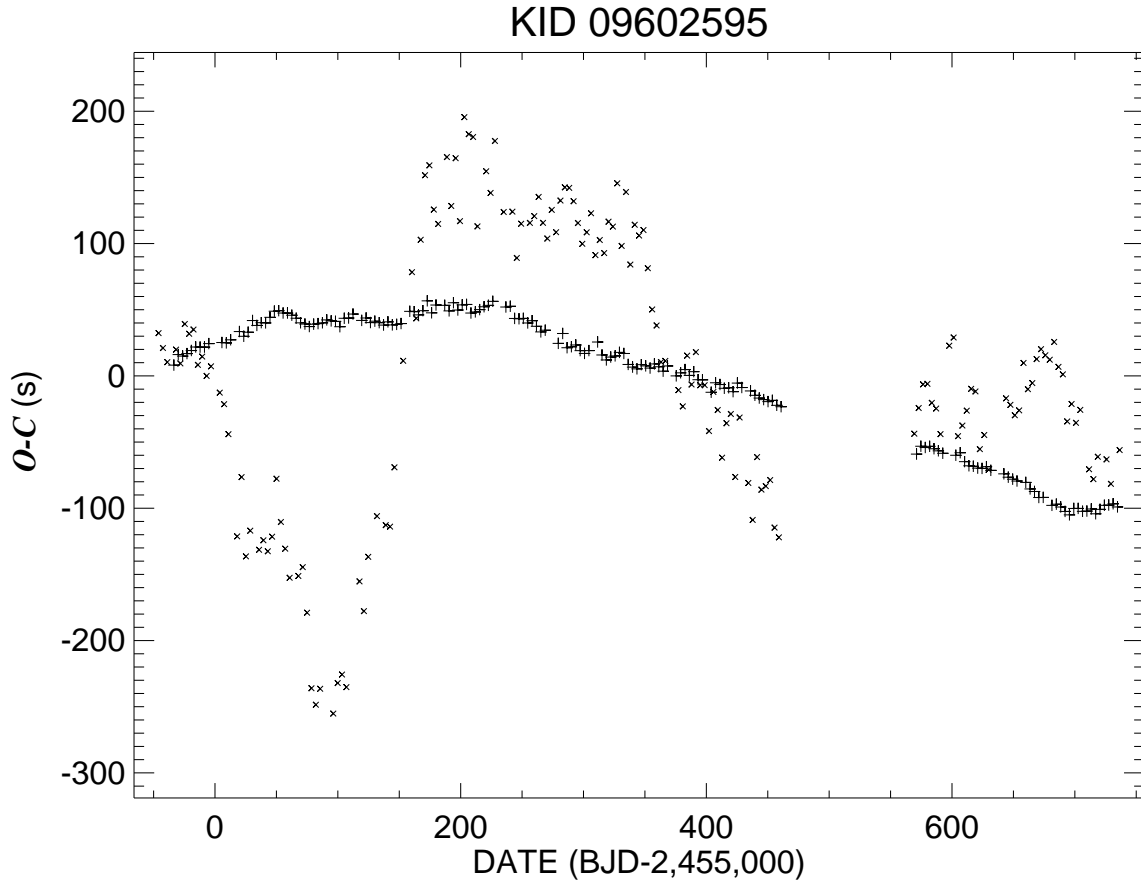


Fig. 2.28.— The observed minus calculated eclipse times relative to a linear ephemeris. The primary and secondary eclipse times are indicated by + and  $\times$  symbols, respectively.

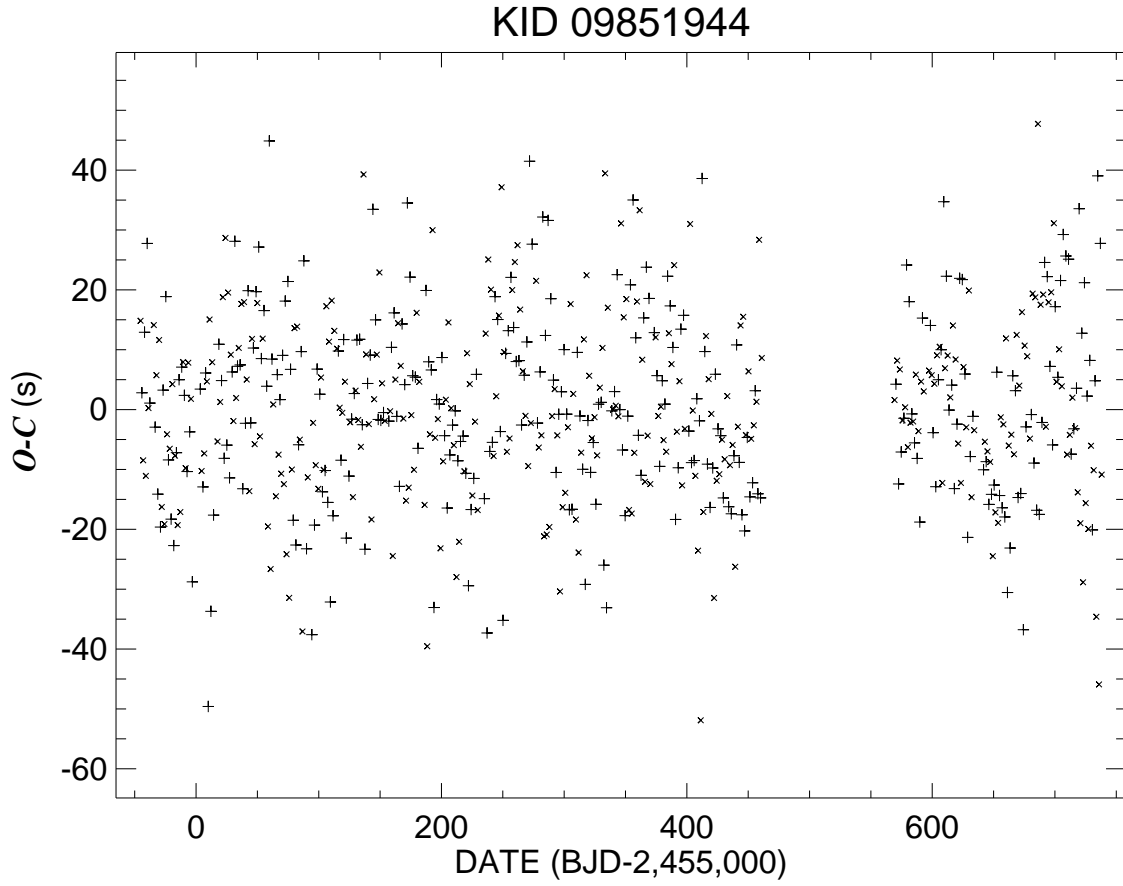


Fig. 2.29.— The observed minus calculated eclipse times relative to a linear ephemeris. The primary and secondary eclipse times are indicated by + and  $\times$  symbols, respectively.

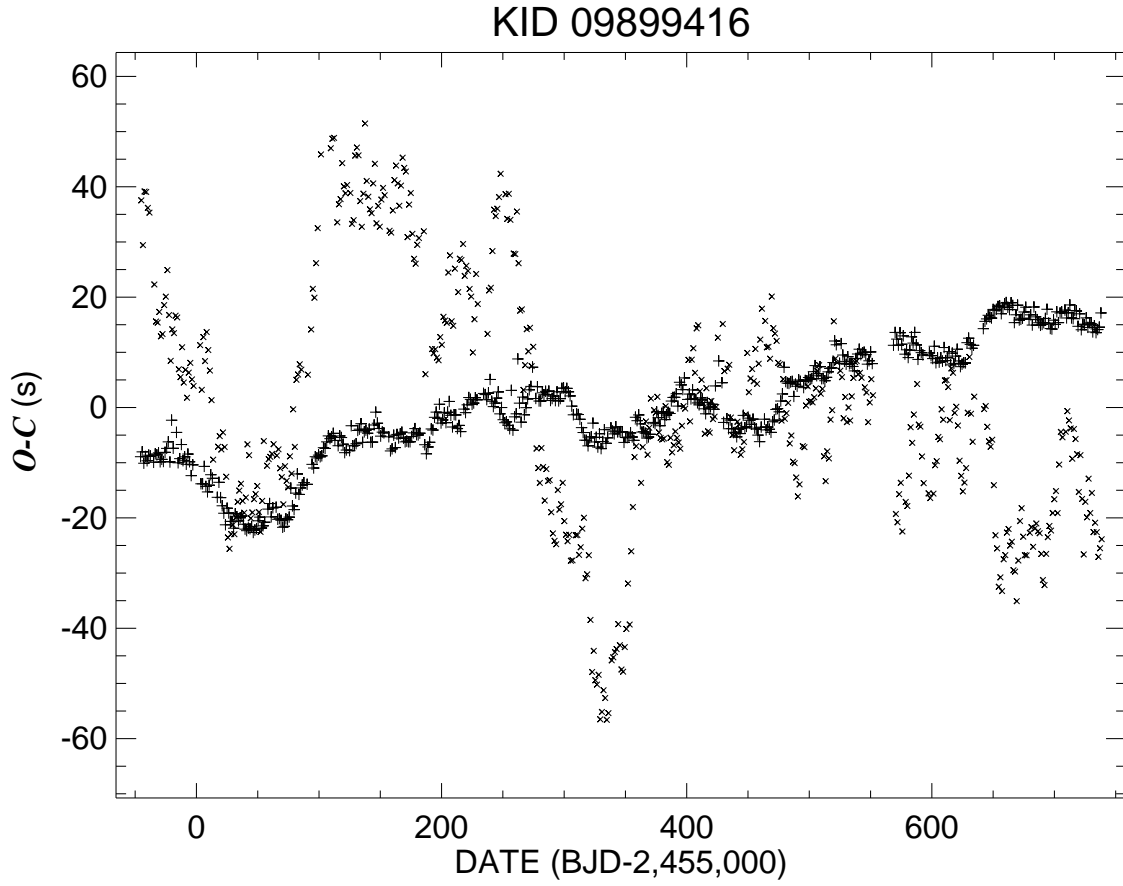


Fig. 2.30.— The observed minus calculated eclipse times relative to a linear ephemeris. The primary and secondary eclipse times are indicated by + and × symbols, respectively.

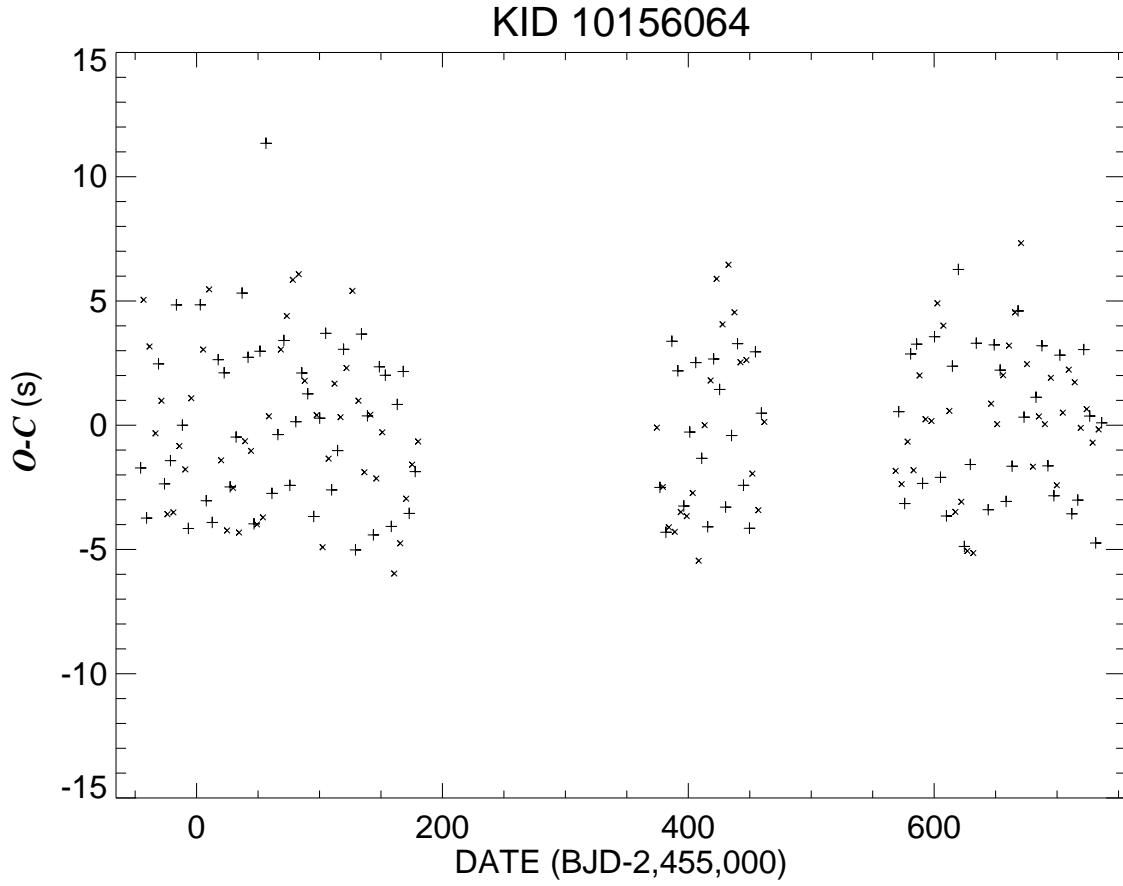


Fig. 2.31.— The observed minus calculated eclipse times relative to a linear ephemeris. The primary and secondary eclipse times are indicated by + and × symbols, respectively.

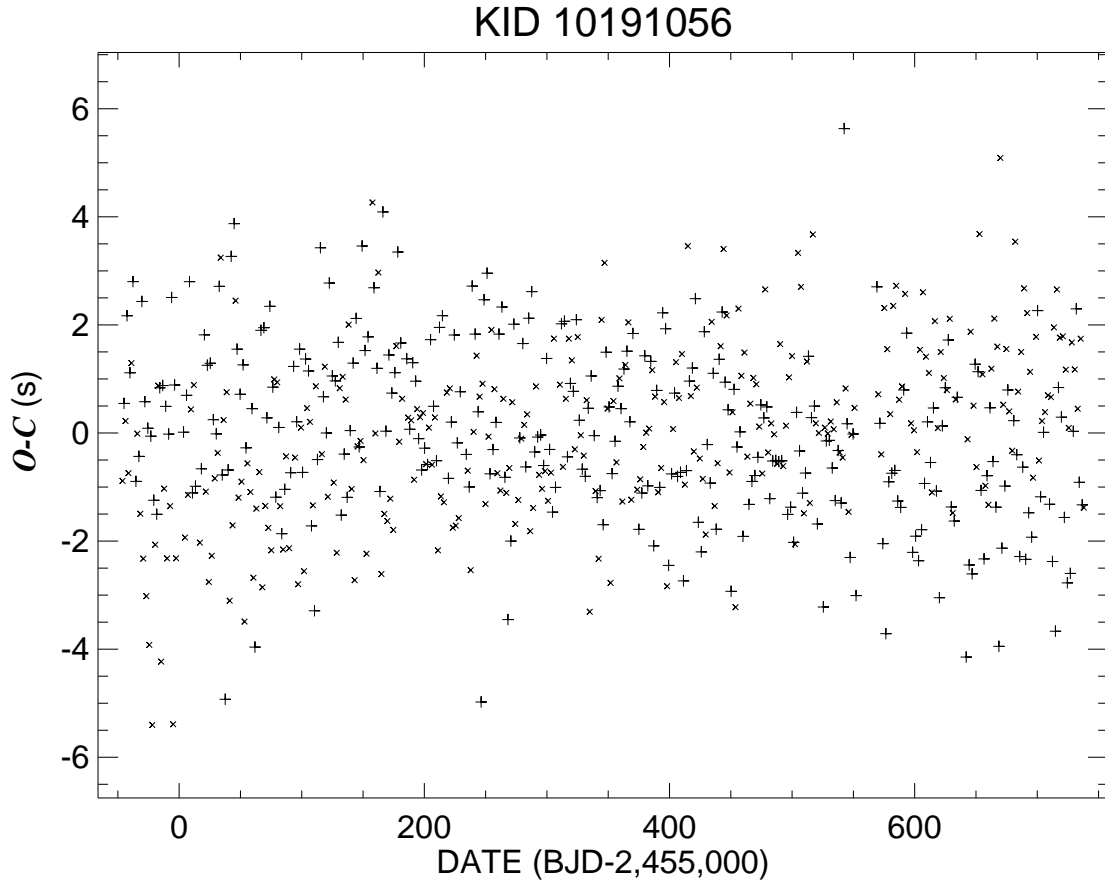


Fig. 2.32.— The observed minus calculated eclipse times relative to a linear ephemeris. The primary and secondary eclipse times are indicated by + and  $\times$  symbols, respectively.

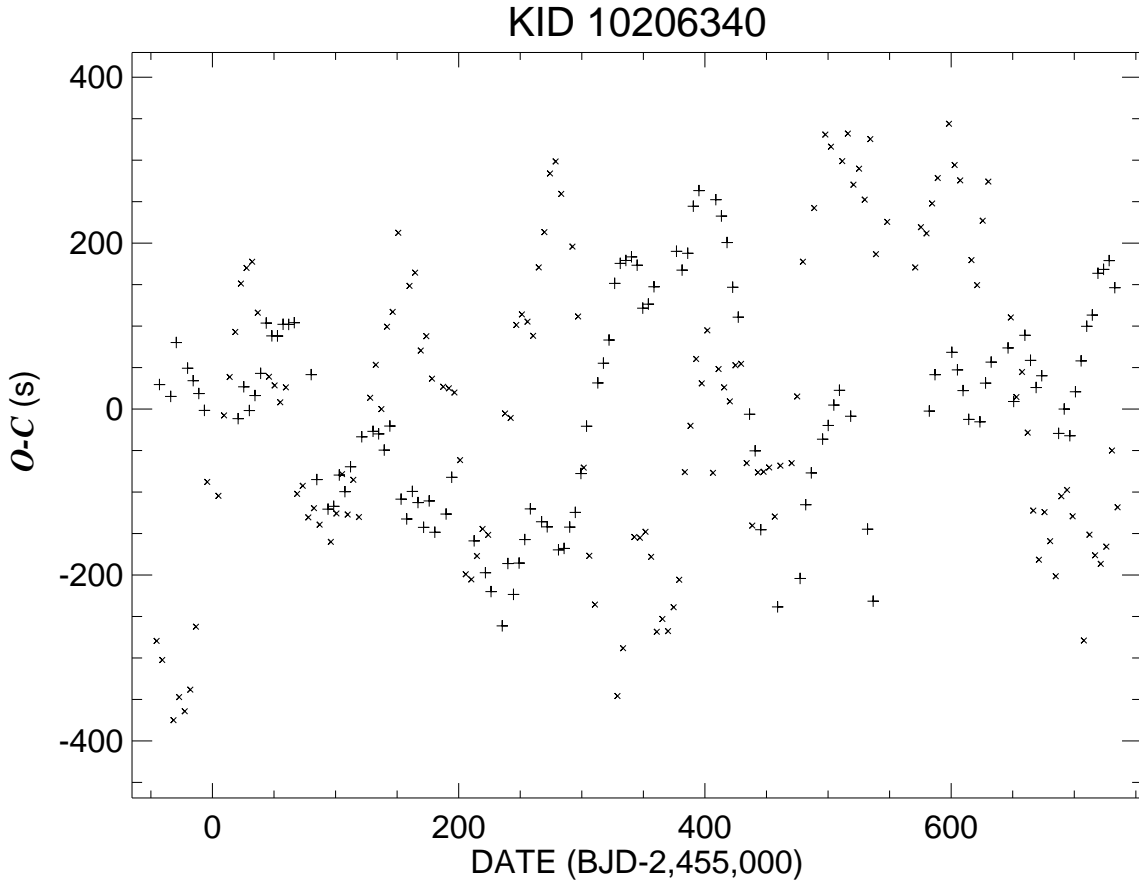


Fig. 2.33.— The observed minus calculated eclipse times relative to a linear ephemeris. The primary and secondary eclipse times are indicated by + and × symbols, respectively.

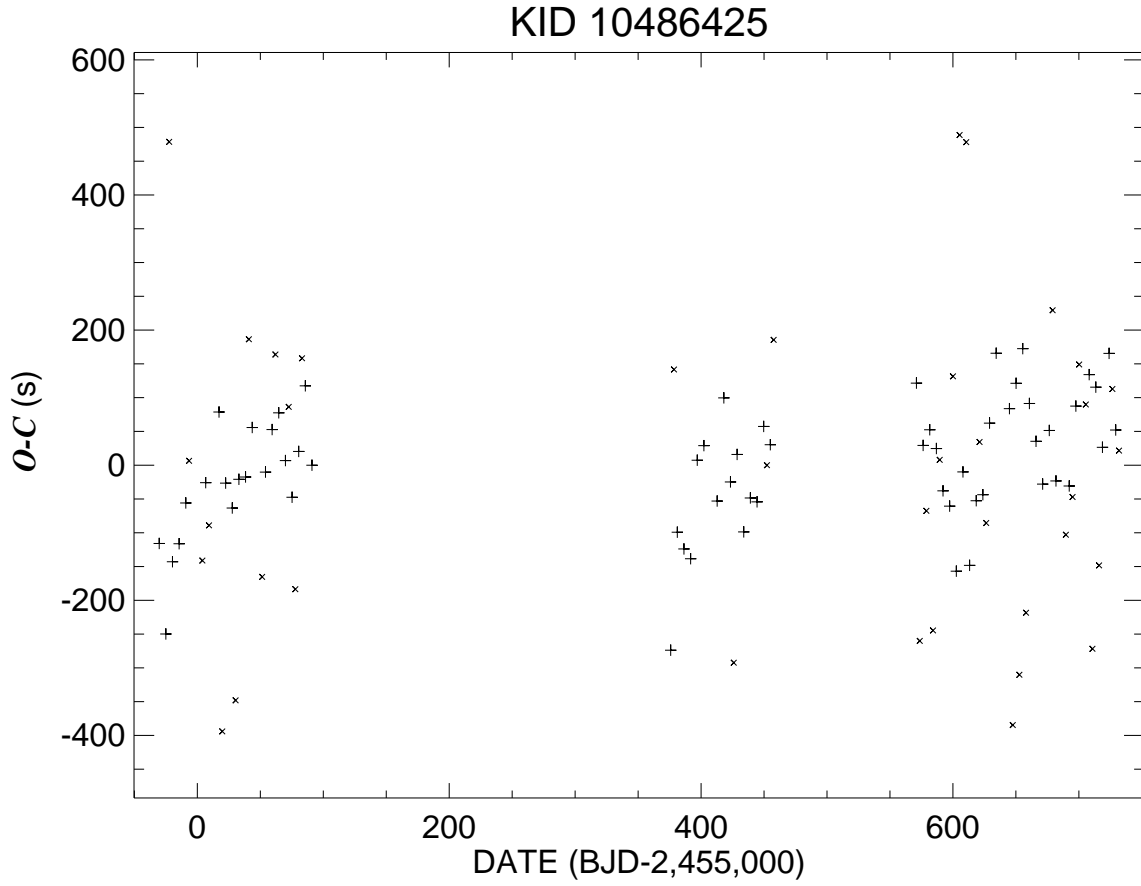


Fig. 2.34.— The observed minus calculated eclipse times relative to a linear ephemeris. The primary and secondary eclipse times are indicated by + and × symbols, respectively.



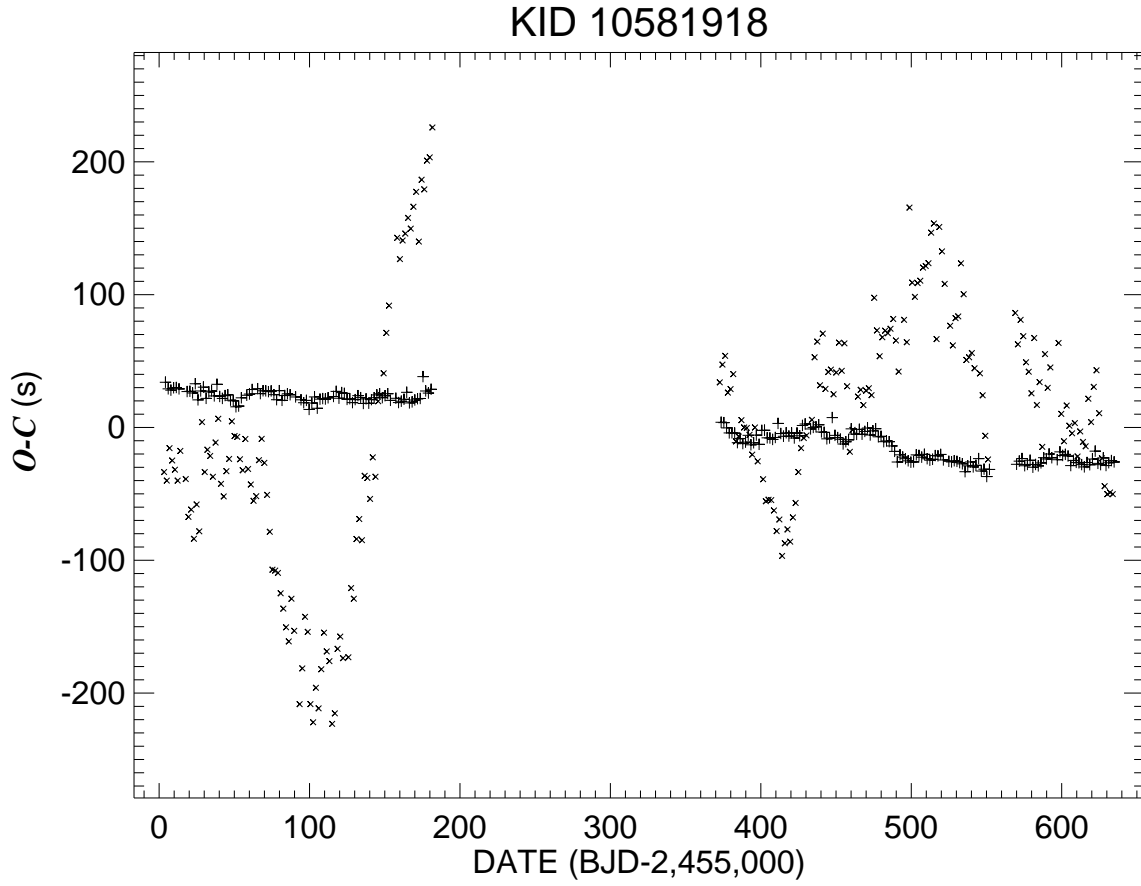


Fig. 2.35.— The observed minus calculated eclipse times relative to a linear ephemeris. The primary and secondary eclipse times are indicated by + and  $\times$  symbols, respectively.

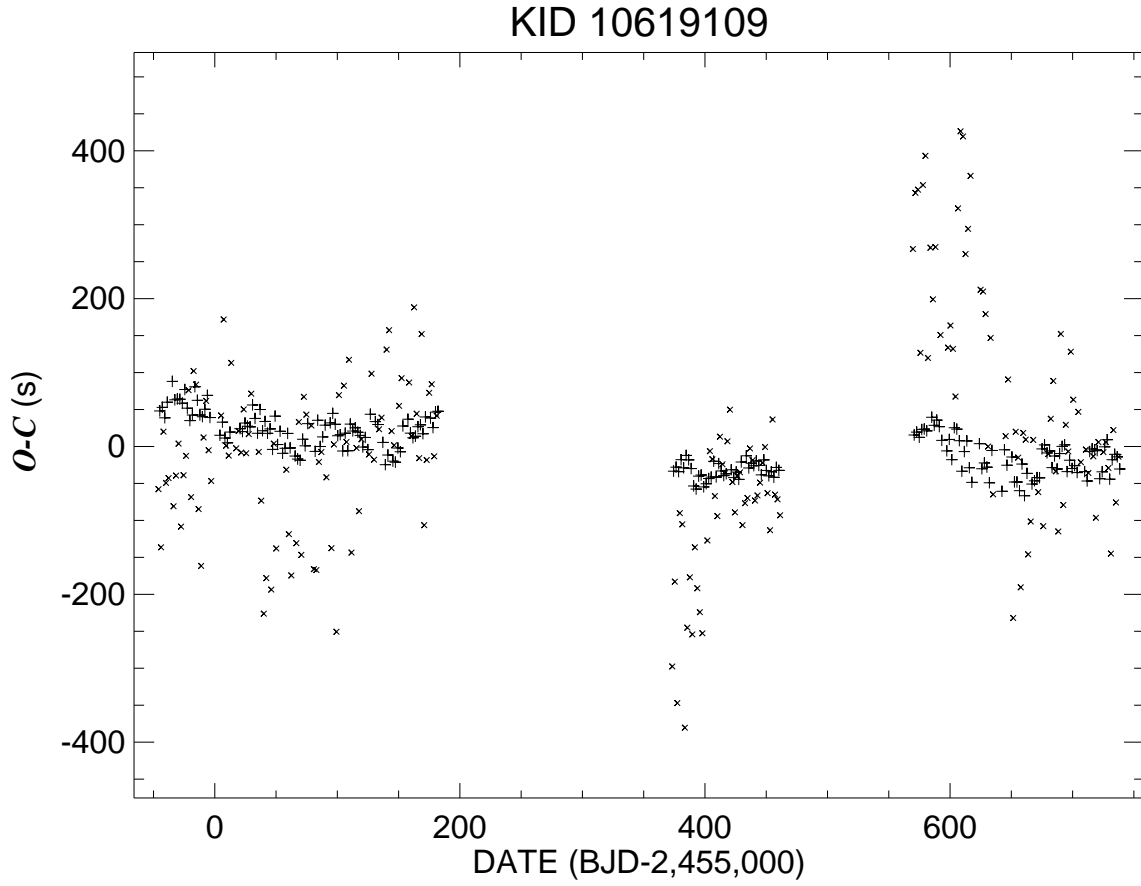


Fig. 2.36.— The observed minus calculated eclipse times relative to a linear ephemeris. The primary and secondary eclipse times are indicated by + and  $\times$  symbols, respectively.

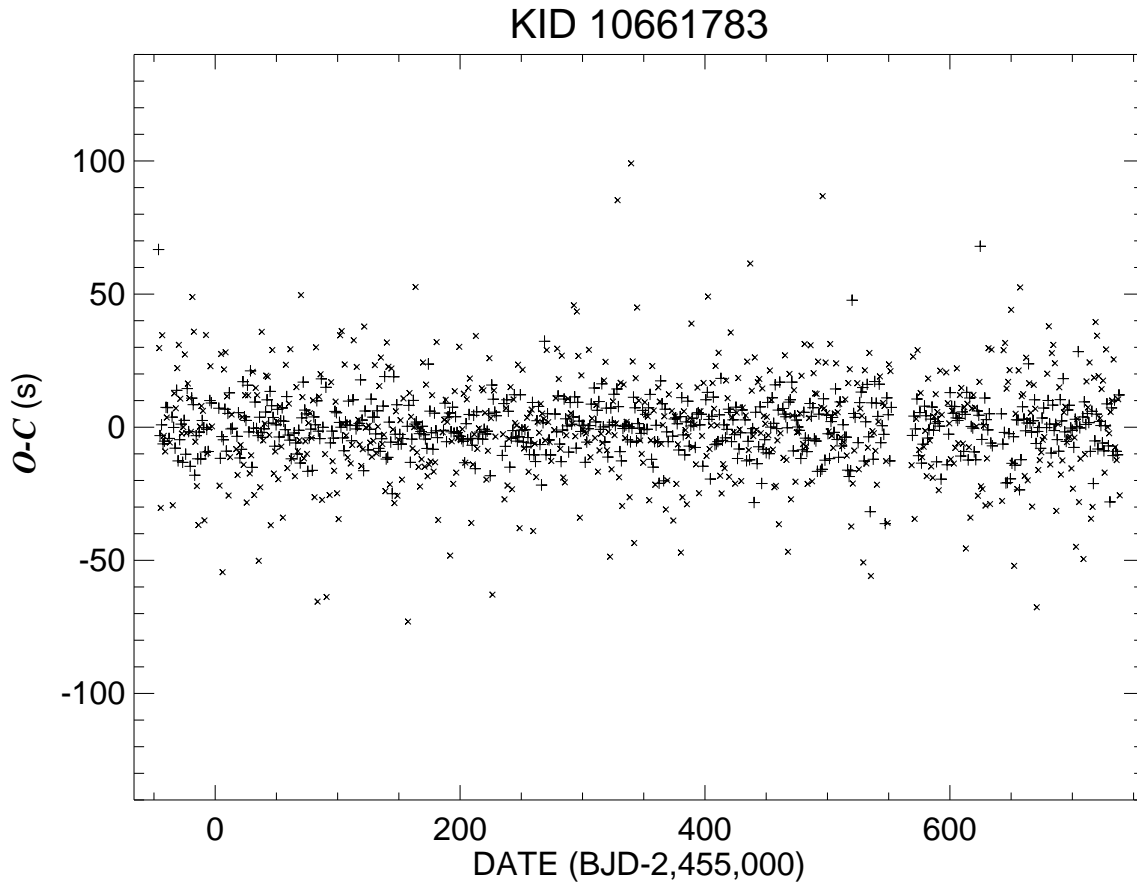


Fig. 2.37.— The observed minus calculated eclipse times relative to a linear ephemeris. The primary and secondary eclipse times are indicated by + and  $\times$  symbols, respectively.

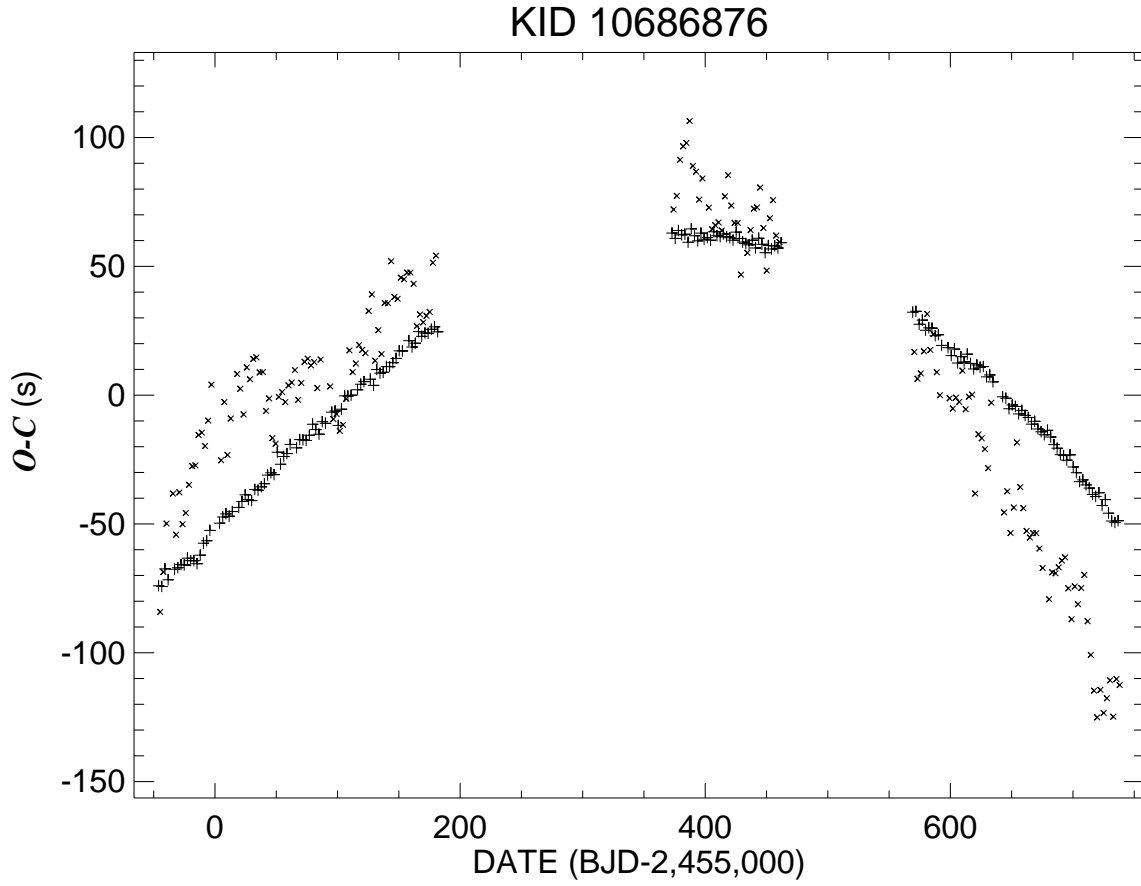


Fig. 2.38.— The observed minus calculated eclipse times relative to a linear ephemeris. The primary and secondary eclipse times are indicated by + and × symbols, respectively.

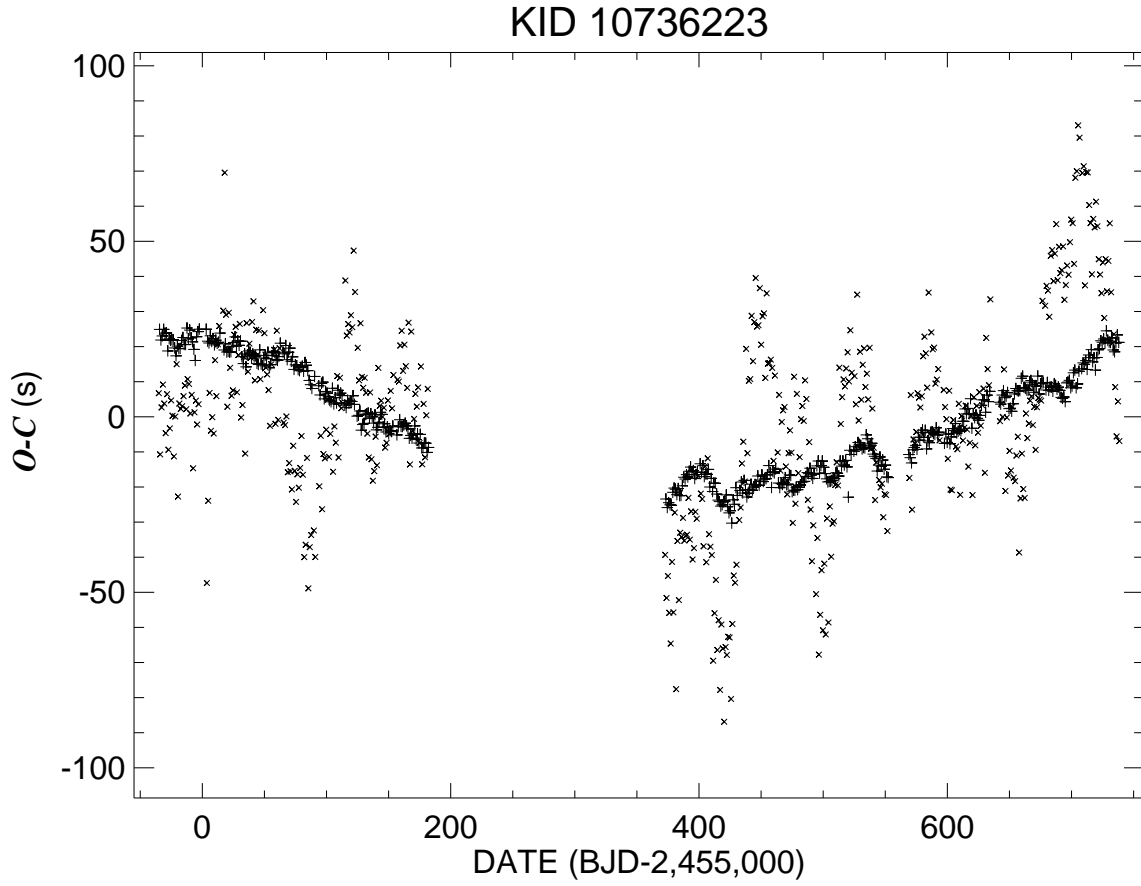


Fig. 2.39.— The observed minus calculated eclipse times relative to a linear ephemeris. The primary and secondary eclipse times are indicated by + and × symbols, respectively.

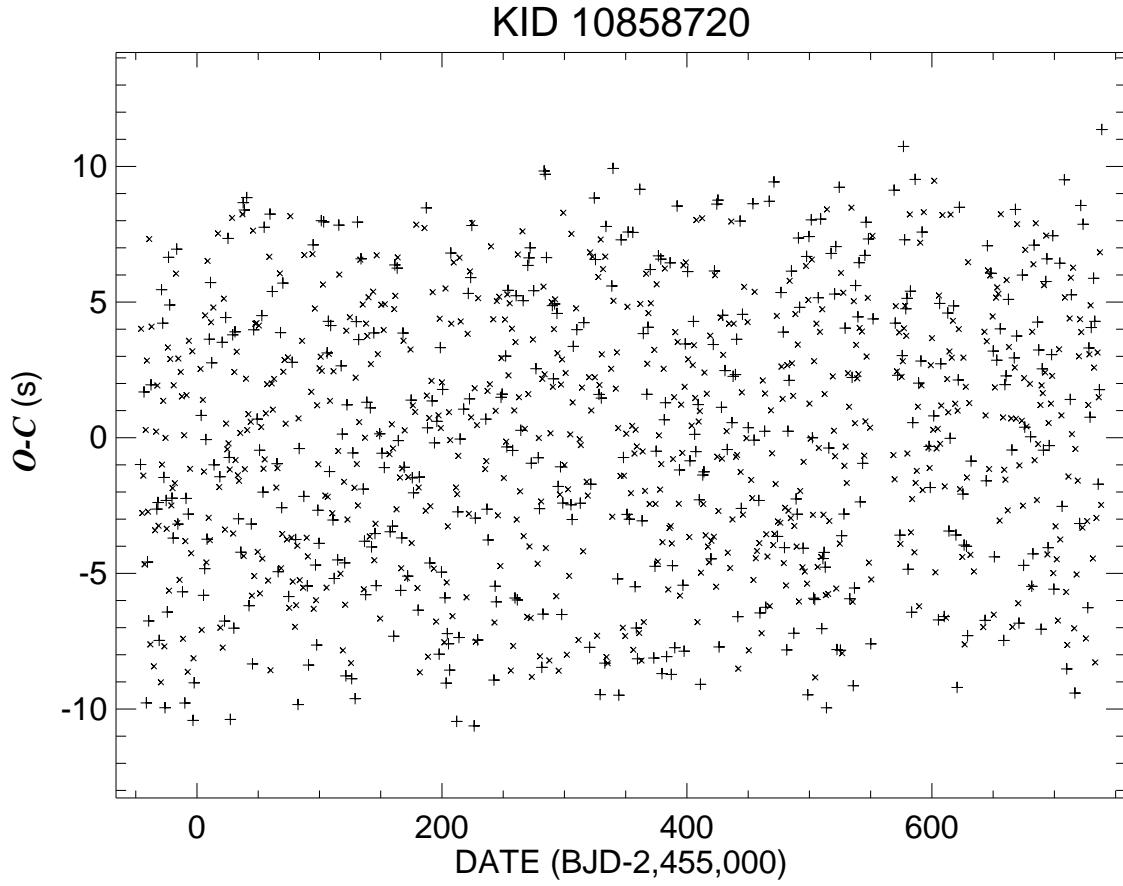


Fig. 2.40.— The observed minus calculated eclipse times relative to a linear ephemeris. The primary and secondary eclipse times are indicated by + and × symbols, respectively.

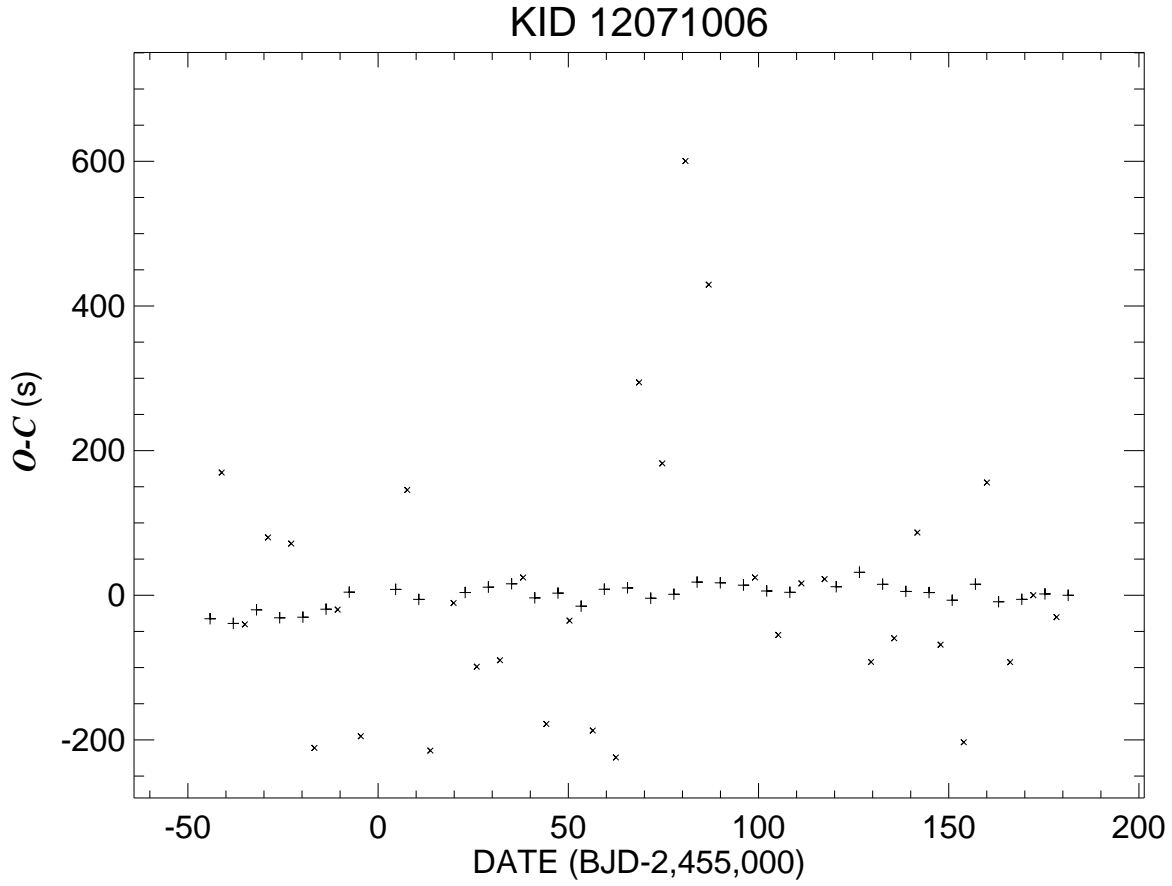


Fig. 2.41.— The observed minus calculated eclipse times relative to a linear ephemeris. The primary and secondary eclipse times are indicated by + and  $\times$  symbols, respectively.

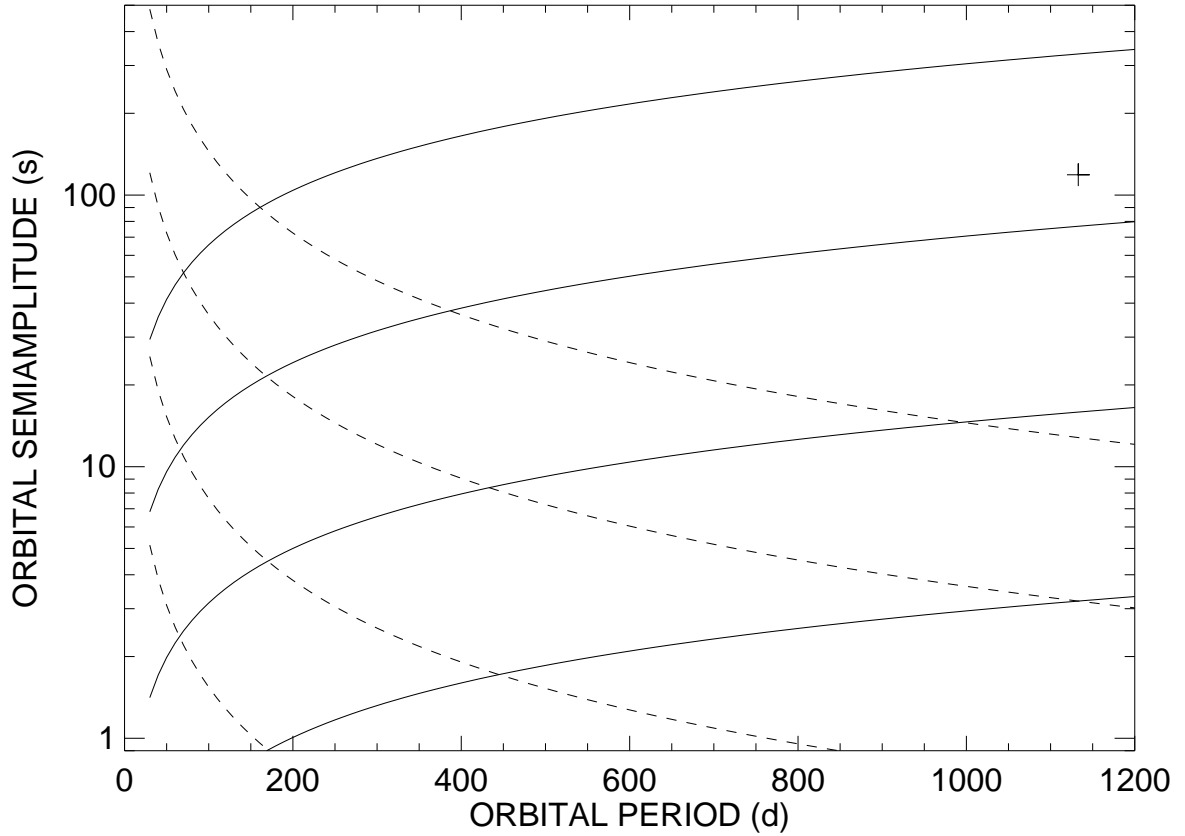


Fig. 3.— The predicted semi-amplitudes for the light travel time effect (*solid lines*) and the dynamical effect (*dashed lines*) for a third body mass of 0.008, 0.04, 0.2, and  $1M_{\odot}$ , from bottom to top, respectively. The plus sign marks the preliminary period and LITE semi-amplitude for KID 9402652.